

Dissertation
Universität Bremen
Fachbereich für Physik Elektrotechnik
Institut für Umweltphysik

Remote sensing of tropospheric methane and isotopes of atmospheric carbon dioxide using Fourier Transform Spectrometry

Zur Erlangung des akademischen Titels
Doktor der Naturwissenschaften (Dr. rer. nat.)

Dipl.-Phys. Zhiting Wang

Gutachter: Prof. Dr. Justus Notholt

Abstract

Due to the warming effect of atmospheric trace gases, such as CH₄ and CO₂, it is important to monitor their variations and understand their sources and sinks. While an increasing trend in atmospheric concentrations of CH₄ and CO₂ is confirmed by many measurements, the sources and sinks are not completely understood. As one of the methods determining sinks and sources of traces gases, inverse modeling, its accuracy depends on assimilated observation and the simulation ability of atmospheric motion. For CH₄ measurements, a method has been developed to determine tropospheric column-averaged mole fractions of CH₄ from total columns of CH₄ and N₂O measured by solar absorption Fourier transform spectrometer (FTS). The motivation of this work is that tropospheric CH₄ is more directly related to its sources and sinks compared to the total columns, which contain variabilities of stratospheric CH₄ mostly originating from dynamic processes. Another reason is that the chemical transport model, in its current state, represents the troposphere better than the stratosphere.

The method is applied to most of the FTS sites within the Total Carbon Column Observing Network. The measured tropospheric and stratospheric column-average CH₄ are used to assess performances of three European CH₄ models in the troposphere and stratosphere separately. In addition, the isentropic mixing processes and evolutions of the polar vortex in the models are evaluated using equivalent length. It is found the southern surf zone is not developed to a real extent. Together with the southern surf zone, a region with both vertically and horizontally uniform CH₄ occur between 450 and 850 K (~18 and 30 km) in surf zone latitudes, which is absent in the models. The modeled polar vortex breaks too fast compared to the measurements.

Measuring different isotopes of one species is another approach to improve knowledge on the sources and sinks of traces gases. This is explored for CO₂ using ground-based solar FTS spectra, specifically the ratio ¹³C/¹²C in atmospheric CO₂. Retrieval from the FTS spectra is almost entirely determined by assumed molecular spectroscopy. The existing databases can not fulfill requirements for CO₂ isotopes retrieval. An algorithm that inverts molecular spectroscopy from the ground-based spectra is developed. This algorithm is applied to H₂O, CO₂ and solar lines indicating its feasibility. While the inverted spectroscopy improves the accuracy of the column and profile retrieval of CO₂ and H₂O, the retrieved ratio ¹³C/¹²C is still beyond the required accuracy at a FTS site Bialystok.

Contents

Abstract.....	II
Contents.....	III
1. Introduction.....	1
1.1 Sources and sinks of atmospheric CH4.....	1
1.2 Atmospheric properties and CH4 transport.....	4
1.3 Ground-based observation of greenhouse gases by TCCON.....	9
2. Methods.....	10
2.1. Fourier transform spectrometry.....	10
2.2. Retrieval theory and methods.....	12
3. Retrieval of tropospheric CH4 from solar absorption FTS spectra.....	16
3.1. A posteriori correction method.....	16
3.1.1. FTS measurements.....	17
3.1.2. In situ measurements.....	17
3.1.3. Theory description.....	18
3.1.4. Comparison of between the N ₂ O and HF methods and in situ data.....	23
.....	26
3.1.5. Comparison with aircraft profile measurements.....	27
3.1.6. Uncertainty analysis.....	28
3.2. Profile retrieval method.....	30
3.2.1. FTS measurements and surface in situ datasets.....	30
3.2.2. Profile retrieval setup.....	31
3.2.3. Comparison with a posterior correction method and in situ data.....	33
3.3. Summary.....	34
4. Validation of European CH4 models using ground-based and satellite measurements.....	35
4.1. Description of measurements.....	35
4.2. Description of models.....	37
4.3. Comparison between FTS and surface measurements.....	39
.....	41
4.4. Comparison between measurements and models.....	42
4.4.1. FTS, GOSAT and HIPPO.....	42
4.4.2. Stratospheric satellite.....	51
4.4.3. Diagnose by Equivalent length.....	53
4.4.4. Validation of simulated CH4 vertical profiles.....	58
4.5. Summary.....	61
5. Retrieval of the isotopic composition of atmospheric CO ₂ from ground-based FTS solar absorption measurements.....	62
5.1. Problems of retrieving atmospheric CO ₂ isotopes from ground-based FTS spectra.....	62
5.2. Spectroscopy aspect.....	63
5.2.1. Inversion of spectroscopy parameter from ground-based FTS spectra.....	66
5.2.2. H ₂ O.....	68
5.2.3. Solar line.....	72
5.2.4. CO ₂	74
5.3. Retrieval aspect.....	81
5.3.1. Influence of Interference species.....	81
5.3.2. Influence of retrieval method.....	83
5.3.3. Influence of atmospheric T, P profiles.....	86
5.4. Instrumental aspect.....	87
5.4.1. Laser sampling error.....	87

5.4.2. Instrumental line shape.....	89
5.5. Summary.....	92
6. Conclusions.....	93
Appendix.....	94
A. Derivation of formula for integrating in situ profile.....	94
B. Derivation of formula for correcting airmass-dependent artifact.....	95
List of Tables.....	97
List of Figures.....	98
Publications.....	105
References.....	106
Acknowledgments.....	117

1. Introduction

1.1 Sources and sinks of atmospheric CH₄

CH₄ is the second most important anthropogenic greenhouse gas in the atmosphere and one of the concerns of this thesis. CH₄ is produced in several processes, including both natural and anthropogenic processes. The geographic distribution and strength of each source differ from the others, and could change with time depending on human activities (e.g. industry, agriculture) or climate conditions (e.g. temperature, humidity and flood). They are showed in Fig. 1.1 and described in the following.

Natural wetlands: Natural wetlands are the largest natural sources of CH₄. According to oxygen condition wetland ecosystems can be classified into an aerobic zone and an anaerobic zone below it. Organic carbon in the soil is broken down to simple substrates through microbial processes at first. Then the end products of these preparing steps are used by methanogen communities to produce CH₄ in the anaerobic zone. There are three paths, named diffusion, ebullition and plant-mediated transport for CH₄ produced in the anaerobic zone to leave into the atmosphere. There usually exists a gradient of CH₄ concentration from the anaerobic zone to the soil surface, which can result in an upward diffusion of CH₄. The diffusion path passes the aerobic zone where a lot of CH₄ is consumed by methanotrophic communities. In the ebullition process CH₄ is taken out of the wetland in the form of gas bubbles, which avoids the oxidation of CH₄ in the aerobic zone. The transport of CH₄ from the wetland to the atmosphere by the ventilation system of plants bypasses the aerobic zone as well. Among the three paths the diffusion contributes least to the CH₄ emission from wetlands.

The estimated wetland CH₄ emissions range from 80 to 280 Tg CH₄ yr⁻¹, have a median value of 164 Tg CH₄ yr⁻¹ (Bridgham et al., 2013). The global area of wetlands ranges from 7.1 to 26.9×10^6 km² for model simulations, and from 4.3 to 12.9×10^6 km² for observations (Melton et. al., 2013). The zonal sum of wetlands area simulated by models peaks in the tropics and around 60°N. For zonally summed CH₄ emissions, both models and observations reveal two peaks in the tropics and around 60°N as well, and the former is much larger (Spahni et. al., 2011; Melton et. al., 2013). The strong emissions of CH₄ in the tropics are mainly attributed to South American, and the one around 60°N to northern peatlands. The CH₄ emissions from wetlands depend on ecosystem hydrology, soil and vegetation characteristics, and they are believed to be sensitive to climate conditions. For example, it is stated that wetland emissions dominated the substantial interannual variability of CH₄ sources between 1984 and 2003 (Bousquet et. al., 2006). In a model study, a large fraction of the global and tropical variability in wetland CH₄ emissions can be attributed to El Niño/Southern Oscillation (ENSO) between 1950 and 2005.

Fresh water: Fresh waters include lakes, rivers and reservoirs, and have similar CH₄ production mechanisms and emission pathways except for reservoirs, for which there are additional pathways (downstream dam emissions). The estimated CH₄ emission from fresh water is about 93 Tg CH₄ yr⁻¹

resulted by ebullition and diffusive flux. Among these fluxes lakes, reservoirs and rivers contribute about 71.6, 20.0 and 1.5 Tg CH₄ yr⁻¹, respectively (Bastviken et. al., 2011). In addition, there is about 10 Tg CH₄ yr⁻¹ flux from plant-mediated transport.

Biomass burning: The fires of savanna, woodland, deforestation, forest, agriculture and peat release the chemical compounds of burning vegetation. Most of the emissions contain carbon in the form of CO₂ and CO (about 90%). The rest of the carbon is emitted in the form of CH₄, other gases, and smoke particles. These chemical gases and particles have import influence on tropospheric chemistry and climate. The strength of emissions depends on area burnt, potentially burnable vegetation, emission factor and burning efficiency. The emission factor relates the emission of a particular species to the amount of fuel burned, and depends on the type of biomass burning and species. For CH₄ the emission factor is largest for peat fires, agriculture waste burning and tropical forest fires (Werf et. al., 2010; Andreae and Merlet, 2001). Burning efficiency describes the combusted fraction of burnable vegetation, and depends on the type of ecosystem and season. Fire carbon emissions are about 2000 Tg C yr⁻¹, in which grasslands, savannas and woodlands contribute 60%. The geographic distribution of carbon emission has maxima in Africa where savannas dominate, the northern part of South America and Equatorial Asia where deforestations dominate (Werf et. al., 2010). The CH₄ emissions mainly come from Africa (36%), Southeast and Equatorial Asia (32%), Tropical America (16%) and Boreal (10%). The total emissions of CH₄ are estimated to be 11-53 Tg CH₄ yr⁻¹ (Crutzen and Andreae, 1990).

Termites: The emissions of CH₄ from termites is a balance between the production in the colony of termites and oxidation by bacteria during emission into the atmosphere. The estimated amount of CH₄ emissions are 1.5-7.4 Tg CH₄ yr⁻¹ (Sugimoto and Inoue, 1998).

Geological: Geological sources of CH₄ include emissions from ocean and lithosphere. The ocean contributes about 0.6-1.2 Tg CH₄ yr⁻¹ (Rhee et. al., 2009). The CH₄ in the lithosphere is produced through several precesses, microbial CH₄ production, thermogenic CH₄ production and gas hydrates. After the production, they can bypass the water column in the ocean in the form of bubbles and enter the atmosphere, dissolve in ocean, or be released into the atmosphere by volcanoes. The amount of CH₄ entering the atmosphere produced in the lithosphere is 42-64 Tg CH₄ yr⁻¹ (Etiope et. al., 2008).

Agriculture and waste: The agriculture sources of CH₄ include enteric fermentation, rice cultivation, manure management and agriculture soils. The waste sources of CH₄ include landfilling of solid waste, wastewater and some other processes. The emissions by these CH₄ sources are 187-224 Tg CH₄ yr⁻¹ (Kirschke et. al., 2013).

Fossil fuels: This category relates to the energy need of humankind. It includes natural gas and oil system, coal mining activities, stationary and mobile combination and other processes. The strength is 85-105 Tg CH₄ yr⁻¹ (Kirschke et. al., 2013).

Atmospheric CH₄ is destracted in the troposphere by oxidation with OH, which constructs the sinks of atmospheric CH₄ together with loss to the stratosphere, soils and tropospheric Cl. These

processes are described in the following.

Tropospheric OH: Atmospheric OH radical is produced by two steps, the production of O(¹D) (the O atom in an excited singlet state) through photolysis of O₃ by ultraviolet solar radiation, the produced O(¹D) reacts with H₂O molecule and produces OH. The concentration of OH depends on the strength of ultraviolet radiation, the concentration of O₃ and H₂O. CH₄ reacts with OH in the manner:



There are several reactions following (1.1), and final products are CO₂, H₂O, O₃, OH and HO₂. There is plenty of ultraviolet radiation in the stratosphere, and much of ultraviolet radiation is absorbed by stratospheric O₃. On the other hand, almost all of atmospheric H₂O stay in the troposphere. The global averaged vertical distribution of OH peaks in the range of 500-700 hPa, with an order of 10⁶ molecules cm⁻³. The latitude distribution of OH presents a maximum between 30°S and 30°N, which changes following the seasonal shift of maximum solar radiation. The maximum of OH concentration in lower tropical troposphere results from high H₂O concentration, strong solar radiation and low O₃ column overhead there. The amount of CH₄ consumed by tropospheric OH is 430-587 Tg CH₄ yr⁻¹ from models study (Naik et. al., 2013).

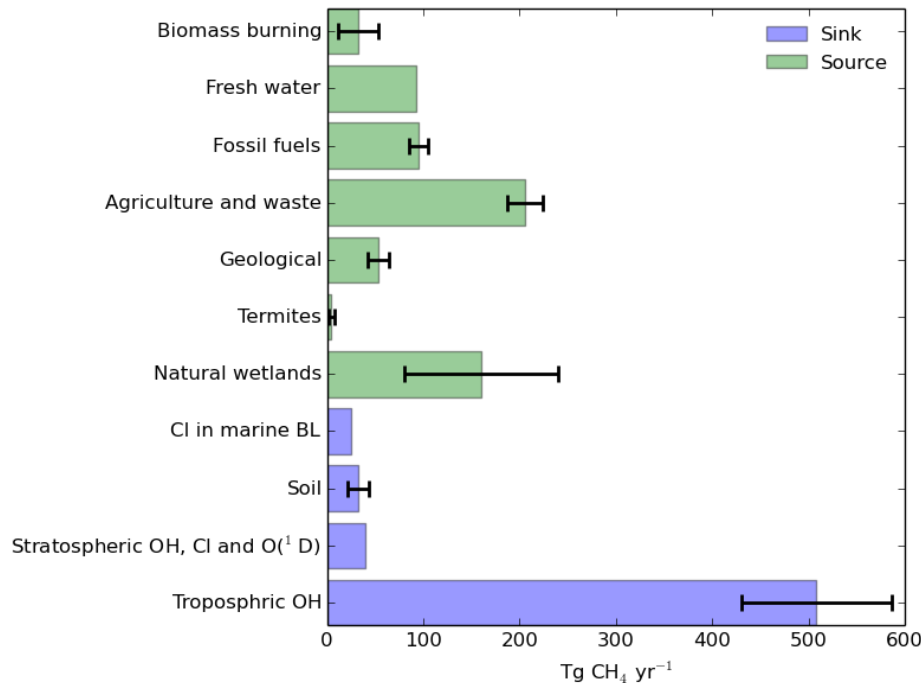


Figure 1.1. Sources and sinks of atmospheric CH₄ with errorbar indicating spread of the reported values. There are no uncertainties given for the fresh water and Cl in marine BL because their measurements are rare.

Stratospheric consumption: CH₄ can be transported up to the stratosphere and consumed by OH, Cl atoms and O(¹D). The reaction of CH₄ with OH is an important source of stratospheric H₂O. The stratospheric sink of CH₄ is commonly assumed to be about 40 Tg CH₄ yr⁻¹.

Soil: Except for chemical destruction of CH₄ in the atmosphere, soil can uptake CH₄ as well. Uptake of CH₄ in soil occurs via oxidation by specialized aerobic bacteria. The magnitude of soil sink derived from model is about 28 Tg CH₄ yr⁻¹ (Curry, 2007), and 22-44 Tg CH₄ yr⁻¹ from measurements (Dutaur and Verchot, 2007).

Cl in the marine boundary layer: According to the model simulation (Allan et. al., 2007) Cl atoms in the marine boundary have a concentration of 18×10^3 atoms cm⁻³, and oxidize 25 (range 13-37) Tg CH₄ yr⁻¹.

1.2 Atmospheric properties and CH₄ transport

The earth-atmosphere system receives its energy from solar radiation. The atmosphere is a thin layer of gas constrained to earth surface by gravity. The spectrum of solar radiation can be described well by a flux distribution function for a blackbody with a temperature of 5800 K. Solar radiation distributes mainly between 0.2 and 3 μm and has maximum at about 0.5 μm. Part of this incoming radiation is reflected back to space by the earth's surface and atmosphere, and the residual is absorbed and reemitted by the earth-atmosphere system.

The atmosphere is mainly composed of N₂, O₂ and Ar, these three gases contribute 99.93% totally in dry air (Jacob, 1999, p. 2). Besides these gases the atmosphere contains trace gases, e.g. CO₂, Ne, O₃, He, CH₄, Kr, H₂, N₂O, H₂O, CO, hydrocarbons and chlorofluorocarbons (CFCs). A molecule absorbs or emits radiation through changing its internal state, which includes electronic, vibrational and rotational states. The state of a molecule is quantized and therefore its absorption or emission is selective. The energy associated with the change in molecular states decreases for electronic, vibrational and rotational states sequentially. They correspond to ultraviolet, near-infrared and far-infrared regions respectively. The change in the molecular state can occur independently for each type or in a combination of them. The symmetries of N₂, O₂, and Ar molecules forbid a radiation-induced change in their vibrational and rotational states (Goody and Yung, 1989, p. 74). As a result, there is no absorption in the near-infrared region from them. In the ultraviolet region O₂ has important absorption, as well as O₃. All the minor constituents of the atmosphere absorb in the near-infrared region and H₂O dominates the absorption in the far-infrared region (Goody and Yung, 1989, p. 68).

The capture of the energy associated with solar radiation is accomplished through interaction between the earth surface and the atmosphere. About 46% of incoming solar radiation is absorbed directly by the earth surface and 19% by the gases O₃, H₂O, O₂, and CO₂ (Mitchell, 1989). If the earth-atmosphere system is taken as a blackbody then such amount of input energy flux will give an effective emission temperature of 255 K (the effective emission temperature is a temperature under

which the Stefan-Boltzmann law predicts an amount of emission radiation same as absorbed one). This low-temperature earth-atmosphere system emits radiation having wavelengths longer than 4 μm . In a stable earth-atmosphere system, the incoming solar radiation is balanced by the sum of reflected solar radiation and thermal radiation from the earth-atmosphere system at the top of the atmosphere. The effective emission temperature of the earth-atmosphere system is much lower than observed temperature at the earth surface. The earth surface absorbs solar radiation and then emits thermal radiation. The minor constituents of the atmosphere, H_2O , CO_2 , O_3 , N_2O , CH_4 and CFCs, have significant absorption in the infrared region. A fraction of the thermal radiation from the earth surface is absorbed by these minor constituents. The atmosphere emits thermal radiation up to space and down to the earth surface. The earth surface is nearly a blackbody in the infrared region, and absorbs almost all of the downward radiation from the atmosphere. As a result, the earth surface receive more radiation than directly absorbed solar radiation and has a higher temperature than the effective emission temperature of 255 K. This effect of the atmosphere is known as the greenhouse effect. The atmospheric gases that contribute to this effect are called greenhouse gases (GHGs). Different gases have different strength for the greenhouse effect. The strength is determined by the absorption wavelengths, the strength of the absorption line, the concentrations and absorption efficiency of other gases in the same wavelengths. In the current state of the atmosphere, important GHGs are H_2O , CO_2 , CH_4 , N_2O , O_3 and CFCs, their contributions decreases in turn (Mitchell, 1989). The increases in the concentrations of GHGs will warm the earth surface, therefore there is much concern about the increasing GHGs in the atmosphere.

The atmosphere is adhered to the earth surface by gravity. In vertical direction the atmospheric density decreases exponentially, and about 99.9% of its mass locates below 50 km (comparing to the earth radius of 6371 km). According to the thermal structure of the atmosphere in vertical direction, the atmosphere is usually classified into four layers, troposphere, stratosphere, mesosphere and thermosphere (Fleagle and Businger, 1980, p. 79-84). The troposphere extends from the surface to 8-18 km depending on latitude and season. About 80% of the atmospheric mass is located in the troposphere. Temperature decreases with altitude in this layer at a typical rate of 6.5 K/km. The atmosphere is statically unstable in most cases in the troposphere, and convection occurs to adjust the vertical distribution of its temperature. The stratosphere extends from the top of the troposphere to about 50 km. Atmospheric temperature increases in the stratosphere, and the atmosphere is statically stable. Consequently, the atmospheric motions are mainly in horizontal direction in the stratosphere. In the mesosphere from 50 km to about 85 km, the temperature decreases with altitude similar to the troposphere. Above the mesosphere is the thermosphere, and the temperature increases until about 250 km and then becomes almost constant with altitude. The constant temperature has large variability from 1000 to 2000 K, which is related to solar activities.

The thermal structure of the atmosphere as described above can be understood approximately in term of radiative equilibrium and radiative-convective models (Goody and Yung, 1989, p. 388-420). In the radiative equilibrium model it is assumed that solar heating rates are equal to the thermal cooling rate at each height level. Solar radiation downward to the atmosphere is equal to thermal

radiation upward to space at the top of the atmosphere. At the earth surface the sum of solar and thermal radiation downward to ground is equal to that upward through the atmosphere. Assuming the absorption of solar radiation by the atmosphere is homogeneous, atmospheric temperature calculated based on the assumption of radiative equilibrium decreases monotonically with altitude. If taking the absorption of solar radiation by atmospheric gases into account, which varies with altitude, the calculated atmospheric temperature increases above 10 km for an average condition at 40°N. This feature corresponds to the vertical distribution of temperature in the troposphere and the stratosphere. Another difference from accounting for the gas's absorption is that the temperature decreases faster with height near to ground. When dividing absorption and emission of solar and thermal radiation into contributions from various gases, it shows that the increase of atmospheric temperature in the stratosphere is caused by absorbing solar radiation by O₃. In the troposphere, especially lower troposphere, the absorption of solar radiation by H₂O heats atmosphere as well. The heating of O₃ and H₂O is balanced by thermal cooling of H₂O and CO₂. The lapse rate of the temperature from the radiative equilibrium model is too large in the troposphere to be statically stable. Convection must develop to adjust the vertical distribution of tropospheric temperature until the atmosphere is statically stable. In a simple radiative-convective model, the upward heat flux can be related to the difference of the lapse rate given by radiative equilibrium and a prescribed neutral lapse rate (It is 6.5 K/km based on observation).

CH₄ is emitted at the earth surface and mixed upward into the atmospheric boundary layer (It usually extends from ground to 1-2 Km) through turbulence in 1 day, or several hours under condition with strong convection driven by solar heating at ground. The transport of CH₄ into middle and upper troposphere is accomplished by convective motions caused by the instability in the troposphere. The convective motion is stronger over the continents than over oceans because of the larger heat capacity of water, therefore the vertical mixing of CH₄ is more efficient over the continents. The vertical motion can be driven by horizontal motion as well. For example, the upward branch of the Hadley cell is driven by horizontal convergence at tropics. The vertical transport of CH₄ in the free troposphere occurs at much larger spatial scales compared to the turbulence in the atmospheric boundary layer. The temporal scale associated with the vertical transport in the free troposphere is about one month (Jacob, 1999, p. 67). The efficiency of horizontal transport of CH₄ in the free troposphere is different for different directions. The latitudinal transport of CH₄ is much faster than meridional transport in the same hemisphere. Temporal scale is about 2 weeks for the latitudinal transport and 1-2 months for the meridional transport in each hemisphere. There is a strong barrier for the meridional transport at the intertropical convergence zone (ITCZ). The ITCZ is a persistent convergence belt near the equator formed by the southward branch of the northern Hadley cell and northward branch of the southern Hadley cell (Holton, 2004, p. 371-374). There is a strong ascending motion at the ITCZ throughout the year and divergence in the upper troposphere. The position of the ITCZ varies seasonally and along longitude, and is located at a latitude with a maximum temperature of the earth surface in meridional direction. Generally the ITCZ is in the warmer part of two hemispheres. Meridional motion in the troposphere is basically driven by latitudinal gradients of the earth surface

temperature. Around the ITCZ such gradients are absent and then motion crossing the ITCZ is weak. The typical time is about 1 year for air to exchange between northern and southern hemisphere. The ITCZ is a realistic boundary separating the air of the two hemispheres. The lifetime of CH₄ in the troposphere is about 10 years, much longer compared to the temporal scales of the tropospheric transport in each hemisphere. It can be expected that CH₄ is well-mixed in the troposphere of each hemisphere.

As described earlier, the atmospheric temperature decreases with altitude in the troposphere and arrives at a local minimum at the tropopause. In the stratosphere located just above the tropopause the atmospheric temperature increases with altitude. The strong static stability of the stratosphere prevents convective motions originating in the troposphere from continuing into the stratosphere. The transport from the troposphere to the stratosphere is mainly accomplished by ascending motions in the tropics. The typical time for air to ascend into the stratosphere is 5-10 years. The air ascending into the stratosphere is taken toward the poles and subsides back into the troposphere at mid to high latitudes. The circulation is called stratospheric residual circulation, which is driven by eddy-induced zonal force in the stratosphere (Holton 2004, p. 407-421), in contrast to the thermally driven tropospheric circulation. CH₄, as well as other long lived species such as N₂O, are distributed mainly by the transport, and present similar patterns in the stratosphere. It takes 1-2 years for air to move back into the troposphere. Because of the slow transport from the troposphere to the stratosphere and the destruction in the stratosphere, the concentration of CH₄ is much lower in the stratosphere than in the troposphere and deceases with altitude above the tropopause with height owing to increased oxidations by radicals.

The geographic distribution of atmospheric CH₄ is a combination effect of atmospheric transport, sources and sinks. Satellites are a useful tool to visualize the global distribution of CH₄, as being shown in Fig. 1.2. Higher CH₄ concentration in northern hemisphere compared to southern hemisphere is a result of most of CH₄ sources locate in the northern hemisphere, slow transport between two hemispheres and rapid mixing in each hemisphere relative to the long lifetime of CH₄. The boundary between high and low CH₄ concentrations approximately denotes the mean position of the ITCZ. Several regions present higher CH₄ concentrations relative to the surrounding, for example, South America, middle Africa, East Asia and Russian. Some important CH₄ sources exist in these regions, which are wetlands, biomass burning, rice cultivation and boreal wetland, respectively. The long-term trend and seasonal variation of CH₄ depend on a balance between seasonal cycles of its sources and sinks. Fig. 1.3 presents zonally averaged CH₄ over time and latitude, derived from in situ measurements at the earth surface (mostly in marine boundary layer). Regions in mid- to high-southern latitudes are far from any strong sources, and then present a well mixed CH₄ field. The seasonal cycles there are really regular compared to significant interannual variability in northern hemisphere. The reasons are that the seasonal variation of OH dominates the seasonal cycle of CH₄ in southern hemisphere, but more factors (transport, sources and sinks) influence northern CH₄ cycle.

Methane SCIAMACHY/ENVISAT 2003-2005

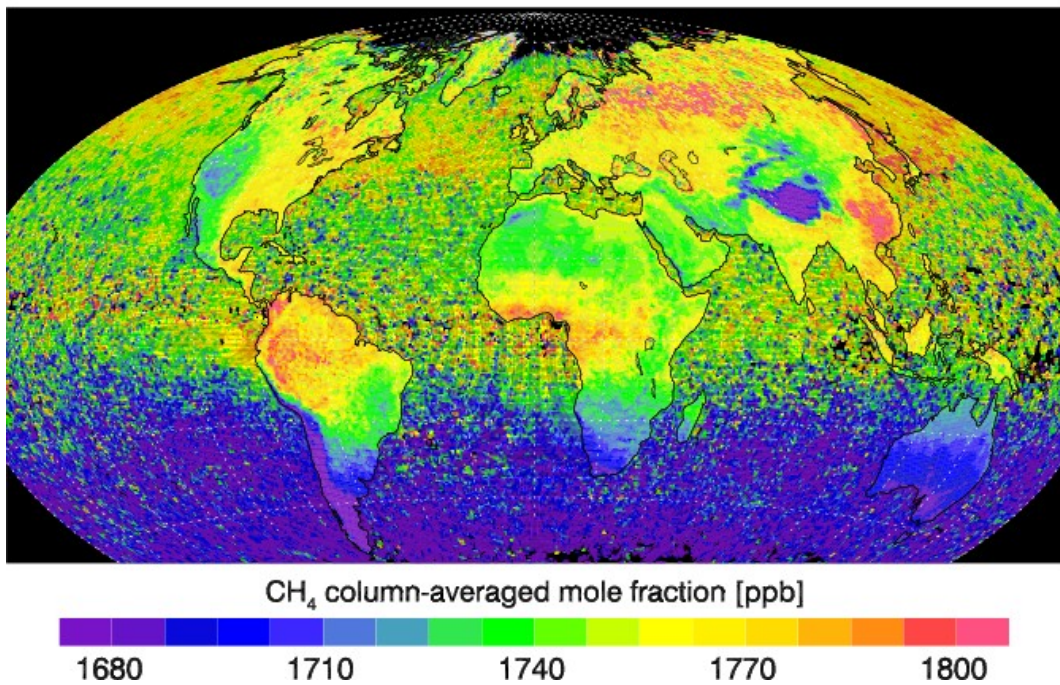


Figure 1.2. Satellite measurements of column-averaged CH₄ concentration for 2003-2005. [Courtesy of M. Buchwitz, IUP, University of Bremen.]

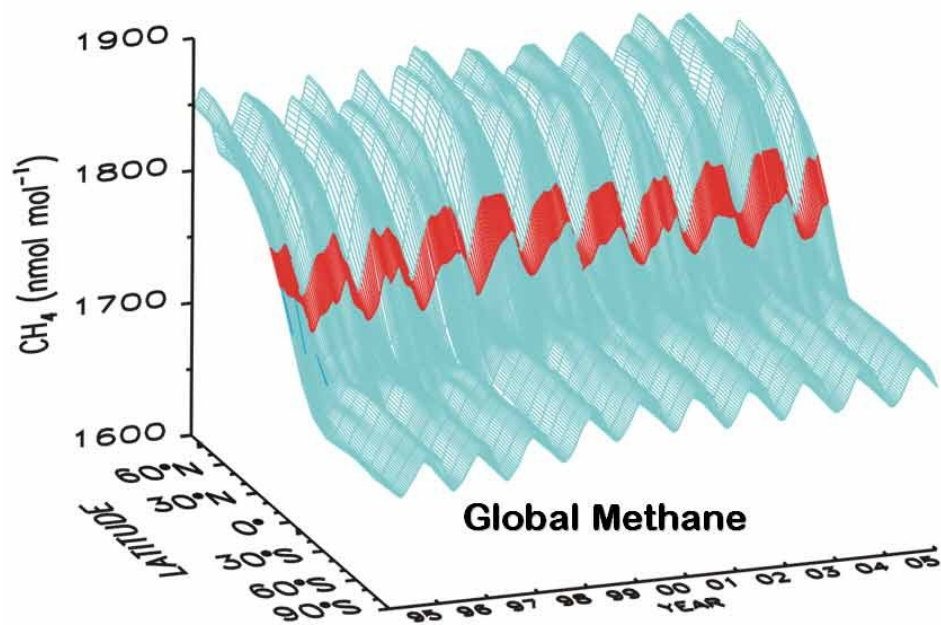


Figure 1.3. Zonally averaged representation of the global distribution of CH₄ at the earth surface (mostly in the marine boundary layer). [Courtesy of NOAA/ESRL.]

Although the categories of CH₄ sources and sinks are known quite well, but their magnitudes are poorly known up to now. The large uncertainties of sources and sinks limit the ability of model to predict CH₄ variation in the future.

1.3 Ground-based observation of greenhouse gases by TCCON

It is important to monitor the temporal and spatial variation of greenhouse gases because of their climate effects. The Total Carbon Column Observation Network (TCCON) is a network of ground-based Fourier Transform Spectrometers (FTS) measuring atmospheric trace gases. The ground-based FTS records solar spectra at ground level in the near-infrared spectral region, where H₂O, CO₂ and CH₄ have significant absorption features, and CO, N₂O and HF absorb solar radiation as well. According to their absorption features the column-averaged concentrations of these species can be derived. The aimed precision of TCCON measurements is 0.1%, which can be achieved under clear sky condition. The high precision measurements can be used to validate measurements of satellite and model simulations.

The global sources and sinks of greenhouse gases are usually derived from top-down and bottom-up approaches. The top-down approach determines optimal surface fluxes that agree with measurements best. The surface fluxes are transformed to atmospheric concentrations of greenhouse gases using a chemical transport model. The bottom-up approach is a process-based model, which determines surface fluxes through directly describing various mechanisms influencing fluxes. The performance of the top-down approach depends on measurement quantity and simulating ability of chemical transport model. TCCON measurements can act as an independent validation for the top-down approach, or validate surface flux from the bottom-up approaches using chemical transport model.

The first part of this thesis describes the derivation of tropospheric column-averaged CH₄ concentration using TCCON column data of CH₄ and N₂O. There is much lower CH₄ concentration in the stratosphere compared to the troposphere. The variabilities of the tropopause and stratospheric CH₄ cause variabilities of the column-averaged CH₄ concentrations. Currently numerical models have difficulties in simulating tropopause variabilities and some stratospheric processes, for example the polar vortex. If the tropospheric column-averaged CH₄ is used, such difficulties can be avoided.

The second part of this thesis is about the retrieval of the $\delta^{13}\text{C}$ in atmospheric CO₂ from TCCON spectra. One difficulty of the top-down approach to estimate sources and sinks of greenhouse gases is the attribution to different categories. Taking isotopes measurements of greenhouse gases into account is a way to improve it. For example, CO₂ produced by fossil fuel burning contain higher ¹³C than by biosphere.

2. Methods

2.1. Fourier transform spectrometry

The Fourier transform infrared spectrometry (FTS) records the interference pattern of incident light. The incident light is split into two beams and then combined together. The intensity of the combined light depends on the difference of the paths from splitting to combination of two beams, and the spectrum of the incident light. The FTS records the variation of the intensity of the combined light along the difference of the paths, namely interferogram. The spectrum can be recovered from the interferogram.

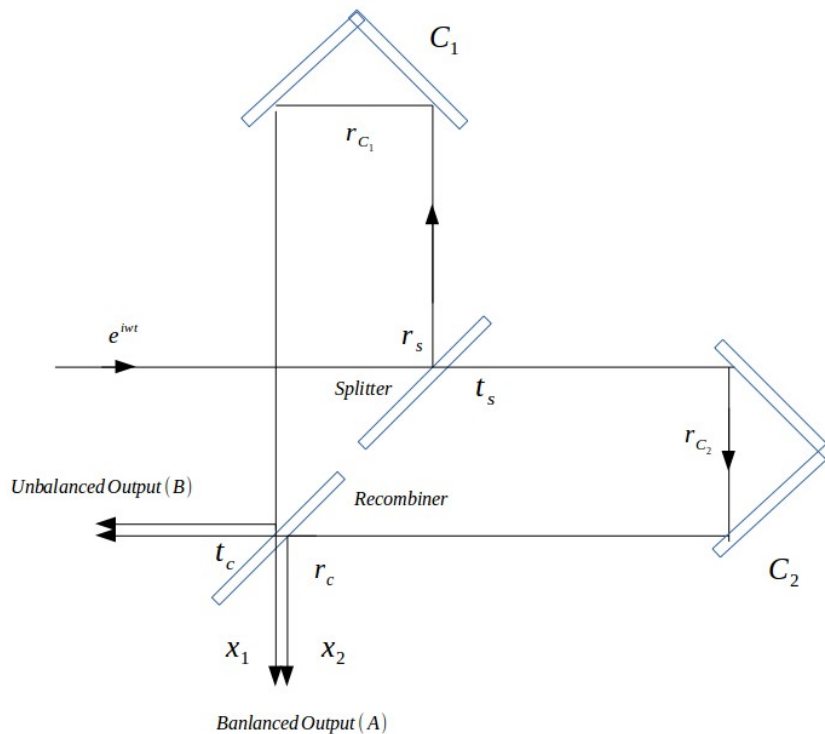


Figure 2.1. Diagram sketch of a Fourier transform infrared spectrometry. r and t represent reflection and transmission coefficients, their subscripts denote corresponding object. x_1 and x_2 are paths of two beams.

The working principle of the FTIR can be described by Fig. 2.1. Assuming incident light is monochromatic and can be described as e^{iwt} , then the balanced output A can be described as,

$$A = e^{iwt} (t_s r_{C_2} r_c e^{-i2\pi\sigma x_1} + r_s r_{C_1} t_c e^{-i2\pi\sigma x_2}),$$

where, σ is an inverse of the wavelength. If ignoring the differences of reflection and transmission coefficient between different objects, the intensity of the balanced output is,

$$E = A^* A = 2r^4 t^2 (1 + \cos 2\pi \sigma x), \quad (2.1)$$

where r and t represent reflection and transmission coefficients, and $x = x_2 - x_1$. Since the constant term in the bracket of Eq. 2.1 is not important, the intensity of the balanced output is basically proportional to the cosine of the path difference. When the incident light contains various frequencies and has a spectrum $B(\sigma)$, the intensity of the balanced output, the interferogram, is,

$$I(x) = \int_0^\infty B(\sigma) \cos 2\pi \sigma x d\sigma.$$

The multiplier and constant term in Eq. 2.1 has been left out during deriving above equation. So the interferogram recorded by the FTS is a cosine transform of the spectrum. The spectrum can be recovered by taking the interferogram's cosine transform. Usually the equation above is written as,

$$I(x) = \int_{-\infty}^\infty B_e(\sigma) \cos 2\pi \sigma x d\sigma; \quad B_e(\sigma) \equiv \frac{1}{2}(B(\sigma) + B(-\sigma)). \quad (2.2)$$

Conversely, for an ideal interferogram there is,

$$B_e(\sigma) = \int_{-\infty}^\infty I(x) \cos 2\pi \sigma x dx.$$

The reason for extending to minus frequency is an easier mathematical manipulation of Eq. 2.2 in analysis of a non-ideal interferogram.

While the relation between a spectrum and an interferogram is clear, there are several limitations in the real observation. The path difference is limited for a real FTS. It is equivalent to multiply $I(x)$ by a rectangle function with a width of twice the maximum path difference. In spectrum domain, it means a convolution of $B_e(\sigma)$ with a sinc function. The width of the sinc function is inversely proportional to the maximum path difference, and is an indication of the resolution in the spectrum. Moreover, a FTS has a finite aperture. The path difference of the combined beams varies with the distance of hitting point on the aperture off the center. The recorded $I(x)$ at a specific path difference actually contains contributions from other path differences. The effect on a spectrum is a convolution by a rectangle function of width proportional to wavenumber and the aperture size. These effects of physical limitations of the FTS on the spectrum is combined into a convolution function, namely the instrumental line shape function (ILS). The ILS characterizes how a real spectrum is smeared into an observed one.

The performance of a FTS can not be ideal, and suffers various deficiencies. One common error is inaccurate knowledge on the position of the moving mirror in Fig. 2.1. Its effects on the spectrum depend on its distribution along the path difference. For example, a periodic error in x will result in false lines locating off from the true line. Other examples are that the response of instrument to signal intensity changes with path difference (usually decreases with path difference) and the aperture is not centered on the optical axis. As a result, the real ILS differs from the nominal one

accounting for the limited path difference and aperture only. Additional measurements have to be taken to determine what it is.

2.2. Retrieval theory and methods

Retrieval is a process of deriving the quantities which are interested for us from indirect measurements. There are usually more than one solution which predict comparable measurements within the measurement error. The reason is that any physical measurement has error, and some components of the quantity interested might have none or little effect on the measurement. The components of the quantity interested which do not exit in the measurement must be obtained from other sources. Even for the components existing in the measurement it is usually better to apply some constraints since the measurement error always come and could distort a solution seriously. Knowledge about the quantity that is independent from the measurement is called *a priori*. With the measurement and *a priori* on the hand, approaches are needed to combine information presenting in the measurement and *a priori*. The principle of such approaches should be minimizing the influence of the measurement error and extracting as much as possible information from the measurement.

Bayes's theorem provides a useful conceptual frame for retrieval problems. It can be expressed as,

$$P(x|y) = \frac{P(y|x)P(x)}{P(y)}, \quad (2.3)$$

where x and y represent a state (quantities interested) and measurement, respectively. P means probability density function (*pdf*). $P(x)$, $P(y)$ are *a priori pdf* of the state and measurement. $P(y|x)$ is the *pdf* of the measurement when the state takes the value of x . $P(x|y)$ is the *pdf* of the state when the measurement has the value of y , called *a posterior pdf* of the state. The Bayes theorem gives an explicit expression on how does knowledge on the state change with the measurement available. Assuming both the measurement error and the state have a Gaussian distribution, and ignoring the term $P(y)$ since it is just a scale factor then Eq. 2.3 can be written as,

$$-2\ln P(x|y) = (y - f(x))^T S_\epsilon^{-1} (y - f(x)) + (x - x_a)^T S_a^{-1} (x - x_a) + c, \quad (2.4)$$

where, both x and y are vectors that represent the state and measurement. $f(x)$ is a forward function which describes how the state is related to the measurement. The superscript T means transpose. S_ϵ and S_a are the measurement error covariance and *a priori* covariance of the state, respectively. x_a is a prior value of the state, c is a constant. It is clear that the *a posterior pdf* of the state contains contributions from both the measurement and *a priori* knowledge. Knowing the *a posterior pdf* of the state, a criterion is needed to select one solution from all states. One reasonable selection is the most probable state. Another could be the expected value of the *a posterior pdf*. The former criterion is used here and applied in most of this thesis.

A numerical procedure should be used to search a solution x minimizing Eq. 2.4 since usually the forward function is a nonlinear and complicated function of the state and the equation can not be

dealt with analytically. At the maximum probability state the derivative of Eq. 2.4 with respect to the state is zero. The Gauss-Newton method is commonly used to obtain the state which zeros the derivative of Eq 2.4. It is an iterative method (Rodgers et al., 2000),

$$x_{i+1} = x_i + (S_a^{-1} + k_i^T S_\epsilon^{-1} k_i)^{-1} [k_i^T S_\epsilon^{-1} (y - f(x_i)) - S_a^{-1} (x_i - x_a)], \quad (2.5)$$

where the subscript i denotes the i th step in the iteration. k is a matrix that contains the derivatives of the forward function to the state, with elements $k_{ij} = \partial f_i / \partial x_j$, the subscripts here mean the i and j th elements of vector x and vector-valued function f . When the iteration converges to a state \hat{x} the Eq. 2.5 can be written as,

$$\hat{x} = x_a + \hat{G} [y - f(\hat{x}) + \hat{k}(\hat{x} - x_a)], \quad \hat{G} = (S_a^{-1} + \hat{k}^T S_\epsilon \hat{k})^{-1} \hat{k}^T S_\epsilon^{-1}. \quad (2.6)$$

Except for obtaining a solution, it is even more important to characterize this solution. For example, how far is the solution from the true state, how sensitive is the solution to the measurement error. Especially for remote sensing the solution usually is some function of the true state, such relation needs to be determined as well. Since the solution contains information from both the measurement and the a prior it is necessary to know how much information is taken from the measurement.

Assuming the forward function is linear in a region around \hat{x} , within which the true value of the state x locates. It means $y = f(\hat{x}) + \hat{k}(x - \hat{x}) + \epsilon$, ϵ is the measurement error. The expression for the solution Eq. 2.6 can be written as,

$$\hat{x} = x_a + \hat{G} [\hat{k}(x - x_a) + \epsilon]. \quad (2.7)$$

According to Rodgers (2000), the expected value of the first terms in Eq. 2.4 at the solution is defined as degrees of freedom for signal, that of the second term as degrees of freedom for noise.

$$\begin{aligned} d_s &= E[(\hat{x} - x_a)^T S_a^{-1} (\hat{x} - x_a)] = \text{tr}(\hat{G} \hat{k}) \\ d_n &= E[(\hat{k}(x - \hat{x}) + \epsilon)^T S_\epsilon^{-1} (\hat{k}(x - \hat{x}) + \epsilon)] = \text{tr}([\hat{k}^T S_\epsilon^{-1} \hat{k} + S_a^{-1}]^{-1} S_a^{-1}), \end{aligned} \quad (2.8)$$

where, E means calculating an expected value and tr means calculating a trace of a matrix. The sum of d_s and d_n is equal to the dimension of the state vector. When a prior constraint, described by S_a , is tight the solution will approach the a prior value of the state and d_s will decrease. At the same time the degrees of freedom for noise will increase, which means the measurement mainly provides noise information.

Except for the state, a forward function is determined by many other parameters. For example, in the case of retrieving CO₂ profiles from a ground-based FTS measured spectra the CO₂ profiles will be the state. But other parameters impact spectra as well, like atmospheric temperature, pressure and water profiles, solar position, instrument parameters, spectroscopy parameter of all molecules contributing to absorption in a used spectral region. It is also possible that some factors are still not recognized and not included in the forward function. The knowledge on the recognized parameters of the forward function can not be completely correct in practice. The forward function must be

replaced by a likely imperfect forward model F , which could have not completely correct model parameters. Its relation to the forward function is,

$$f(x, b, b') = F(x, \hat{b}) + K_b(b - \hat{b}) + \Delta f(x, b, b'), \quad (2.9)$$

where, b collects recognized model parameters and b' includes unknown parameters. K_b is the derivative of $F(x, b)$ to the model parameters at their estimated value \hat{b} . Δf is the error in the forward model caused by the unknown parameters. As a result, the f and k in Eq. 2.5 and 2.6 must be replaced by $F(x, \hat{b})$ and its derivatives to the state K , respectively, in practice. The solution obtained when using the forward model F has properties different from that described in Eq. 2.7 and 2.8. They are explained as follows, use a relation $y = f(x, b, b') + \epsilon$ and rewrite Eq. 2.6 in terms of F and K ,

$$\hat{x} = x_a + \hat{G}[f(x, b, b') - F(\hat{x}, \hat{b}) + \hat{K}(\hat{x} - x_a) + \epsilon].$$

Then insert Eq. 2.9 into the equation above, and expand $F(x, \hat{b})$ at \hat{x} ,

$$\begin{aligned} \hat{x} &= x_a + \hat{G}[\hat{K}(x - \hat{x}) + \hat{K}(\hat{x} - x_a) + K_b(b - \hat{b}) + \Delta f(x, b, b') + \epsilon] \\ &= x_a + \hat{G}\hat{K}(x - x_a) + \hat{G}K_b(b - \hat{b}) + \hat{G}\Delta f(x, b, b') + \hat{G}\epsilon \end{aligned} \quad (2.10)$$

Compared to Eq. 2.7, there are two additional terms contributing to the solution in Eq. 2.10. They are the solution errors caused by the error in the forward model parameters and parameters not included in the forward model. Only the last three terms in Eq. 2.10 are called error term. But the error related to unknown model parameters is not possible to evaluate. The covariances of other two error terms can be derived from the statistical properties of forward model parameters and the measurement error. The first two terms together describe how the solution is related to the true value and a prior value of the state. Especially important is the term $\hat{A} = \hat{G}\hat{K}$, called averaging kernel. The rows of an averaging kernel matrix expand a space, which is a subspace of the state vector space. Only these states located in the subspace can contribute to the solution, or can be measured. The state outside the subspace is orthogonal to all rows of the averaged kernel matrix and then its product with the matrix is a zero vector.

The derivation of the definition of the degrees of freedom for signal and noise in Eq. 2.8 is based on the solution expression of Eq. 2.7. When using a likely imperfect forward model in practice, the solution expression needs to be replaced by Eq. 2.10. The expected value of the second term in Eq. 2.4 at the solution contains more terms than $\text{tr}(\hat{G}\hat{K})$, but only this term is treated as the degrees of freedom for signal d_s . The expression of d_n in Eq. 2.8 needs to be changed as well in this case, but not important in the thesis. So the number of independent pieces of information from the measurement is equal to the trace of the averaging kernel matrix.

To obtain a maximum a posterior solution (that minimize Eq. 2.4) the a prior covariance is needed. A prior covariance can be derived from the direct measurements of the state or constructed through some approximate methods. There is another method to construct a prior constraint, namely

Tikhonov-Phillips regularization, which selects a solution with the most similarity with a prior in the absolute value or difference between the elements of a state vector. These constraints do not have probability-related meaning, result in a solution which is not necessarily most probable. In Tikhonov-Phillips regularization method, usually a function as follows is minimized,

$$(y - F(x))^T S_e^{-1} (y - F(x)) + (x - x_a)^T (\gamma^2 B^T B) (x - x_a), \quad (2.11)$$

where B is a matrix to apply regularization constraints and γ^2 is a scale factor, and for convenience other parameters of F than the state x are omitted. Compared to Eq. 2.4 the inverse a prior covariance is replaced by $\gamma^2 B^T B$, which however is not a measure for probability distribution of the state. The derived properties, e.g. the degrees of freedom for signal and error characteristic, for the maximum a posterior solution is also suitable to this case. The matrix B can be any linear combination of following matrices,

$$\begin{pmatrix} 1 & 0 & 0 \\ 0 & 1 & 0 \\ 0 & 0 & 1 \end{pmatrix}, \begin{pmatrix} 1 & -1 & 0 \\ 0 & 1 & -1 \\ 0 & 0 & 0 \end{pmatrix}, \begin{pmatrix} 1 & -2 & 1 \\ 0 & 0 & 0 \\ 0 & 0 & 0 \end{pmatrix}. \quad (2.12)$$

The example matrices are given in a dimension of 3×3 , but their row and column dimensions should be equal to the dimension of the state vector in practice. The first matrix constraint the absolute value of the state toward the a prior value. The second and third matrix make sure the first and second order differences of the state is close to the differences of the a prior state. The scale factor determines how strong the constraint applied by the matrix B is.

In this thesis, two retrieval codes are applied to get the information of atmospheric greenhouse gases from ground-based FTS measured spectra, namely GFIT and PROFFIT. GFIT is a nonlinear least-squares spectral fitting algorithm (Wunch et al., 2011), which only retrieves the total columns of interested gases. For atmospheric application, a set of a prior profiles of all atmospheric species which have observable absorption feature is prepared. The temperature, water and pressure of the atmosphere is obtained from some additional sources (measurements, reanalysis meteorological data etc.). Spectroscopy parameters of molecule are from HITRAN (Rothman et al., 2010) and some other sources. The forward model in GFIT is a line-by-line calculation of absorption of atmospheric species but ignoring scattering effect of molecule. The absorption line shape of molecule is described by the Voigt function. The retrieval process of GFIT is a minimization of a function having the format of Eq. 2.4, however, only the scale factors to the a prior profiles of atmospheric species is retrieved. PROFFIT is a more flexible inversion code, which allows both scaling the a prior profiles and retrieving profiles of atmospheric species (Hase et al., 2004). The a prior constraint can be the a prior covariance, and the Tikhonov-Phillips regularization matrix. The physical contents in the forward model are generally similar to GFIT. But PROFFIT includes more selections for absorption line shape of molecule, and atmospheric self-emission if needed.

3. Retrieval of tropospheric CH₄ from solar absorption FTS spectra

The atmospheric mole fraction of CH₄ has increased from about 700 ppb to the current atmospheric background of about 1800 ppb since 1770. Despite this dramatic increase, the observed global mean atmospheric abundance was nearly constant from 1999 to 2006, before it began to increase again in 2007 (Rigby et al., 2008; Dlugokencky et al., 2009). This behavior is a subject of open scientific discussion (Bousquet et al., 2011; Pison et al., 2013). Several explanations exist due to large uncertainties in our knowledge on the sources and sinks of CH₄. Usually surface CH₄ and total column-averaged mole fractions of CH₄ (referred to total xCH₄ hereafter) are used in the top-down estimation of the sources and sinks of CH₄. Tropospheric column-averaged mole fractions of CH₄ (referred to tropospheric xCH₄ hereafter) could provide a better constraint in retrieving drivers of CH₄ variations, since the tropospheric xCH₄ is free from influences of stratospheric CH₄.

The tropospheric xCH₄ can be derived using methods such as: (i) a posterior correction to the total column using a proxy for variations in the stratospheric contribution, such as the HF total column as an estimator for the stratospheric CH₄ contribution (Washenfelder et al., 2003; Warneke et al., 2006), as well as (ii) a direct determination of the tropospheric mole fraction of CH₄ via a retrieval of CH₄ profiles (Sepúlveda et al., 2012). Currently the second method is only applied to the Network for the Detection of Atmospheric Composition Change (NDACC) high resolution mid-infrared solar absorption spectra, not to the near-infrared TCCON spectra. The first method is based on the fact that a linear relationship exists in the stratosphere between the mole fractions of CH₄ and HF and that the tropospheric mole fraction of HF exhibits little variabilities, and is indeed approximately zero. The stratospheric column of CH₄ can therefore be inferred from the total column of HF via this linear relationship, and then subtracted from the total column of CH₄ to yield the tropospheric CH₄ column. Variations in the CH₄ column due to changes in surface pressure are determined from the O₂ column. Using this method, the tropospheric xCH₄ can be determined with a precision of 0.5 % (Washenfelder et al., 2003). In this chapter, a new method based on a posterior correction is proposed and tested. The tropospheric xCH₄ using the algorithm developed by Sepúlveda (2012) is also presented as a comparison.

3.1. A posteriori correction method

In the stratosphere, a compact correlation exists between species of sufficiently long lifetime (Plumb et al., 1992). Species whose local lifetimes are longer than quasi-horizontal transport time scales share surfaces of constant mixing ratio, and a scatter plot of the mixing ratio of one versus that results in a compact curve. These correlations have been demonstrated by data sets from both chemical transport models and in situ measurements, such as observations taken from an aircraft platform (Avallone et al., 1997), Atmospheric Trace Molecule Spectroscopy Experiment (ATMOS) observations (Michelson et al., 1998) and balloon observations (Herman et al., 1998). This is true in the case of CH₄ and N₂O in the stratosphere. Hence, using N₂O to infer the stratospheric contribution of the total column of the CH₄ is an alternative approach. This approach is, however, complicated by the fact that N₂O is also present in the troposphere. In this work, we describe a

method to derive the tropospheric $x\text{CH}_4$ in which the stratospheric N_2O column is used to estimate the stratospheric column of the CH_4 . We apply the method to TCCON spectra at four sites, one tropical, two extra-tropical and one polar, and compare it with the results derived with the method using HF.

3.1.1. FTS measurements

Here we use solar absorption FTS measurements at four TCCON stations: Ny-Ålesund (78.9°N , 11.9°E) at Spitsbergen (Palm et al., 2010), Orléans, France (47.97°N , 2.113°E), Bialystok, Poland (53.23°N , 23.025°E) (Messerschmidt et al., 2010, 2012), and Darwin, Australia (12.424°S , 130.892°E) (Deutscher et al., 2010). The near-infrared observations cover the spectral range between 4000 cm^{-1} and $10\,000 \text{ cm}^{-1}$ and were carried out with a CaF_2 beam splitter and a room-temperature InGaAs photodiode. The spectra were analyzed using the retrieval code GFIT. Atmospheric absorption coefficients are calculated line-by-line for each gas in a chosen spectral window, and for each retrieval level using the assumed temperature, pressure and a priori profile in the forward model. All these absorption coefficients together produce the atmospheric transmittance spectrum. The temperature, pressure and water vapor profiles are obtained from National Centers for Environmental Prediction (NCEP) reanalysis data provided by the NOAA/ESRL Physical Sciences Division (Kalnay et al., 1996), and interpolated in time and space from six-hourly data to local solar noon and site latitude/longitude. The simulated spectrum is compared with the measured spectrum and a prior profiles iteratively scaled to minimize the least-squares differences between the calculated and measured spectra. The spectral regions used in this study are the TCCON-standard regions given in Wunch et al. (2010).

3.1.2. In situ measurements

The spatial and temporal variations of tropospheric N_2O need to be known to derive the tropospheric $x\text{CH}_4$ in the posterior correction proposed here. The combined Nitrous Oxide data from the NOAA/ESRL Global Monitoring Division, which is sampled at a set of atmospheric background air sites, is used to derive the global distribution, seasonal cycle and long-term trend of tropospheric N_2O .

To validate the tropospheric $x\text{CH}_4$ derived from FTS measurements, in situ data from several sources is used. At Ny-Ålesund (78.9°N , 11.9°E) in situ CH_4 data is the NOAA surface flask measurements (Dlugokencky et al., 2012) sampled at Zeppelin mountain, which has an elevation of 474 masl compared to the TCCON site's elevation of 20 masl. The relatively high elevation and absence of strong local sources means that these measurements could approximately represent the free troposphere, and are used here in the absence of other more appropriate validation data. Low altitude aircraft flight data is available at Orléans, taken twice per month since 1998 up to 3 km, corresponding to approximately 700 hpa in the pressure coordinate. Over Bialystok there has been regular profiling with semi-monthly to monthly observations using flask sampling at multiple levels up to 3 km for CO_2 , CH_4 , N_2O and other tracers since 2002. These measurements are extended through the entire atmosphere via a linear interpolation between 3.0 km and the tropopause altitude

and assuming the GFIT a priori above that. The tropospheric xCH₄ obtained from the extended low altitude aircraft measurements are used to check the seasonal behavior of the FTS-derived tropospheric xCH₄.

In addition, data from the HIAPER Pole-to-Pole Observations (HIPPO) of Carbon Cycle and Greenhouse Gases Study and Infrastructure for the Measurement of the Europe Carbon Cycle (IMECC) aircraft campaigns is used to calibrate the derived tropospheric xCH₄. HIPPO of Carbon Cycle and Greenhouse Gases Study measured cross sections of atmospheric concentrations of greenhouse gases approximately pole-to-pole, from the surface to the tropopause (Wofsy et al., 2011). A comprehensive suite of atmospheric trace gases pertinent to understanding the Carbon Cycle were measured. The measurements were taken using the High- performance instrumented Airborne Platform for Environmental Research. In this work, the measurements near the TCCON site at Darwin are used. The IMECC project aimed to build the infrastructure for a coordinated, calibrated, integrated and accessible data set for characterizing the carbon balance of the European. The aircraft campaign conducted within the IMECC project was organized by the Max Planck Institute for Biogeochemistry. A Learjet 35 aircraft was equipped with a cavity ring-down spectroscopy instrument (Picarro Inc.) for measuring CO₂ and CH₄ mixing ratios and with a vacuum UV fluorescence analyzer for CO. Profiles were taken from 300 m to 12 000 m over the European TCCON stations, including Bialystok and Orléans, during September and October of 2009 (Geibel et al., 2012).

3.1.3. Theory description

For both HF and N₂O, assuming there is a linear relationship in the stratosphere between their mole fractions, f , and that of CH₄, then

$$f_{CH_4}(z) = a + b f_y(z), \quad (3.1)$$

where, y represents HF or N₂O. Figure 3.1 presents the correlation of the stratospheric mole fractions of HF (left) and N₂O (right) with CH₄ based on retrievals from the ACE-FTS (Atmospheric Chemistry Experiment-Fourier Transform Spectrometer) satellite (Bernath et al., 2005). The deviation of the N₂O-CH₄ relationship from the global fit occurs only when N₂O mole fractions are lower than 50 ppb, and represents a small contribution to the column. For the derivation of a and b , the retrieved stratospheric profiles of HF, N₂O and CH₄ are separated into several 20 degrees wide latitude bands. In case of HF, the latitudinal variation of the slope b ranges from 740 to 870 ppb ppb⁻¹, and from 3.6 to 4.4 ppb ppb⁻¹ for N₂O. Between 2004 and 2010 no discernible time-dependency could be detected. At the four TCCON sites: Ny-Ålesund, Bialystok, Orléans and Darwin the slopes, b , corresponding to their latitude bands are 4.34, 4.39, 4.39 and 3.53 ppb ppb⁻¹, respectively, for N₂O, and -749.05, -751.21, -751.21 and -876.03 ppb ppb⁻¹ for HF. Multiplying both sides of Eq. 3.1 with air density and integrating through the stratosphere yields,

$$VC_{CH_4}^{strat} = a VC_{air}^{strat} + b VC_y^{strat}, \quad (3.2)$$

where VC denotes the vertical column. The stratospheric column of y can be obtained by subtracting the tropospheric column from the total column, so Eq. 3.2 can be rewritten as follows,

$$VC_{CH_4}^{strat} = aVC_{air}^{strat} + b(VC_y - VC_y^{trop}). \quad (3.3)$$

The tropospheric xCH_4 is then calculated as,

$$X_{CH_4}^{trop} = \frac{VC_{CH_4} - VC_{CH_4}^{strat}}{VC_{air}^{trop}}. \quad (3.4)$$

In Eq. 3.3 the tropospheric column of HF is zero. The abundance of N_2O is well-mixed in the troposphere because of its long lifetime (120 years) and the major sink is destruction in the stratosphere. The mole fraction of N_2O is almost constant with respect to altitude in the troposphere. The horizontal distribution of N_2O is fairly uniform with small variability (3-5 ppb) (Kort et al., 2011). In the calculation of the tropospheric column of N_2O , only horizontal and time variations are considered. The NOAA N_2O measurements contain a set of globally distributed sites influenced mainly by atmospheric background air. We approximately separate measured N_2O concentration into three terms: global means of each year, a mean over all years of residual meridional variations relative to the global mean, and means over all years of residual monthly variations relative to yearly mean at a specific latitude. The second and third components are shown in Fig. 3.2. At a specific station and time, the corresponding three components are obtained from interpolations in time and latitudes. Then the tropospheric N_2O concentration is calculated as their sum. With the predicted concentration, the tropospheric column of N_2O is just calculated as its product with the dry air column in the troposphere.

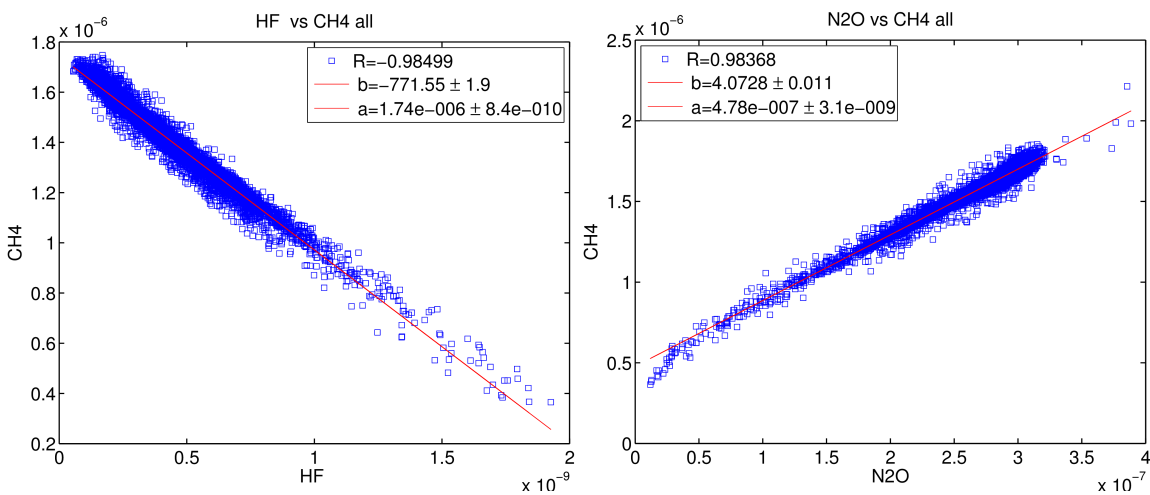


Figure 3.1. Correlations between the stratospheric mole fractions of N_2O (right) and HF (left) with CH_4 on a global scale. Correlation coefficient, slope and intercept are indicated in the legend. The data are from the ACE-FTS satellite.

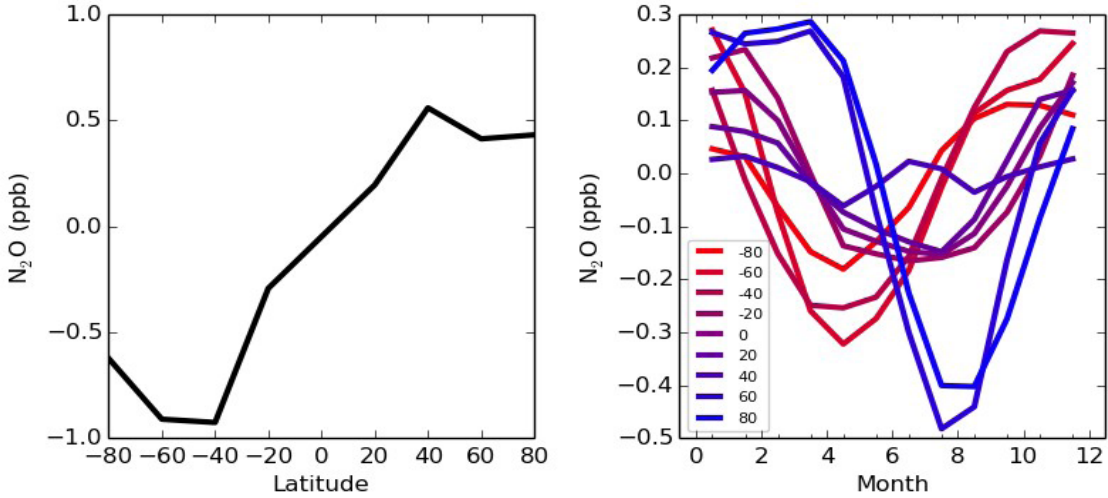


Figure 3.2. The residual yearly mean N_2O at each latitude band relative to globally yearly mean (left), and residual monthly mean N_2O relative to yearly mean at each latitude band (right). The residuals are averaged over all measurement years. The residuals are derived from N_2O data from NOAA/ERSL in situ measurements at ground level.

While Eq. 3.3 and 3.4 are straightforward, the tropopause position is necessary for calculating tropospheric air column. It could cause potential problems since knowledge of tropopause position might be not accurate enough. There is a way to bypass it, as described in the following. In the case of the HF, when approaching the tropopause, the HF concentration approaches zero and so the constant a in Eq. 3.1 represents the CH_4 concentration in the troposphere. Washenfelder et al. (2003) treated a as the tropospheric $x\text{CH}_4$, and use O_2 columns to infer the dry air column. Under these conditions, inserting Eq. 3.3 into Eq. 3.4 yields the equation used by them,

$$X_{\text{CH}_4}^{\text{trop}} = a = \frac{0.2095(VC_{\text{CH}_4} - bVC_{\text{HF}})}{VC_{\text{O}_2}}. \quad (3.5)$$

This method can be used in the N_2O correction approach as well. Since the N_2O mole fraction is almost constant in the troposphere and its value can be quite well predicted, we then subtract the tropospheric N_2O mole fraction from its mole fraction profile in the whole atmosphere. Such a derived “species” is also present completely in the stratosphere, and a linear relationship between the derived “species” and CH_4 mole fractions exists in the stratosphere. But the constant a in Eq. 3.1 is replaced by a value equal to a plus the tropospheric N_2O mole fraction multiplied by the slope b . When the new constant is treated as the tropospheric $x\text{CH}_4$, we get an expression,

$$X_{\text{CH}_4}^{\text{trop}} = \frac{VC_{\text{CH}_4} - b(VC_y - X_y^{\text{trop}}VC_{\text{air}})}{VC_{\text{air}}}, \quad (3.6)$$

where, X_y^{trop} is replaced by $X_{N_2O}^{trop}$ when using N₂O, or set to zero for HF case.

Due to the effect of the averaging kernels the straightforward equation Eq. 3.6 needs to be modified. The total column retrieved by GFIT is a weighted sum of partial columns at retrieval levels. The weights are represented by the averaging kernel, which is a function of the altitude and solar zenith angle, and usually differ from unit. Figure 3.3 presents the averaging kernels of HF, N₂O and CH₄ retrieval at Bialystok from all spectra during 2010. It should be noted that GFIT just scales a prior in the retrieval so the rows of its averaging kernel have the same shape. The showed are the column averaging kernel vector (Connor 2009) instead of the full averaging kernel matrix, which basically is a weighted average of all rows. The shape of the column averaging kernel depends largely on the solar zenith angle. The N₂O averaging kernel has a large weight in stratosphere and small weight in troposphere, so true variations in the stratospheric column of N₂O are amplified in the retrieved total column, and true tropospheric variations are damped. The CH₄ averaging kernel is close to unity at all altitudes, so the effect of the averaging kernel is small.

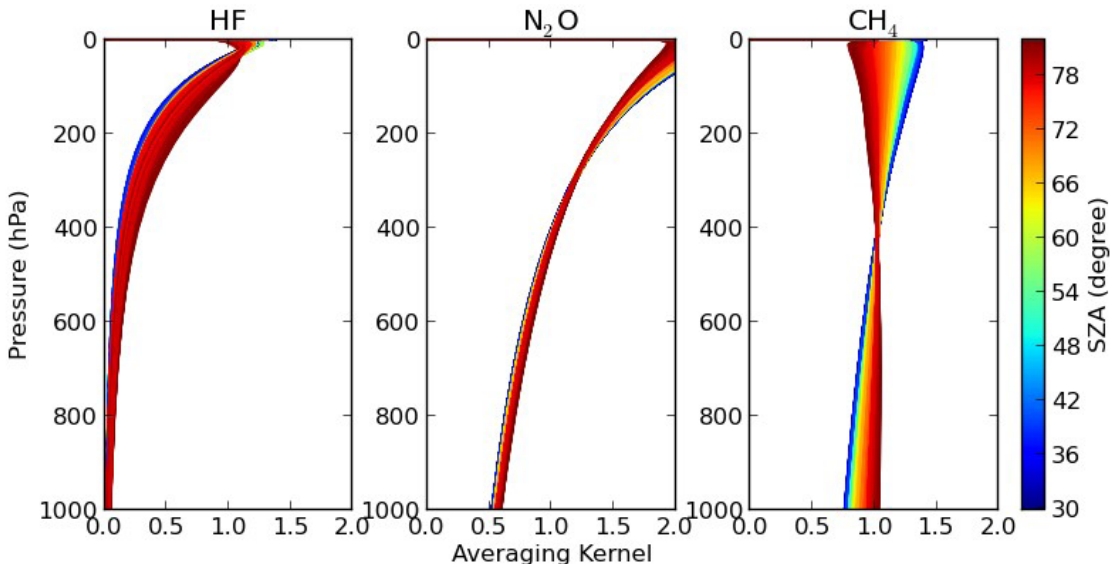


Figure 3.3. The averaging kernels of HF, N₂O and CH₄ at Bialystok for all spectra from 2010. the colors indicate the solar zenith angle (SZA) of the corresponding measurements.

To see how an averaging kernel influences retrieval, using Eq. 2.10 and ignoring last three error terms, replacing the state notation x by the mole fraction profile f , and omitting the hat notation, then we have,

$$f_r = f_a + A(f_t - f_a), \quad (3.7)$$

where, the f_r , f_t and f_a are retrieved, true and a prior mole fraction profiles, respectively. A is the averaging kernel. Integrating Eq. 3.7 and rearranging yield,

$$\int_0^{P_s} f_r \frac{dp}{mg} = \int_0^{P_s} (I - A) f_a \frac{dp}{mg} + \int_0^{P_s} A f_t \frac{dp}{mg}, \quad (3.8)$$

where m is the molecular mass of moist air ($m = (1 - X_{H_2O})m_{dry}^{air} + X_{H_2O}m_{H_2O}$), g is the gravitational acceleration, I is an identity matrix, and P_s is surface pressure. Since GFIT performs a profile scaling retrieval, Eq. 3.8 should be written in the form of the column averaging kernel,

$$\int_0^{P_s} f_r \frac{dp}{mg} = \int_0^{P_s} (1 - a(p)) f_a \frac{dp}{mg} + \int_0^{P_s} a(p) f_t \frac{dp}{mg}, \quad (3.9)$$

where, $a(p)$ is the column averaging kernel vector, which is a function of pressure (altitude). From the equation above, it can be seen that the retrieved total column includes contributions from a prior and true profiles, whose weights are determined by the column averaging kernel magnitude.

After taking the averaging kernel effect into account Eq. 3.6 is changed to following equations,

$$\begin{aligned} X_{CH_4}^{trop} &= \frac{VC_{CH_4}^r - \gamma_{CH_4} - b\mu_y(VC_y^r - \gamma_y - \varphi_y X_y^{trop} VC_{air})}{\varphi_{CH_4} VC_{air}} \\ \varphi &= \int_0^{P_s} a(p) \frac{dp}{mg} / \int_0^{P_s} \frac{dp}{mg} \\ \mu &= \int_0^{P_s} a_{CH_4}(p)(f_t - X^{trop}) \frac{dp}{mg} / \int_0^{P_s} a(p)(f_t - X^{trop}) \frac{dp}{mg} \\ \gamma &= \int_0^{P_s} (1 - a(p)) f_a \frac{dp}{mg} \end{aligned}, \quad (3.10)$$

where, y represents N₂O, HF or CH₄, and VC^r is the retrieved total column including a prior and averaging effect as described by Eq. 3.9, being distinguished from the true column VC . Considering the calculation of the coefficients φ and μ , the true mole fraction profiles of N₂O or HF are needed. Because of the long lifetime of N₂O and HF, and then small variabilities of their profiles, the GFIT a prior profiles should be a reasonable approximation. However, the GFIT a prior does not account for the influence of the polar vortex, within which air is subsided strongly and the profiles of atmospheric species deform as well. According to Toon et al. (1992) this deformation can approximately be described by one parameter, the degree of subsidence. Here the degree of subsidence is derived through compressing a reference N₂O profile to fit the FTS measured total column-averaged N₂O mole fraction. The reference profile has same shape as the N₂O a prior profile, but its tropospheric mole fraction has the same value as that predicted by the mentioned method (a sum of three terms). The subsidence is achieved through a relation $f_{N_2O}^{sub}(z) = f_{N_2O}^{ref}[z(1+dos)]$, dos is the degree of subsidence. The subsided profile is integrated, accounting for the a prior and averaging kernel according to Eq. 3.9, to give a predicted total column-averaged mole fraction of N₂O. The dos is changed until the prediction and measurement of

total column-averaged N₂O mole fractions agree well. To avoid influences of measurement noise the daily median of the total column-averaged N₂O mole fraction is used. The derived degree of subsidence is also applied to HF a prior profiles.

To compare the derived tropospheric xCH₄ with in situ measurements, measured CH₄ profiles need to be integrated. At the same time, the averaging kernel effect of the FTS measurements should be taken into account. For our purpose only the tropospheric part is important, and it is expected that the integration only extends up to tropopause for both in situ profiles and the averaging kernel. It can be proved that the integration takes the following format (see Appendix A),

$$X_{CH_4}^{trop} = \left(\int_{P_t}^{P_s} a_{CH_4} f_t \frac{dp}{mg} \right) / \left(\int_{P_t}^{P_s} a_{CH_4} \frac{dp}{mg} \right), \quad (3.11)$$

where P_t is tropopause pressure. f_t is the true CH₄ profile and replaced by the in situ profiles.

The total columns of CH₄, N₂O and HF are used in the derivation above, but the total columns directly retrieved from spectra include errors arising from spectroscopic imperfections and instrumental effects. The TCCON products are the dry air column averaged mole fractions, which are obtained through creating a ratio of the retrieved total columns of a species to a dry air column inferred from a retrieve O₂ column. This is because the ratio with the O₂ column can decrease instrumental effects. The dry air column averaged mole fractions have been corrected by air-mass independent and air-mass dependent calibration factors to account for spectroscopic inaccuracies. These corrections should be taken into account in calculating the tropospheric xCH₄ and the Eq. (3.10) is changed to,

$$X_{CH_4}^{trop} = \frac{1}{\varphi_{CH_4}} \left[X_{CH_4} - \frac{\gamma_{CH_4}}{VC_{air}} - b \mu_y \left(X_y - \frac{\gamma}{VC_{air}} - \varphi_y X_y^{trop} \right) \right], \quad (3.12)$$

where X_{CH_4} and X_y are the dry air column averaged mole fractions of CH₄ and y .

3.1.4. Comparison of between the N₂O and HF methods and in situ data

To test the method described in Sect. 3.1.3, data from four TCCON sites at Ny-Ålesund, Orléans, Bialystok and Darwin are used. Figures 3.4-3.7 show the results for these sites. We compare FTS-measured tropospheric xCH₄ to in situ data from NOAA at Ny-Ålesund, and the low aircraft data at Orléans and Bialystok. These low aircraft profiles have been extended into the whole troposphere as described in Sect. 3.1.2, and then integrated to produce a tropospheric xCH₄. For each site with available in situ data the results using N₂O are in better agreements with the in situ measurements than when using HF. The difference between the results using N₂O and HF has both seasonal and site dependence. At Ny-Ålesund the results using N₂O are about 30 ppb higher than those using HF, about 20 ppb at Bialystok and Orléans, and about 10 ppb lower at Darwin. Such a difference might result from the uncertainty in the HF column. The HF column used here is not calibrated through in situ profile measurements since HF is located completely in the stratosphere and there are no such

measurements currently available. The inaccuracy in the spectroscopy of HF will force the retrieved HF column away from the truth. Such an effect also depends on the HF total column. A stronger signal is more sensitive to a spectroscopy parameter error. This might partly explain the site dependence of the difference between the results using N₂O and HF since the tropopause pressure and HF column generally decrease from Arctic to tropics.

Another difference is that the results using HF present a larger scatter at Darwin than at the other three sites, while the results using N₂O have similar scatters at all four sites. This difference also arises from the HF column error. The TCCON HF column is retrieved from a weak spectral absorption line that is located at the shoulder of a water line. Therefore, the retrieval of HF suffers from water vapor interference. The interference depends on both the water amount and its vertical distribution, and could result in a large scatter. In the tropics the higher amount of water vapor in the atmosphere will significantly influence the retrieved HF column. Another factor is that the HF column amount decreases from high to low latitudes, since HF locates completely in the stratosphere and generally the tropopause height increases from high to low latitudes. The retrieval of HF has better precision and worse accuracy for larger HF columns due, respectively, to a stronger signal and larger effect from spectroscopy error, and vice versa. The performance of the HF method should be more stable but has a larger offset for high-latitude sites like Ny-Ålesund owing to the dry conditions and more significant signals, and be less stable and has a smaller offset for tropical sites like Darwin because of the moisture conditions and relatively weaker signals.

The main uncertainty in the N₂O approach comes from applying a simple model to predict latitudinal and temporal variations of tropospheric N₂O mole fractions and ignoring the vertical and longitudinal variations. This is a reasonable approximation because of its long lifetime in the atmosphere. However, in the presence of strong regional sources, like biomass burning and industrial sources, such an assumption might not be valid. A sensitivity test reveals that a 2 ppb perturbation in the assumed tropospheric N₂O mole fraction results in perturbations in the derived tropospheric xCH₄ of 4.0-4.4 ppb at Darwin, 4.2-5.6 ppb at Orléans and 4.5-5.5 ppb at Ny-Ålesund.

Figure 3.8 presents seasonal cycles of the tropospheric xCH₄ derived through averaging the time series given by Figs. 3.4-3.7. Generally the seasonal features of results from N₂O and HF are similar except an almost constant offset (with a variability of about 8 ppb) at each site. As previously mentioned, these might come from the error in the HF total column.

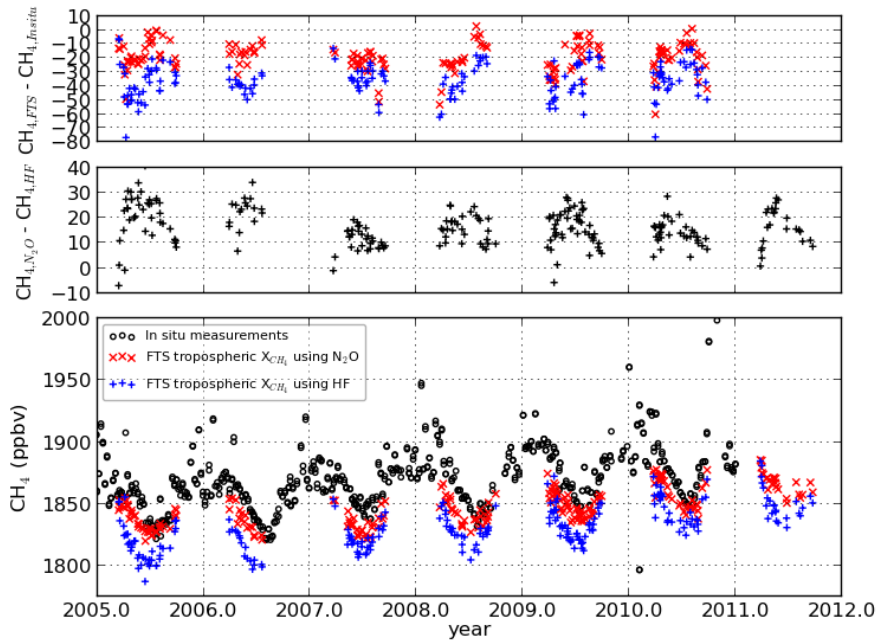


Figure 3.4. Results at Ny-Ålesund, the red points correspond to the tropospheric column-averaged CH_4 mole fraction derived from N_2O , the blue to those derived using HF and the open circles are in situ CH_4 data measured at Zeppelin mountain. The upper panel shows the difference between the in situ and tropospheric column-averaged CH_4 mole fractions, the middle panel is the difference between the results using N_2O and HF.

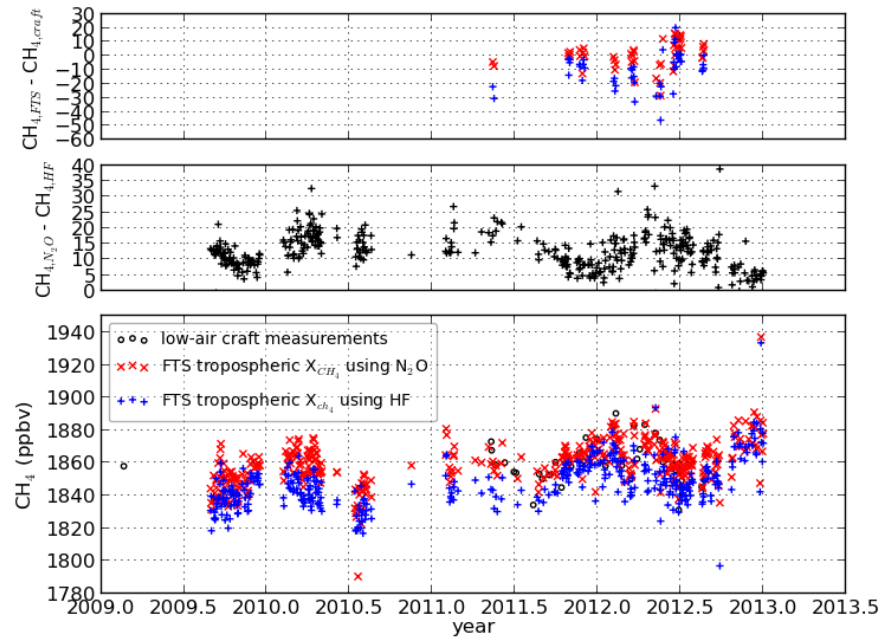


Figure 3.5. Same as Fig. 3.4 except for at the Orléans site and with the black circles lower panel

representing tropospheric column-averaged CH_4 mole fraction from low altitude aircraft profiles.

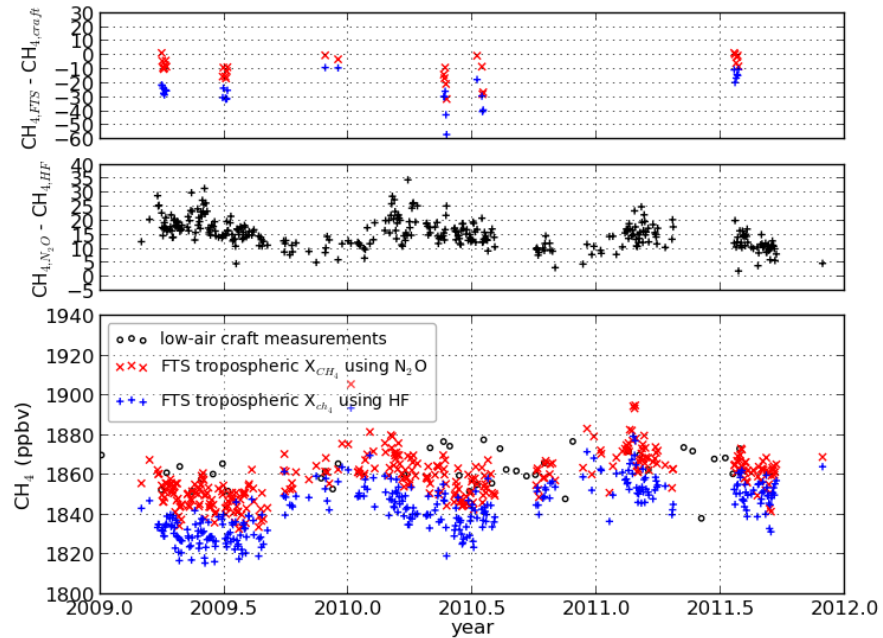


Figure 3.6. Same with Fig. 3.4 except at Bialystok.

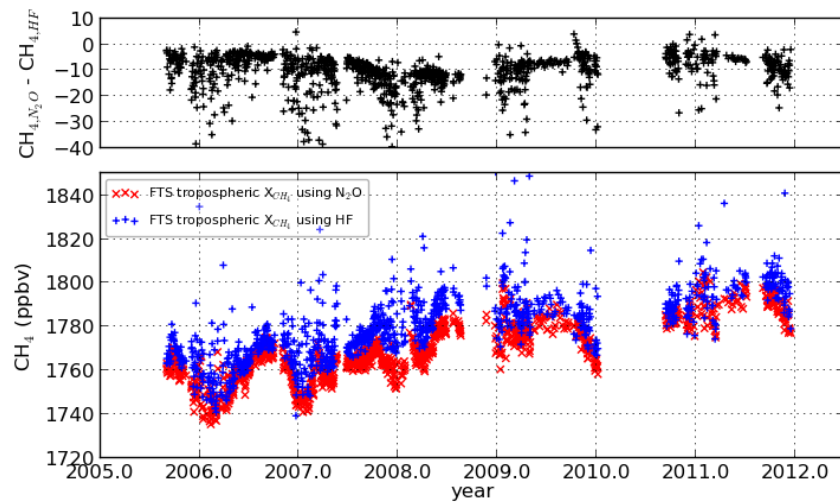


Figure 3.7. Results at Darwin.

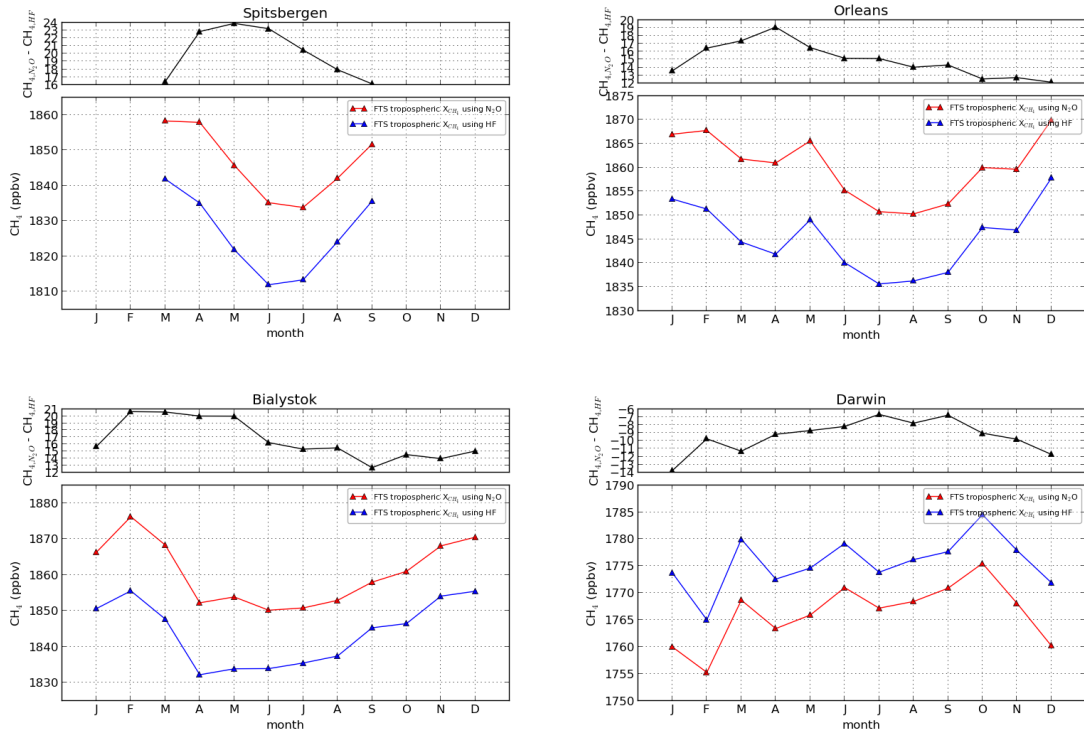


Figure 3.8. The multi-annual mean seasonal cycles of tropospheric column-averaged CH_4 mole fraction for four sites. The red points correspond to the results derived from N_2O and the blue to HF.

3.1.5. Comparison with aircraft profile measurements

The derived tropospheric $x\text{CH}_4$ are compared against in situ measurements from the HIPPO and IMECC aircraft campaigns and the inter-site consistency of the N_2O and HF methods is assessed. The comparison between the integrated in situ profiles and the HF- and N_2O -derived tropospheric $x\text{CH}_4$ s is shown in Fig. 3.9. The aircraft data at Bialystok and Orléans are from the IMECC campaign, and at Darwin from the HIPPO-4 campaign. According to the definition, the tropospheric $x\text{CH}_4$ is the mean abundance between the surface and the chemical tropopause. The aircraft profiles do not extend high enough to identify the chemical tropopause, so the thermal tropopause is used instead. The GFIT a priori profile is used for altitudes above the highest in situ measurement altitude. The a priori profile has been scaled to match the aircraft profile in the troposphere. The mole fraction at the lowest sample point is used to extrapolate to the surface to complete the profile below the lowest measured point during the aircraft flight.

The constructed profiles are then integrated using Eq. 3.11. Results from the FTS during the aircraft measurement period are averaged, and the uncertainty of the FTS data is estimated as the standard deviation of these results. The uncertainty of the tropospheric $x\text{CH}_4$ integrated from the extended aircraft measurement is calculated as the mean of the uncertainties at all sample points along the

altitude axis, weighted by the partial air column at each point. Comparing the GFIT a priori and the in situ measurements reveals that the standard deviation of the ratios of the a priori to the measurement is 1.8 %. Therefore, for the altitude range where the scaled GFIT a priori is used, an uncertainty of 1.8 % is assumed. This part represents the largest contribution to the total uncertainty. The uncertainties of the points below the aircraft ceiling are estimated from instrumental performances and the variation of CH₄ mole fractions along the aircraft path. In general the results using N₂O fall closer to the fitted line. The distances between the points and the fitted line are 3.5, 4.6, 2.1, 0.8, 0.2, 5.7 ppb for the results derived using the N₂O method, and 7.6, 9.0, 6.9, 0.4, 7.1, 17.2 ppb for the HF method.

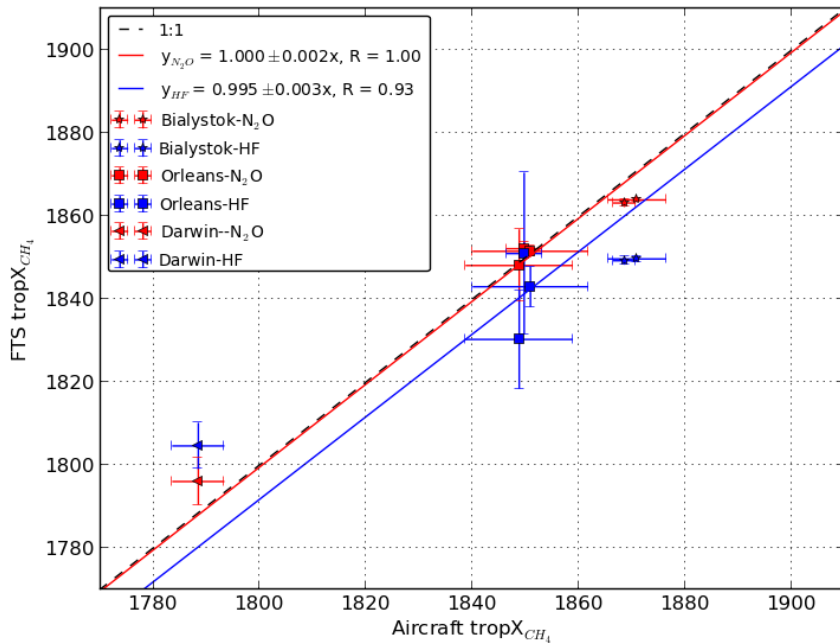


Figure 3.9. Comparison results of FTS tropospheric column-averaged CH₄ mole fraction with aircraft data. The aircraft profiles are smoothed using GFIT averaging kernels in troposphere using Eq. 3.11. The FTS data are averaged through aircraft measurements periods, and the error bars of FTS data are standard deviations of these averaged data.

3.1.6. Uncertainty analysis

The Gaussian error propagation equation is used to estimate the uncertainty in calculating the tropospheric xCH₄ using Eq. 3.12. The errors in the assumed tropospheric mole fraction of N₂O were not taken into account since significant departure only occur in the present of strong local N₂O sources. Also, the errors in the coefficients accounting for the averaging kernel effect are overlooked since they are unknown.

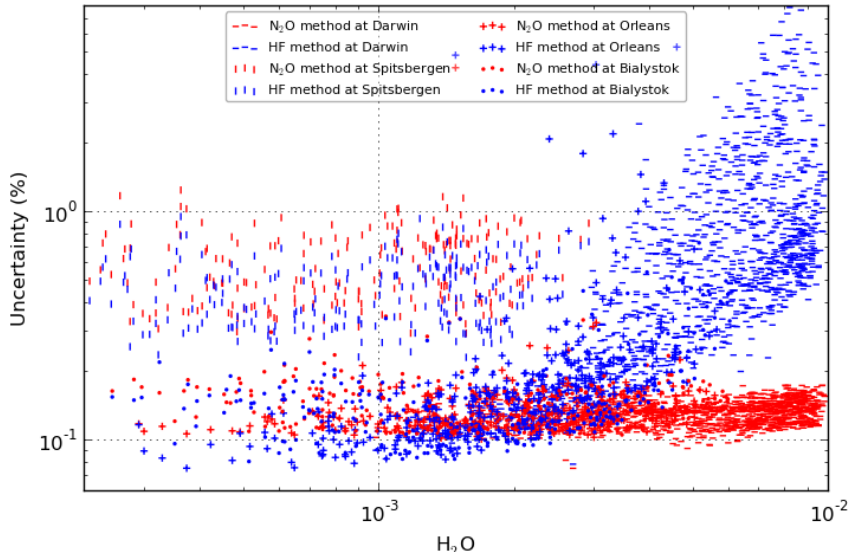


Figure 3.10. Relative error estimation of the tropospheric column-averaged CH_4 mole fraction using Gaussian error propagation equation for four sites, the blue corresponds to the error for the method using HF and the red to that of method using N_2O .

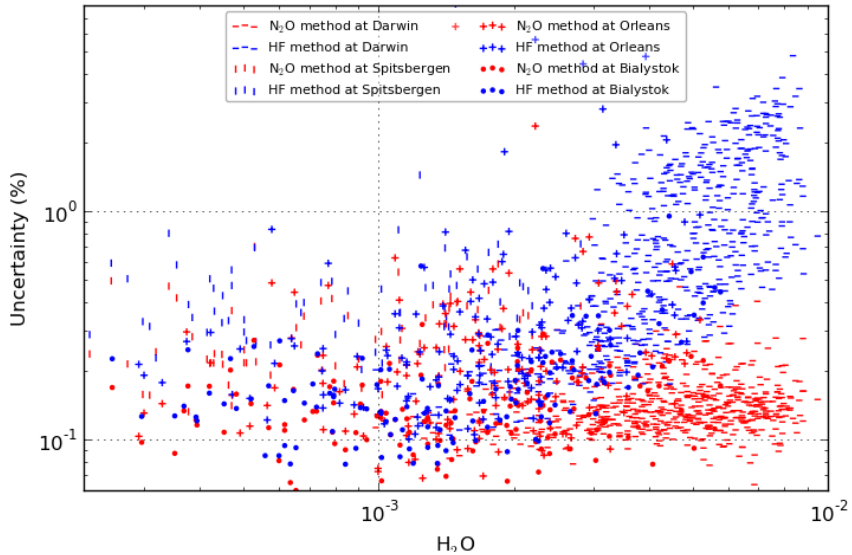


Figure 3.11. Same as Fig. 3.10 except for that the relative error is estimated as the standard deviation of tropospheric column-averaged CH_4 mole fractions during one day divided by the daily mean.

The errors of the slope parameters b are estimated as 0.011 (N_2O) and 1.9 (HF). The errors of the dry air column averaged mole fractions of CH_4 , N_2O and HF are taken as the values estimated in GFIT. Except for using the Gaussian error propagation equation, we calculate the standard deviation

of the derived tropospheric $x\text{CH}_4$ during a day as an alternative estimation of the uncertainty. To ensure the calculated standard deviation is significant only the days with fine weather conditions are considered. In practice, those days during which there are more than 50 spectra available at Ny-Ålesund and 100 spectra at other three sites are considered. Figure 3.10 presents the estimated relative uncertainties for all sites using the Gaussian error propagation equation method and Fig. 3.11 presents the results using the standard deviation method. The two methods produce similar results. The mean relative standard deviation of the tropospheric $x\text{CH}_4$ using N_2O is 0.15 % (Darwin), 0.30 % (Ny-Ålesund), 0.28 % (Orléans) and 0.14% (Bialystok). And they are 0.93 %, 0.45 %, 0.50 %, and 0.20 %, respectively, in the case of HF. It could be concluded that the method using HF produces larger uncertainties, especially at Darwin. In addition, The method using HF suffers from stronger H_2O interference, which results in higher uncertainties when H_2O columns are larger. The two methods are comparable in the case of low H_2O columns. While using the Gaussian error formulation the HF method results in marginally lower uncertainties under the low H_2O condition, the relative daily standard deviations are always smaller for the N_2O method.

3.2. Profile retrieval method

The algorithm of determining the tropospheric mole fraction of CH_4 through profile retrieval is developed in the Karlsruhe Institute of Technology (KIT, Germany) (Sepúlveda et al., 2012, 2014). The method is applied to NDACC high-resolution mid-infrared solar spectra, which include more profile information than TCCON near-infrared spectra. In this section, the algorithm is compared to the posterior correction method using N_2O as a proxy.

3.2.1. FTS measurements and surface in situ datasets

NDACC is a global ground-based FTS network monitoring atmospheric composition changes. The FTS records direct solar spectra in the mid-infrared spectral region ($740\text{-}4250 \text{ cm}^{-1}$), with a resolution of $0.0035\text{-}0.005 \text{ cm}^{-1}$. Measurements at two sites which are involved in both TCCON and NDACC, Ny-Ålesund (78.9°N , 11.9°E , 20 masl), Spitsbergen, and Bremen (53.1°N , 8.85°E , 27 masl), Germany, are used. The mid-infrared spectra are recorded using an Indium-Antimonide (InSb) detector cooled with liquid nitrogen and a CaF_2 beam splitter. The high-resolution FTS allows for a detailed observation of absorption line shape of atmospheric species. The line width of an atmospheric absorber includes natural broadening and collision (pressure) broadening. The natural broadening is proportional to frequency and the square root of temperature. So it decreases in the troposphere slowly with altitudes and increases in the stratosphere at a specific frequency. The collision broadening is proportional to pressure and the inverse of the square root of temperature. So the collision broadening decreases exponentially with height. Because of the dramatic variation of natural broadening, the vertical distribution of an atmospheric species can be inferred from its absorption line shape presented on the spectra recorded by a ground-based FTS. The information content for the vertical distribution depends on the resolution and signal-noise ratio of the spectra.

Two surface in situ datasets are used to empirically validate tropospheric CH_4 retrieved from FTS

spectra. At Ny-Ålesund the same dataset from NOAA as described in Sect. 3.1.2 is used. However, there is not in situ data available near the Bremen FTS site. A NOAA site Mace Head, Ireland (53.326°N, 9.899°W, 5 masl) locates at the west coast of Ireland. The Mace Head site is influenced by air masses from the North Atlantic ocean (about 70% according to trajectory analysis), and from North America and Northern Europe (about 30%). The weekly surface flask measurements are used as a reference for retrieval at the Bremen site although its large distance from Bremen.

3.2.2. Profile retrieval setup

The mid-infrared spectra are analysed with the code PFOFFIT (Hase et al., 2004). The atmosphere is discretized into 49 levels which extend from a FTS observation altitude to 120 km and the increments between them increase from 0.4 km at the lowest levels to 14 km at the highest levels. The profiles of atmospheric temperatures and pressure are from NCEP reanalysis data, with intra-day variabilities included. Applied spectral microwindows are: 2613.70-2615.40 cm^{-1} , 2650.60-2651.30 cm^{-1} , 2682.00-2684.20 cm^{-1} , 2919.64-2920.40 cm^{-1} , and 2922.73-2924.16 cm^{-1} . In these regions CH_4 has dominant absorption features, but there are discernible absorptions from other species as well. To simulate measured solar radiation in these regions absorptions of H_2O , HDO, CO_2 , O_3 , N_2O , CH_4 , NO_2 , HCl , OCS, CH_3OH are considered. The spectroscopic parameters of these gases are from HITRAN 01 for CH_4 , HITRAN 08 for the others (Rothman et al., 2009). The spectral line shape is assumed to be the Voigt function. Simulation effect for a spectrum measured at Bremen is shown in Fig. 3.12.

The state vector consists of CH_4 mole fractions at discretized levels, scale factors for a prior profiles of all interfering species except for O_3 , OCS and CH_3OH , and some other parameters. A prior profiles of CO_2 , N_2O , H_2O and HDO are taken as GFIT a priors (the GFIT a priors of H_2O and HDO are basically from NCEP reanalysis data). The climatologies of the Whole Atmosphere Community Climate Model (WACCM) are used as a prior profiles of other species. Because the spectra do not contain full information of CH_4 profiles, a first-order Tikhonov-Phillips constraint is applied to constrain variabilities of its profile shape. CH_4 retrieval is performed on a logarithmic scale. The degrees of freedom for signal (DOFS) is about 2.6 for Bremen spectra and 2.3 for Ny-Ålesund's. The a posterior correction (Sepúlveda et al., 2014) is applied to the retrieved CH_4 profiles to separate the stratospheric and tropospheric signals further. The corrected CH_4 profiles and corresponding averaging kernels at Ny-Ålesund are shown in Figure 3.13.

The tropospheric CH_4 mole fraction is derived from the retrieved profiles through averaging mole fractions at the lowest six levels (up to about 2 km). The averaging kernels of the tropospheric CH_4 are shown in red lines in Fig. 3.13. In contrast to the almost uniform weights in the troposphere of TCCON CH_4 retrieval, the tropospheric CH_4 from the profile retrieval has large weight in the lower troposphere with a peak at about 3 km.

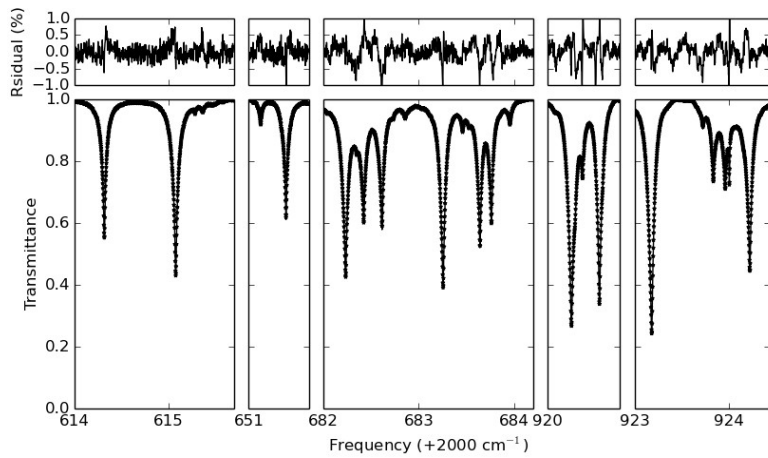


Figure 3.12 The five microwindows used for the retrieval of CH₄ profiles for an example spectrum at Bremen. Lower panel is the transmission with black points representing measurements and black line representing simulation. Upper panel are the differences between the measurement and simulation.

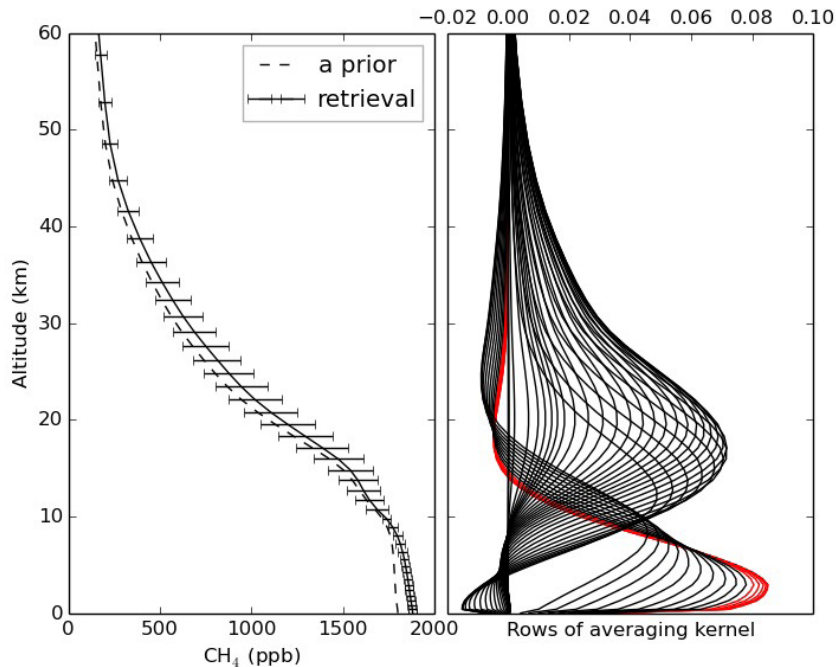


Figure 3.13 The averaged CH₄ profiles and its characteristics at Ny-Ålesund in the period 2007-2012. Left panel is the a prior (dashed line) and average of retrieval (solid line, error bar is the standard deviation). Right panel is the average of averaging kernel, with the red lines representing averaging kernels of CH₄ mole fractions at lowest six layers.

The second peak of the averaging kernels of the tropospheric CH₄ is at about 20 km, which could

bring variabilities of stratospheric CH₄ though the amplitude is much smaller than that of the peak in the troposphere. The tropospheric column-averaged CH₄ mole fraction from the profile retrieval is referred to lower tropospheric xCH₄ hereafter.

3.2.3. Comparison with a posterior correction method and in situ data

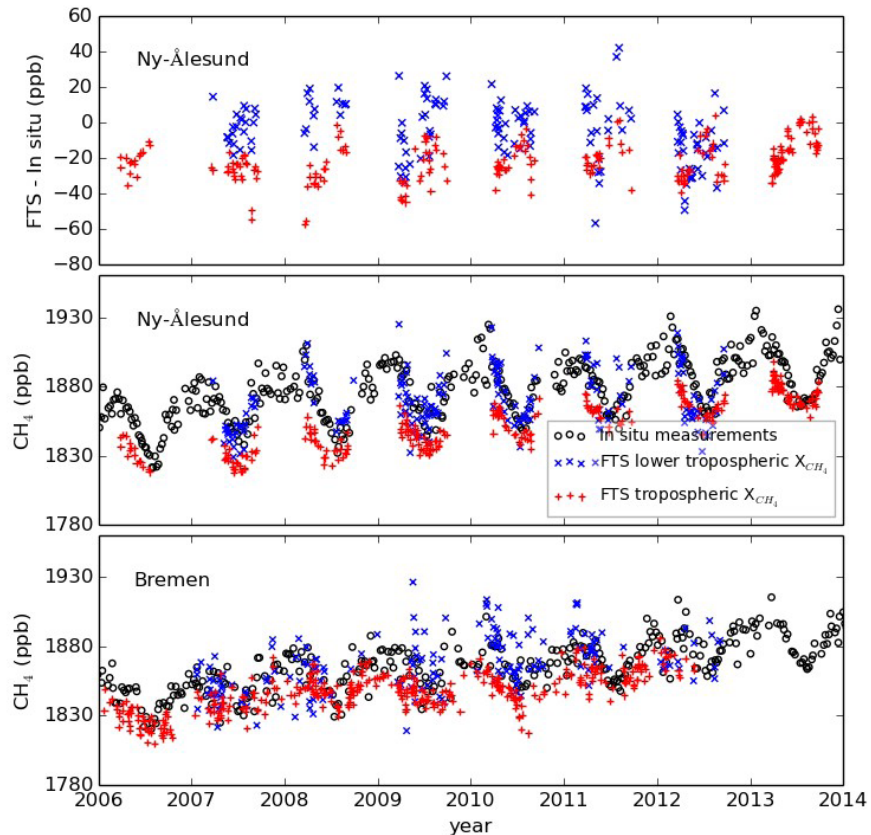


Figure 3.14 The tropospheric column-averaged CH₄ mole fraction from the posterior correction method using N₂O (red pluses) and lower tropospheric column-averaged CH₄ mole fraction (blue crosses) at Ny-Ålesund (mid panel) and Bremen (lower panel). Black circles represent in situ surface CH₄ measured at Zeppelin mountain (upper panel) and Mace Head (lower panel). Upper panel is the difference of FTS CH₄ to in situ CH₄ at Ny-Ålesund, difference is not performed at Bremen because of the large distance between the FTS and in situ sites. Daily medians are shown for all measurements.

In Fig. 3.14 the lower tropospheric xCH₄ is validated empirically with in situ surface measurements and compared with the tropospheric xCH₄ from the N₂O correction method. As expected the lower

tropospheric $x\text{CH}_4$ has a better agreement with the in situ measurements than the tropospheric $x\text{CH}_4$ at Ny-Ålesund in terms of the absolute value and seasonal cycle. The in situ measurements could represent lower tropospheric CH_4 concentrations because of quite clear air conditions there, and have a closer meaning with the lower tropospheric $x\text{CH}_4$. Both the tropospheric and, especially, lower tropospheric $x\text{CH}_4$ present larger scatters than in situ measurements at Bremen. The reason could be the FTS observation at Bremen is conducted in the City of Bremen, while the in situ samples mostly represent marine boundary air. But the large scatter in the lower tropospheric $x\text{CH}_4$, like in 2009 and 2010, could also come from some instability of the instrument, such as alignment variabilities and mechanical perturbations. The CH_4 retrieval by GFIT is performed with three large spectral windows ($116, 11$ and 138 cm^{-1} wide, respectively), and the O_2 column retrieved from the same spectra is used to infer the dry air column. Then the tropospheric $x\text{CH}_4$ should be much less sensitive to instrumental perturbations than the lower tropospheric $x\text{CH}_4$. Due to a higher requirement of profile retrieval for the accuracy of molecular spectroscopy, only a set of microwindows is used where spectral residuals between simulations and measurements are small. Line-mixing has been shown to be important but is not included in simulating molecular absorption here (Tran et al., 2006), which adds an asymmetrical component to the Voigt function.

3.3. Summary

In this chapter, we propose using N_2O to correct for the stratospheric contribution to the total column of CH_4 in order to derive a tropospheric $x\text{CH}_4$ mole fraction. This method is applied to data from four TCCON sites. At Ny-Ålesund and Orléans, the tropospheric CH_4 derived using N_2O and HF are compared with surface flask measurements and low aircraft profiles, respectively. At both sites, the results using N_2O agree better with in situ measurements than the HF derived results. The mean relative standard deviations are 0.23% and 0.52% for the methods using N_2O and HF, respectively. Especially, at Darwin the HF method produces a much larger uncertainty (0.93% compared with 0.15% of N_2O method) due to interference from H_2O , which is absent for the N_2O method. Under drier conditions, the relative uncertainties of the two methods are comparable, however the N_2O method shows a clear advantage in more humid situations. The methods have also been compared with aircraft profiles at three sites, and the results reveal that the N_2O method has a better inter-site consistency. However, it needs to be verified across a wider range of sites. The sensitivity of the N_2O method to the assumed tropospheric N_2O mole fraction is about $4\text{-}6 \text{ ppb per } 2 \text{ ppb}$.

The directly profile retrieval for tropospheric CH_4 is examined and compared to the proposed a posterior correction method using spectra measured at Ny-Ålesund and Bremen. The profile retrieval method has a large weight in the lower troposphere in contrast to an almost uniform weight of the proposed method in the whole troposphere, and then could reflect the sources and sinks of CH_4 more directly. There is a larger scatter in the results from the profile retrieval, which could arouse from a larger sensitivity of the profile retrieval to measurements error and usage of the retrieved O_2 column as the dry air column in the proposed method.

4. Validation of European CH₄ models using ground-based and satellite measurements

It is always important to validate model simulations with independent measurements. Given sources and sinks of GHG (greenhouse gas) and meteorological fields a chemical transport model predicts mole fractions of GHGs in the atmosphere. Inverse modeling goes in the opposite direction, retrieving the sources and sinks of the GHG from measured mole fractions. The theory of the inverse modeling can be described by Eq. 2.3 and 2.4 as well, which search for a solution minimizing the function given by Eq. 2.4. The forward function is replaced by the chemical transport model, and the measurements usually are mole fractions at surface provided by global networks and total columns from space-based remote sensing. A prior knowledge is usually provided by process-based models of sources and sinks. Because direct measurements of the sources and sinks are rare, the evaluation of simulated mole fractions with independent measurement is an important step to assess the quality of the retrieved sources or sinks. In this chapter, CH₄ mole fractions predicted by three inverse modeling systems, TM3, TM5-4DVAR and LMDz-PYVAR, are compared with ground and space-based remote sensing and in situ measurements.

4.1. Description of measurements

The tropospheric xCH₄ is derived with the posterior correction using N₂O as described in Chapter 3. But approximate averaging kernels, which are from interpolations in SZA to a set of reference averaging kernel, are applied. With the tropospheric CH₄ known, the stratospheric column-averaged CH₄ mole fraction is easily calculated given tropopause pressure, which is from NCEP reanalysis here.

The tropospheric xCH₄ derived using the approximate averaging kernel is validated against in situ measurements. The validation method is the same as in Sect. 3.1.5 except for using the approximate averaging kernels. The same aircraft campaigns HIPPO and IMECC, which has been described in Sect. 3.1.2, together with Aircore measurements are used. Figure 4.1 presents the calibration results, the mean distance between scatter points and the fitted line is 3.0 ppb, with a standard deviation of 2.0 ppb.

The TCCON sites referred in this study are listed in Table 4.1.

The CH₄ profiles retrieved from mid-infrared spectra measured at NDACC sites Bremen and Ny-Ålesund in Sect. 3.2 are compared to model simulations. The derived lower tropospheric xCH₄ and partial stratospheric column are compared with model outputs as well.

TCCON site	Latitude/°N	Longitude/°E	Altitude/masl
Ny-Ålesund	78.9	11.9	20
Sodankylä	67.3668	26.6310	188
Bialystok	53.23	23.025	183
Bremen	53.10	8.85	27
Orléans	47.97	2.113	130
Garmisch	47.476	11.063	740
Park Falls	45.945	-90.273	440
Lamont	36.604	-97.486	320
Izaña	28.3	-16.483	2370
Darwin	-12.424	130.891	30
Reunion Island	-20.901	55.485	87
Wollongong	-34.406	150.879	30
Lauder	-45.038	169.684	370

Table 4.1. Overview of TCCON sites used for evaluation of models.

The used surface CH₄ measurements are from NOAA/ESRL network and a Tall Tower station (Trainou tower, TRN) (Schmidt et al., 2014). For the tower measurements, the air sample at 180 magl is selected.

The CH₄ profiles from HIPPO-1 to 5 missions (Wofsy et al., 2011) are used to validate simulated CH₄ concentrations. The measurements use a quantum cascade laser spectrometer (QCLS). Calibrations derived through comparisons with NOAA Programmable Flask Package (Bergamaschi, et al., 2013; Alexe et al., 2015) are applied, which are 3.5, 3.9, 6.0, 4.5 and 5.2 ppb for the five HIPPO missions, respectively.

GOSAT measurements are the total column-averaged dry-air CH₄ mole fraction retrieved by the (UoL-OCPv5.1) algorithm (Parker et al., 2011). For the retrieval, the CO₂ proxy method (Frankenberg et al., 2011) is applied which infers air columns from the CO₂ column retrieved from the same spectra used for CH₄ retrieval. CH₄ and CO₂ are retrieved from channels at 1.65 μm and 1.61 μm respectively. Only spectra measured with clear sky condition are taken into account.

ACE-FTS (Atmospheric Chemistry Experiment) is the main instrument on board the Canadian Space Agency SCISAT-1 satellite. It is a high spectral resolution (0.02 cm^{-1}) FTS that measures in a solar occultation mode, tracking the sun during sunrise and sunset from a 74° , 650 km near circular orbit. This allows it to measure vertical profiles of CH_4 within the ~ 6 to 75 km range covering all latitudes between approximately 85°N and 85°S (Bernath et al., 2005). The data used in this study corresponds with version 3.5.

MIPAS (Michelson Interferometer for Passive Atmospheric Sounding) is a Fourier transform infrared (FTIR) spectrometer aboard ENVISAT (Fischer et al., 2008) for the detection of limb emission spectra in the middle and upper atmosphere. It acquires spectra over the range $685\text{-}2410 \text{ cm}^{-1}$. The primary geophysical parameters of interest are vertical profiles of atmospheric pressure, temperatures, and volume mixing ratios of about 25 trace constituents. The product used here is operational V6 data processed by ESA.

4.2. Description of models

A chemistry transport model describes the evolution of atmospheric compositions by solving the continuity equation, which is a mathematical representation of the principle of conservation of mass. In the case where the effect of molecular diffusion can be neglected, the continuity equation can be expressed as,

$$\frac{\partial x_i}{\partial t} = -\vec{v} \nabla x_i + P(\vec{x}) + L(\vec{x}), \quad (4.1)$$

where x_i is the mole fraction of the interested composition, \vec{v} is wind vector, P and L are production and loss rates of the composition, which are functions of all species that react with the interested one in the atmosphere, collected in the vector \vec{x} . The wind field is prescribed from other sources before integrating Eq. 4.1, such as reanalysis meteorological data. In practice the continuity equation must be discretized onto model grids. There are always atmospheric motions occurring at a scale smaller than the model grid scale because the atmosphere is a continuum. The transport of atmospheric composition by sub-scale motions is usually parameterized thorough relating to variables at the model grid. One is the eddy diffusion parameterization that treats the composition transport induced by turbulent motion of air in a way of treating molecular diffusion. Wet convective motion is another small-scale motion, and usually related to large-scale convergences and vertical instabilities. The production and loss term involves solving chemical kinetic equations, which usually account for more species than the interested species. Except for chemical reactions, the exchange between the earth surface and the atmosphere also produces or removes species. The dry deposition is the uptake of atmospheric species at the surface of the earth, and the surface can emit species as well. The uptake and emission fluxes provide a surface boundary condition for the continuity equation. Precipitation in the atmosphere scavenges soluble gases, which acts as a loss term. The chemical transport model differs in meteorological data used, discretization methods, parameterizations of small-scale motions, descriptions of production and loss processes, and

integration methods.

Model	Institute	Resolution (lat×lon)	No. of model levels	output Time step (hour)	Meteorology
TM3	Max Plank Institute for Biogeochemistry	4×5	26	3.0	ERA-Interim
TM5-4DVAR	European Joint Research Centre	1×1 for Europe, 6×4 for the rest of world	25	1.5	ECMWF-IFS
LMDz- PYVAR	Laboratoire des Sciences du Climatet de l'Environnement	2.5×3.75	19	3.0	Prediction by LMDz

Table 4.2. The models used in the comparison with solar absorption measurements.

The details of the models are listed in Table 4.2. The important chemical reactions involving CH₄ in the atmospheric is oxidations by OH in the troposphere, and by OH, Cl and O(¹D) in the stratosphere. The concentrations of these radicals are prescribed based on other model outputs, for example, tropospheric OH fields based on Carbon Bond Mechanism 4 chemistry and stratospheric radicals based on a photochemical model are applied in TM5-4DAVR inversion (Bergamaschi et al., 2009). The outputs of TM3 are from an inversion spanning from 2005 to 2012, and those of LMDz-PYVAR are from an inversion covering 2007 to 2011. TM5-4DVAR outputs are from a 6 year inversions series 2007-2012, consisting of 6 individual 14-month inversions, each of them includes 1 month spin-up and 1 month spin-down. Only in situ measurements at surface are used in the inversion run of the models, involved sites are presented in Figure 4.2. Detailed information on the inversion methodology was discussed in Bergamaschi et al. (2015).

The details about the global atmospheric tracer model TM3 can be found in Heimann and Köerner (2003) and inversion method is described in Rödenbeck (2005). TM5-4DVAR is a four-dimensional variational data assimilation system for inverse modeling of atmospheric methane emissions (Meirink et al., 2008). The system is based on the TM5 atmospheric transport model (Krol et al., 2005). LMDz-PYVAR is a framework that combines the inversion system PYVAR (Chevallier et al., 2005) with the transport model LMDz (Hourdin et al., 2006).

For evaluations of the model, model simulations are matched to measurement through interpolations in time, latitudes, longitudes and pressure. For the total and tropospheric column-averaged CH₄ the model profile is integrated taking a priori and averaging kernel into account

according to Rodgers and Connor (2003), and actually Eq. 3.9 and 3.11 are applied.

4.3. Comparison between FTS and surface measurements

The difference between the tropospheric $x\text{CH}_4$ and surface CH_4 mole fractions qualitatively reflects a vertical gradient of CH_4 in the troposphere. However, surface measurements are influenced by the turbulence and local emissions in the boundary layer while the tropospheric $x\text{CH}_4$ mainly reflects CH_4 in the free troposphere. To reduce this difference long-term trends are extracted from their time series. The TCCON and corresponding in situ sites are selected to locate closely so that the two kinds of instrument measure similar airmass. The sites used are listed in Table 4.3.

FTS site				In situ site			
Name	Lat/ $^{\circ}$ N	Lon/ $^{\circ}$ E	Alt/masl	Name	Lat/ $^{\circ}$ N	Lon/ $^{\circ}$ E	Alt/masl
Ny-Ålesund	78.923	11.923	24	zep/NOAA	78.907	11.889	479
Sodankylä	67.367	26.631	188	pal/NOAA	67.970	24.120	565
Orléans	47.965	2.113	132	Trainou tower	47.965	2.113	311
Park Falls	45.945	-90.273	440	lef/NOAA	45.930	-90.270	868
Lamont	36.604	-97.486	320	sgp/NOAA	36.620	-97.480	374
Izaña	28.300	-16.483	2370	izo/NOAA	28.300	-16.480	2378
Lauder	45.038	169.684	370	bhd/NOAA	-41.408	174.871	90

Table 4.3. The sites used for comparison of FTS tropospheric column-averaged CH_4 mole fraction and in situ surface/tower CH_4 mole fraction.

A curve fitting procedure similar to that described in Dlugokencky et al. (1994) is applied to extract a long-term variation in which variabilities with temporal scale shorter than 1.4 years is filtered out. Firstly, a daily median series is constructed from original data. Then a curve that is a quadratic polynomial and a series of four harmonics is fitted to the daily median series. The Kolmogorov-Zurbenko (KZ) filter (Eskeidge et al., 1997) is applied to the residual between data and the fitted curve to extract variations with periods greater than 1.4 years. Then the long-term variation is obtained via adding the quadratic function and extracted variation. The procedure is used iteratively and values outside 2.8 standard deviations are removed at each step until no outliers are recognized.

Figure 4.3 shows a comparison between the long-term variations and increases of measured tropospheric $x\text{CH}_4$ and in situ surface CH_4 . The difference between the tropospheric $x\text{CH}_4$ and in situ surface CH_4 reflects a mean vertical gradient of tropospheric CH_4 , which is influenced by

surface emissions, transports and OH fields. Generally there are negative vertical gradients in the northern hemisphere and positive vertical gradients in the southern hemisphere (except for above southern continents with strong emissions). Here we refer to decreasing CH₄ mole fractions with altitudes as a negative vertical gradient, while increasing CH₄ with altitudes is a positive vertical gradient. This occurs because most CH₄ is emitted at northern surfaces and mixed into southern air and transported by the southward branch of the southern hemispheric Hadley cell, which prevails in the mid and upper troposphere. In the troposphere, surface emissions cause decreasing CH₄ with altitudes, while OH oxidations cause a positive vertical gradient.

In the absence of horizontal transports and OH oxidations, the growth rate of the tropospheric xCH₄ would be smaller than, and follows the variations of the surface CH₄. As shown in Fig. 4.3, there are significant positive anomalies in the surface CH₄ growth rate during 2007 for all sites. This is consistent with other studies (Dlugokencky et al., 2009) and was attributed to wetland emissions. As a result, the CH₄ vertical gradient becomes more negative at all sites. However, as can be seen from Fig. 4.3, there are many cases where tropospheric xCH₄ presents a larger growth rate, or its growth rate rises faster than that of the surface CH₄ and sometimes even rises when the growth rate of the surface CH₄ drops. The CH₄ vertical gradient at Ny-Ålesund has significantly changed toward positive since 2008 (increases about 15 pbb) compared to other sites except for Park Falls. These results could reveal that there is CH₄ from lower latitudes transported into the mid to upper troposphere over this site during that time.

At Park Falls, the CH₄ vertical gradient also significantly changes toward positive since 2008 but with more fluctuations than Ny-Ålesund. However, both the tropospheric xCH₄ and surface CH₄ mole fractions increase in this period, which means there are strengthening surface emissions and would have change the gradient toward negative. The positive change of the gradient could be caused by OH, because strengthening of a loss via reactions with OH will depress increase trends in tropospheric CH₄ due to increases in surface emissions, but to a larger extent for surface CH₄. Such an explanation could apply to cases when surface CH₄ has smaller growth rates than the tropospheric xCH₄ at sites over which without horizontal transports induced additions of CH₄. At sites in the southern hemisphere, the annual variability in North-South transports will play an important role, which changes CH₄ in the mid and upper troposphere more directly. The surface CH₄ is influenced by southern emissions as well, e.g. natural wetlands and agriculture in South America and southern part of Africa. The change in the vertical gradient of tropospheric CH₄ could be a result of combined effects of transport, surface emissions and OH.

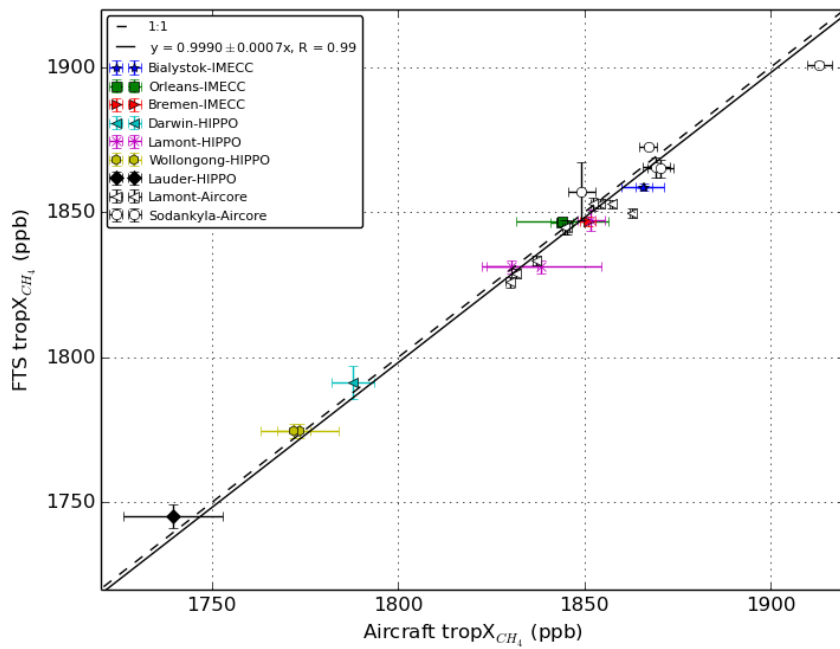


Figure 4.1. Validation results of FTS derived tropospheric column-averaged CH_4 mole fractions with in situ measurements. The in situ profiles are smoothed using GFIT CH_4 averaging kernels in troposphere as described in Sect. 3.1.5. The FTS data are averaged through the aircraft measurements periods.

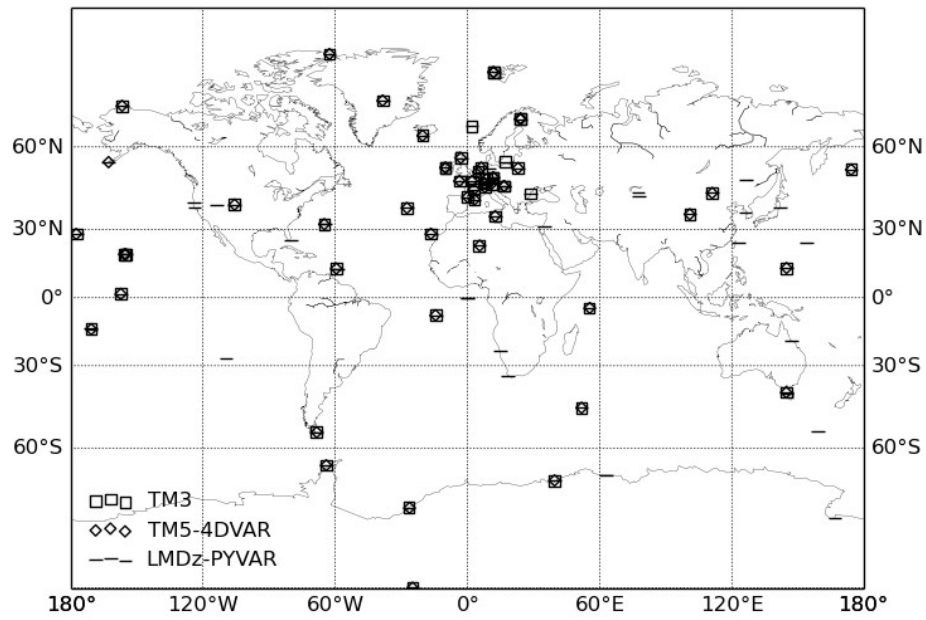


Figure 4.2. Global distribution of surface sampling/in situ sites at which measurements are assimilated into TM3 (square), TM5-4DVAR (diamond) and LMDz-PYVAR (horizontal line) in their inversion run.

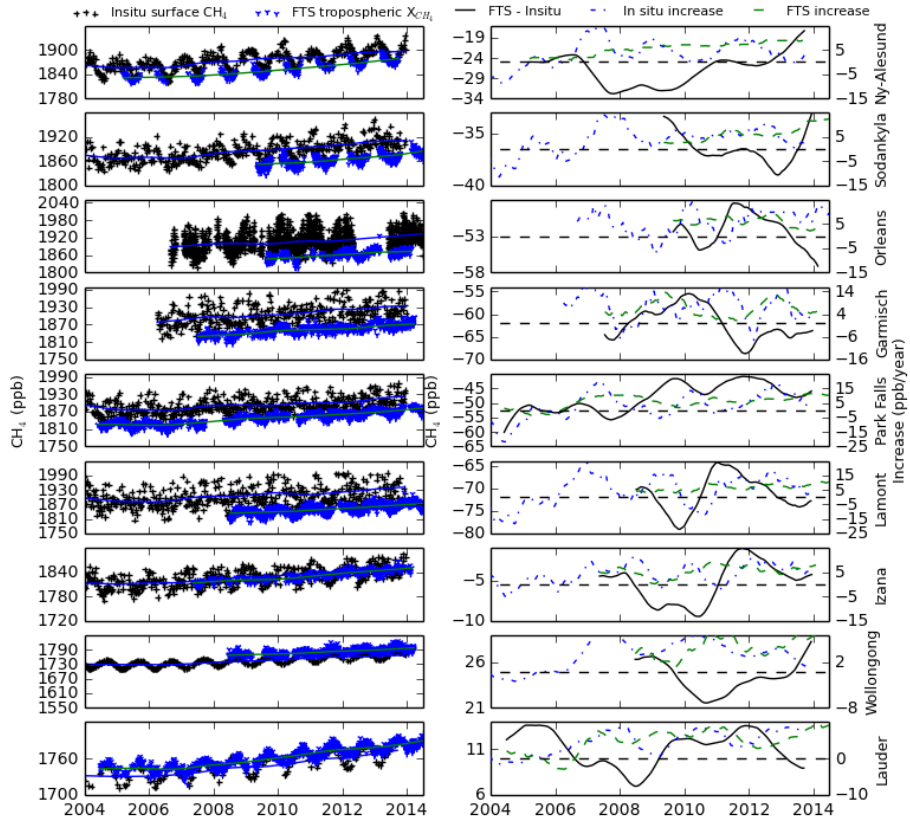


Figure 4.3. Comparison between FTS derived tropospheric column-averaged CH₄ and in situ surface/tower CH₄. In the left panel, the black and blue crosses represent the daily median of in situ CH₄ and tropospheric column-averaged CH₄, respectively. The curves are fitted long-term variations with time scale longer than 1.4 years. The lines in the right panel represent the difference between the long-term variations of tropospheric and in situ CH₄ (black), and the long term increase rate of tropospheric (green) and in situ (blue) CH₄.

4.4. Comparison between measurements and models

4.4.1. FTS, GOSAT and HIPPO

Temporal variabilities of the difference between models and FTS of the tropospheric and total xCH₄ is given at selected sites in Fig. 4.4. The measured tropospheric xCH₄ rises faster than the modeled since 2009 at Ny-Ålesund and Sodankylä. The differences (model – FTS) change from about 20 ppb to 10 ppb for TM3 and TM5-4DVAR, 10 ppb to 0 ppb for LMDz-PYVAR during 2009-2011.

The measured vertical gradient of tropospheric CH₄ changes toward positive since 2009 at Ny-Ålesund as shown in Fig. 4.3. But the models did not capture such a variation in the vertical

gradient. Differences between the long-term variations of tropospheric $x\text{CH}_4$ and surface CH_4 change about 5 ppb during the period 2007-2012 for all three models (see Fig. 4.5), much smaller than the measured 15 ppb during 2009-2013. It is shown in this section that all models underestimate the absolute value of the vertical gradient of tropospheric CH_4 at almost all TCCON sites. As said before, the measured change of 15 ppb could be caused by a CH_4 addition in mid and upper troposphere caused by transports from lower latitudes. Since the difference in CH_4 concentrations between in mid or upper troposphere and at surface is smaller in the models than in reality, the strengthening effect of input CH_4 is then depressed. This could explain the smaller increase of tropospheric $x\text{CH}_4$ in the models.

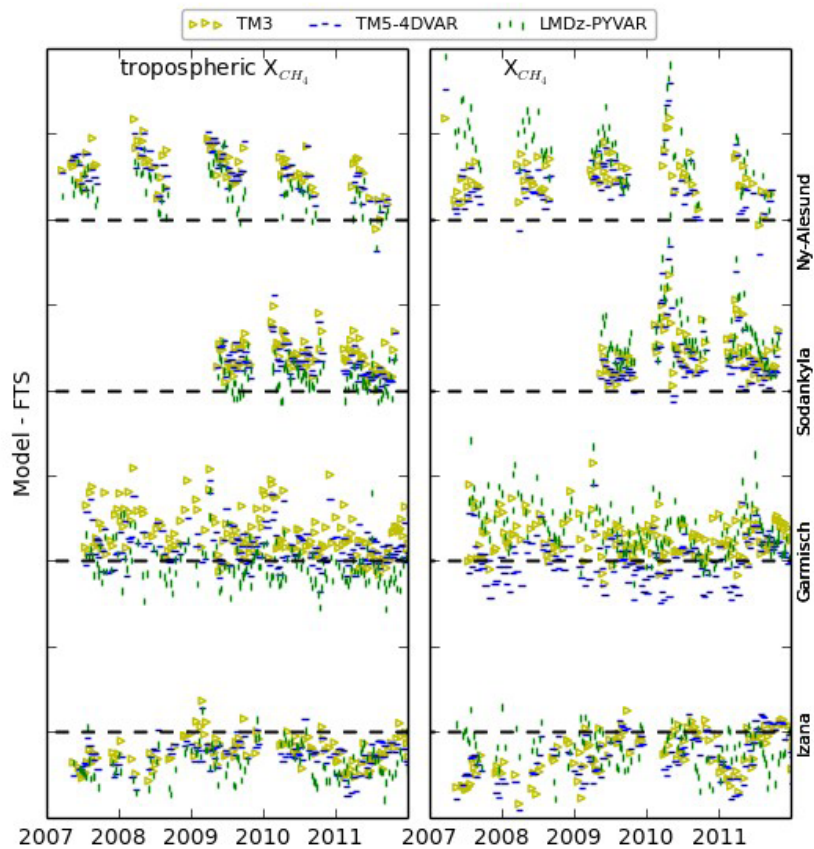


Figure 4.4. Differences of total (right) and tropospheric (left) column-averaged CH_4 concentration between FTS measurements and model simulations at European sites. The differences are shift for clarity and black dash line indicate zero position for each site. The increment of Y-axis is 30 ppb. The green, blue and yellow points represent difference between FTS measurement and TM3, TM5-4DVAR and LMDz-PYVAR simulations. Each point is the average over 7 days.

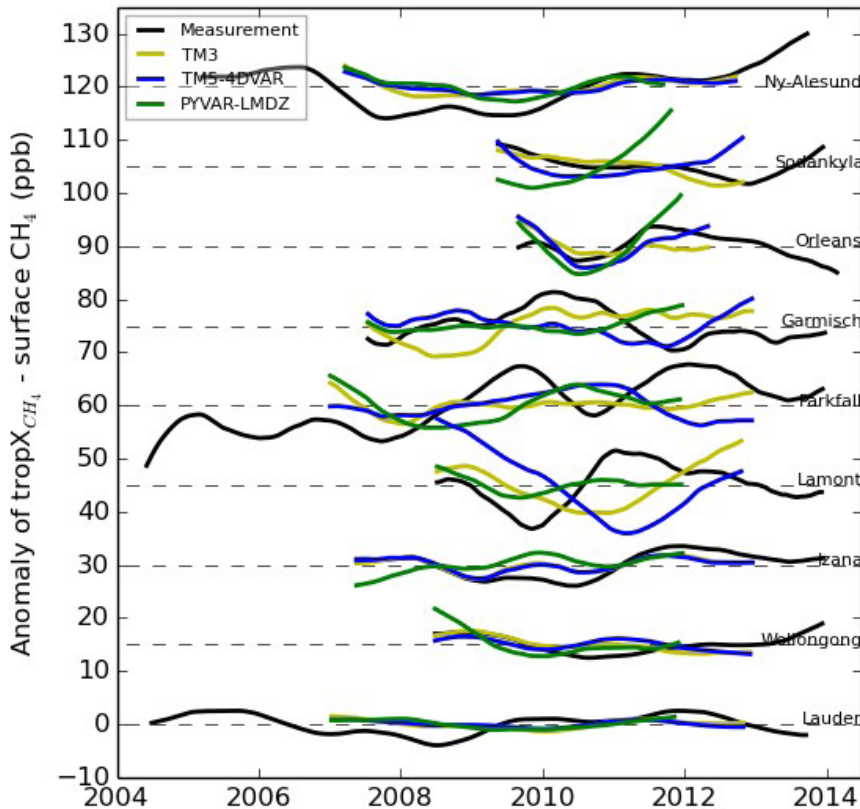


Figure 4.5. Anomalies of measured (black) and simulated (yellow: TM3; blue: TM5-4DVAR; green: LMDz-PYVAR) vertical gradient of CH_4 in the troposphere with respect to their averages. The anomalies have been shifted for clarity and dashed line indicate zero level for each site.

The CH_4 column meridional distribution is sensitive to the latitudinal distribution of CH_4 sources and sinks, tropopause altitudes, inter-hemisphere transport in the troposphere, and the residual circulation in the stratosphere. Assessing latitudinal variabilities of biases of a model could reveal how well these processes are represented in the model. Another important concern is to show whether model biases in the troposphere or the stratosphere contribute more to the total bias. The model to FTS comparison is for the period 2007-2011 when FTS measurements are available and the comparison to GOSAT is for the period 2009-2011.

The latitudinal behavior of the model biases in total, tropospheric and stratospheric xCH_4 are revealed by comparisons to FTS and GOSAT measurements as presented in Figure 4.6 and 4.7. CH_4 is emitted mainly in the northern hemisphere, destroyed mainly in the tropics by OH and has a slow inter-hemisphere transport on a temporal scale of 1 year. These factors altogether result in the final latitude distribution of CH_4 shown in Fig. 4.6, 4.7. The model biases present a latitudinal dependence in both the troposphere and stratosphere, and the latitudinal behavior is consistent

between FTS and GOSAT. Similar results were shown by other studies (Alexe et al., 2015; Ostler et al., 2016), which compared models against TCCON total xCH₄. In the troposphere, the model bias in the troposphere present a North-South gradient with positives at northern high-altitudes northward of 50°S. Figure 4.8 shows latitudinal variations of the measured and simulated vertical gradients of tropospheric CH₄. There are mostly positive biases in mid and high northern latitudes, negative ones in other latitudes. So the overestimated tropospheric CH₄ in mid to high northern latitudes could not originate from too strong emissions, which should result in a more negative vertical gradient there. The models underestimate absolute values of the vertical gradient of tropospheric CH₄. A too strong convection mixing can lead to a vertically uniform distribution of CH₄ in the troposphere. However, it could not be a reason to the incorrect vertical gradients here. The underestimation at high latitudes has similar amplitudes with that at lower latitudes, but convection mixing should be much weaker in high latitudes.

With FTS derived tropospheric and stratospheric xCH₄ (Wang et al., 2014) it is possible to examine how the tropospheric and stratospheric columns contribute to the model bias in total xCH₄. Figure 4.9 shows yearly and seasonal median model biases scaled by air column fractions of the troposphere and stratosphere. It is clear that model biases in the troposphere exhibit a North-South gradient with positive values in northern high-latitude during all seasons for all models. In the stratosphere model biases do not present any clear latitudinal pattern that exists through the whole year, and show significant seasonal variabilities for TM3 and TM5-4DVAR. That is consistent with the fact that stratospheric CH₄ distributions cycle between summer and winter hemispheric states. The stratospheric bias of LMDz-PYVAR shows a 'U' shape with the minimum located in the tropics. Comparing to Fig. 4.6 one can see that the latitudinal pattern of model biases in total xCH₄ results from both the stratosphere and troposphere for LMDz-PYVAR, but arises from the troposphere for the other two models. Because model biases change signs yearly and seasonally it is more appropriate to use the amplitudes (absolute model to FTS differences) to evaluate contributions of the troposphere and stratosphere, as shown in Fig. 4.10. The medians of model bias amplitudes over all FTS sites and years are 7.4±5.1 ppb in the troposphere and 4.3±9.9 ppb in the stratosphere for TM3, 6.72±4.8 ppb and 4.7±9.9 ppb for TM5-4DVAR, and 7.1±5.6 ppb and 10.3±15.9 ppb for LMDz-PYVAR. So the stratosphere dominates in model biases of LMDz-PYVAR but contributes less or comparably with the troposphere for the two other models.

Evaluations of the models at the surface with in-situ measurements, which are assimilated into the models, show smaller biases than the tropospheric xCH₄. The amplitudes are mostly below 10 ppb in the northern hemisphere except for a few outliers and below 5 ppb in the southern hemisphere (not show). The model biases at the surface do not show any significant latitudinal dependence. It is not clear how the model biases at the surface look like in the regions where no measurements are assimilated. However, it could be true that the overestimation of the tropospheric CH₄ meridional gradient is due to model biases in the mid and upper troposphere. That means, vertical distributions of CH₄ in the troposphere are not represented correctly in the models.

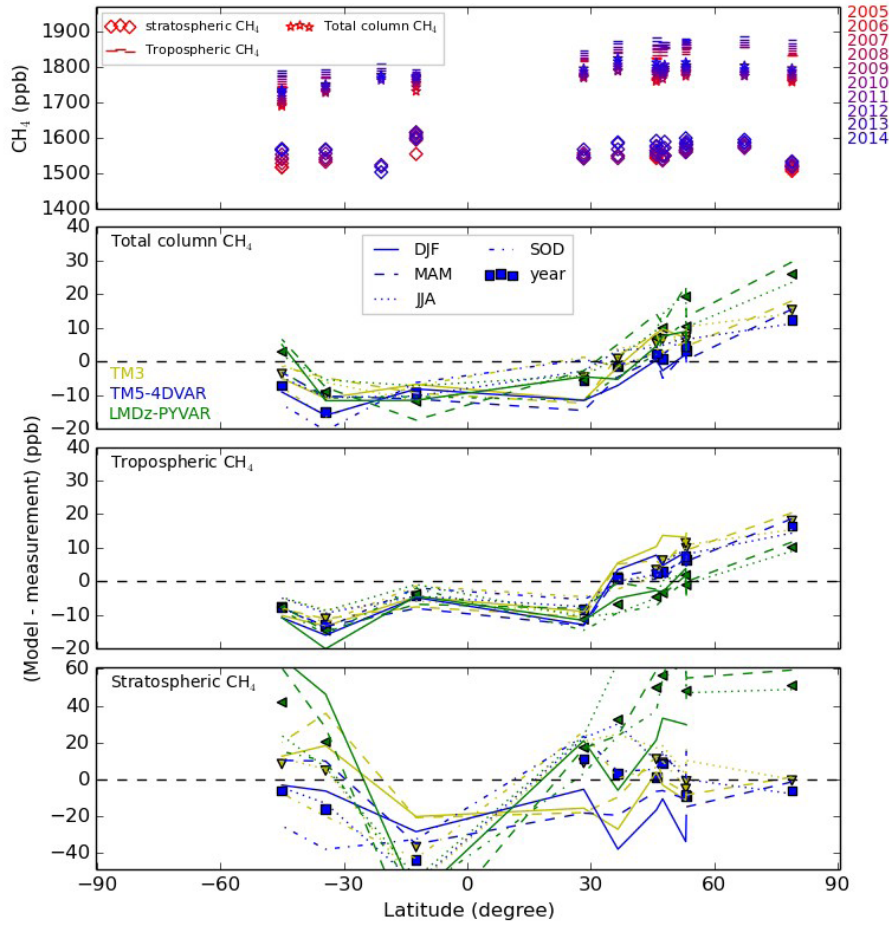


Figure 4.6. Annual mean total, tropospheric and stratospheric column-averaged CH_4 mole fractions plotted as a function of latitude. The upper panel is the results of FTS measurements while the lower panels is the difference between the measurements and the TM3 (yellow), TM5-4DVAR (blue) and LMDz-PYVAR (green) simulations. The annual mean is calculated as yearly mean of the fitted long-term variation. Medians over all time, and also split into different seasons, are shown for the differences.

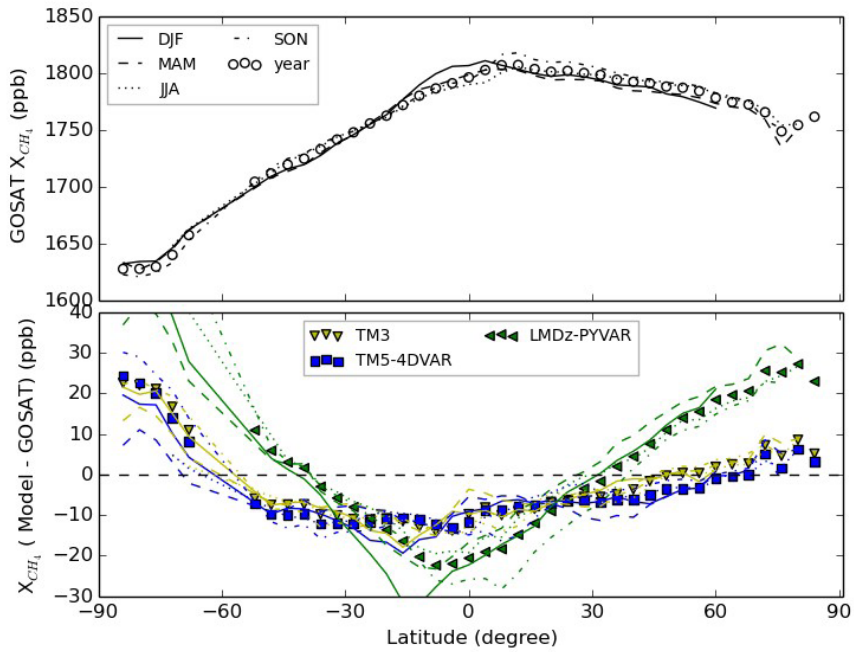


Figure 4.7. Total column-averaged CH_4 mole fraction measured by GOSAT (upper panel) and difference with simulations by the models (lower panel). The results are averaged over the period 2009-2011 and along longitude, with a latitude bin of 4° . Both averages for whole year (marked solid line) and different seasons (DJF: solid; MAM: dashed; JJA: dotted; SON: dash dot) are shown. The yellow, blue and green points represent results for TM3, TM5-4DVAR and LMDz-PYVAR respectively.

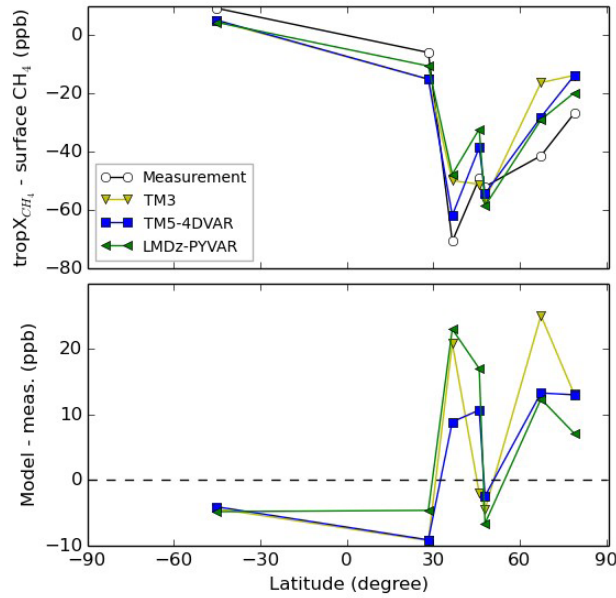


Figure 4.8. Measured (black) and simulated (yellow: TM3, blue: TM5-4DVAR, green: LMDz-

PYVAR) vertical gradients of CH₄ in the troposphere (top panel) and differences between the measurement and simulations (lower panel) against latitude.

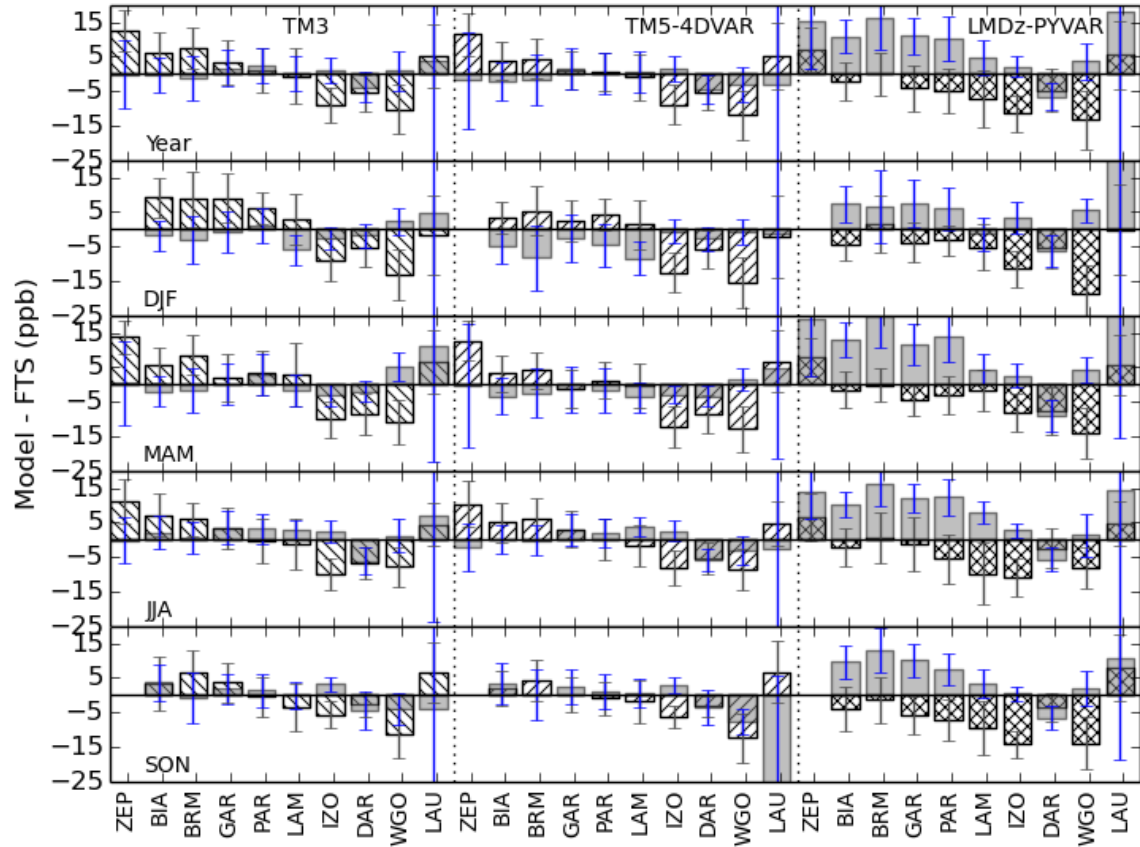


Figure 4.9. Yearly and seasonal medians of the stratospheric and tropospheric contributions in modeled total column biases at TCCON sites. The white bar denotes the tropospheric bias, the grey bar the stratospheric bias. The scale factor for the model bias is the air column fraction $P_t/1000$ (stratosphere) and $(1-P_t/1000)$ (troposphere), where P_t is the tropopause pressure. The standard deviations of the bias amplitudes are shown separately for the troposphere (black error bar) and the stratosphere (blue error bar). The results are averaged for 2007–2011 where FTS measurements are available.

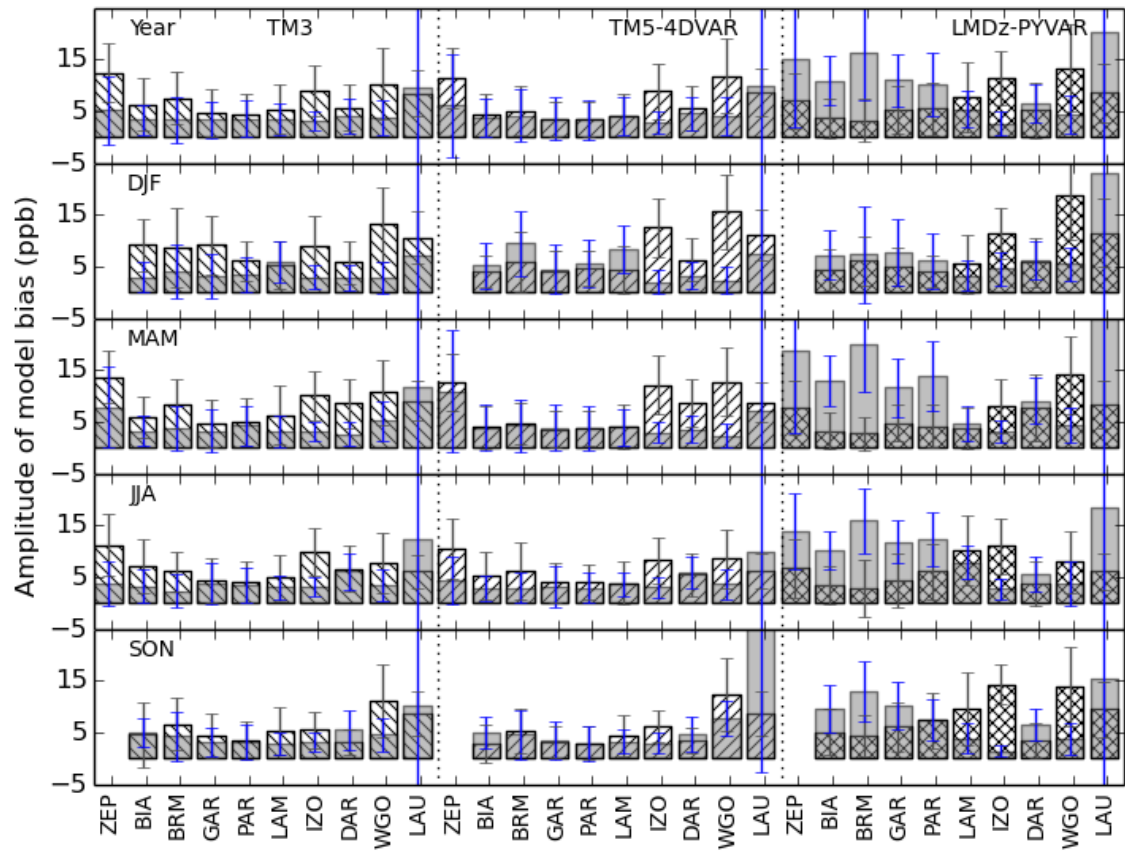


Figure 4.10. Same as Fig. 4.9 except for medians of model bias amplitudes (absolute model to FTS differences). The standard deviations of the bias amplitudes are shown separately for the troposphere (black error bar) and the stratosphere (blue error bar).

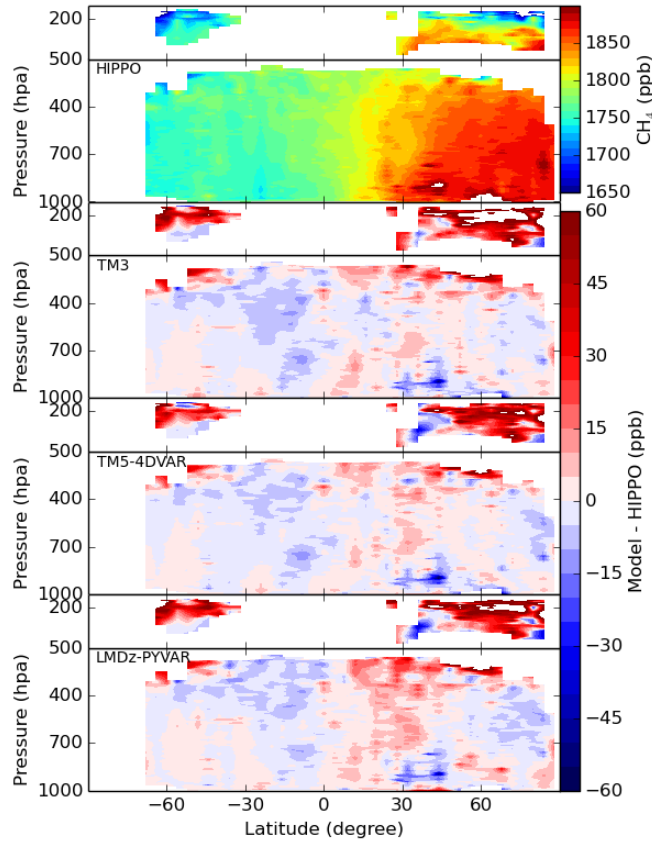


Figure 4.11. HIPPO measured CH₄ distribution in the stratosphere (short panel) and the troposphere (high panel) and differences with model simulations. The results are averages for five HIPPO missions, for latitudinal bins of 4° and vertical increments of 10 hPa.

Figure 4.11 shows a comparison between model simulations and HIPPO measurements. The results are averaged for all five HIPPO missions and longitudinally, and within grids of 4° latitude and pressure increments of 10 hPa. A significant feature is an overestimation of CH₄ in the lowermost stratosphere over latitudes higher than 30°S/N, much larger than the biases in the troposphere. It is not clear whether the overestimation arises from the residual transport in the stratosphere, which appears to be too strong, a too high tropopause or an incorrect vertical CH₄ gradient across the tropopause. Underestimations dominate in the southern troposphere, especially in upper southern troposphere, consistent with the observation that modeled gradients of tropospheric CH₄ are biased negative as revealed by FTS and surface measurements. There are no significant patterns for the vertical gradient bias in the northern troposphere. The model biases in the tropospheric xCH₄ revealed by HIPPO do not present a significant latitudinal trend as that by FTS (not shown). If the tropopause is shifted 200 hPa upward to include the lower stratosphere with high overestimated CH₄, the model biases comparing with HIPPO become closer to that by FTS. In deriving FTS tropospheric CH₄ the stratospheric CH₄ is removed by its linear correlation with N₂O. The tropopause in the FTS data therefore has a chemical definition. The difference between the

thermal/dynamical tropopause used in integrating HIPPO measurements and the chemical one could lead to the different behaviors of tropospheric model biases as revealed by FTS and HIPPO. If this is true, such an explanation could be applied to the North-South gradient in the tropospheric model biases shown in Fig. 4.6.

4.4.2. Stratospheric satellite

To further assess the ability of the models to capture the stratosphere and upper troposphere we look at comparisons with ACE-FTS. Figure 4.12 shows CH₄ concentrations along the latitude and altitude, while Fig. 4.13 shows the median (Model – ACE-FTS) bias per season. As one can see, there is a significant difference to what extent the models capture the entire profile. The typical vertical profile of CH₄ consists of quasi-constant concentrations in the upper troposphere to lower stratosphere after we see a sharp decrease to low upper stratosphere concentrations.

Compared to ACE-FTS TM3's tropospheric concentration levels reach higher altitudes after which they see a sharper drop to reach upper stratospheric concentration levels that are slightly lower than those obtained by ACE-FTS. This is featured across all latitude bands, however the concentration difference is stronger at higher latitude bands. TM5-4DVAR shows the best agreement with ACE-FTS concerning its profile shape. Its upper stratosphere concentrations are slightly overestimated but the position of the gradient is generally well executed. LMDz-PYVAR's vertical profile sees a clear mismatch with respect to ACE-FTS as a function of latitude. At higher latitudes lower stratosphere concentrations are clearly overestimated, while at the tropics the sharp decrease to upper stratosphere values occur at a much lower altitude as compared to ACE-FTS, thus significantly underestimating the CH₄ concentrations here. Also, (uniform for all latitude bands) all upper stratosphere concentrations are clearly overestimated.

Differences in the stratospheric CH₄ between the models and MIPAS are generally similar to the difference with ACE-FTS during 2009-2011 (not shown). However, MIPAS agrees with the models better than ACE-FTS in the lower stratosphere where the later mostly reveals an overestimation by the models. A comparison of the stratospheric xCH₄ between MIPAS and the models is given in Figure 4.14. Except for TM3 in the northern hemisphere, significant differences occur during polar vortex period (about 120 ppb higher than yearly median differences). The large differences are also reflected in the difference of total xCH₄ revealed by GOSAT, whose value peaks during Sep-Oct-Nov period southward of 60°S (no measurements during northern the polar vortex period northward of 60°N). The latitudes 20°S~60°S with negative differences correspond to the region with both horizontal and vertical uniform CH₄ as described in Sect. 4.4.3. For TM3 and TM5-4DVAR, the yearly median difference between models and MIPAS is about 10~20 ppb in 20°N-80°N. It is larger than the bias revealed by FTS (-10~10 ppb) in these latitudes, but is misleading due to different averaging periods (2009-2011 in the case of MIPAS). The difference between the simulated and FTS measured stratospheric CH₄ presents interannual variabilities, increases from -35~6 ppb of 2007 to -6~27 ppb of 2011 at sites in the northern hemisphere for TM3 and TM5-4DVAR. The difference in the stratospheric CH₄ between models and MIPAS also gives significant increase from

-5~10 ppb of 2009 to about 20~40 ppb of 2011 in 20°N-80°N.

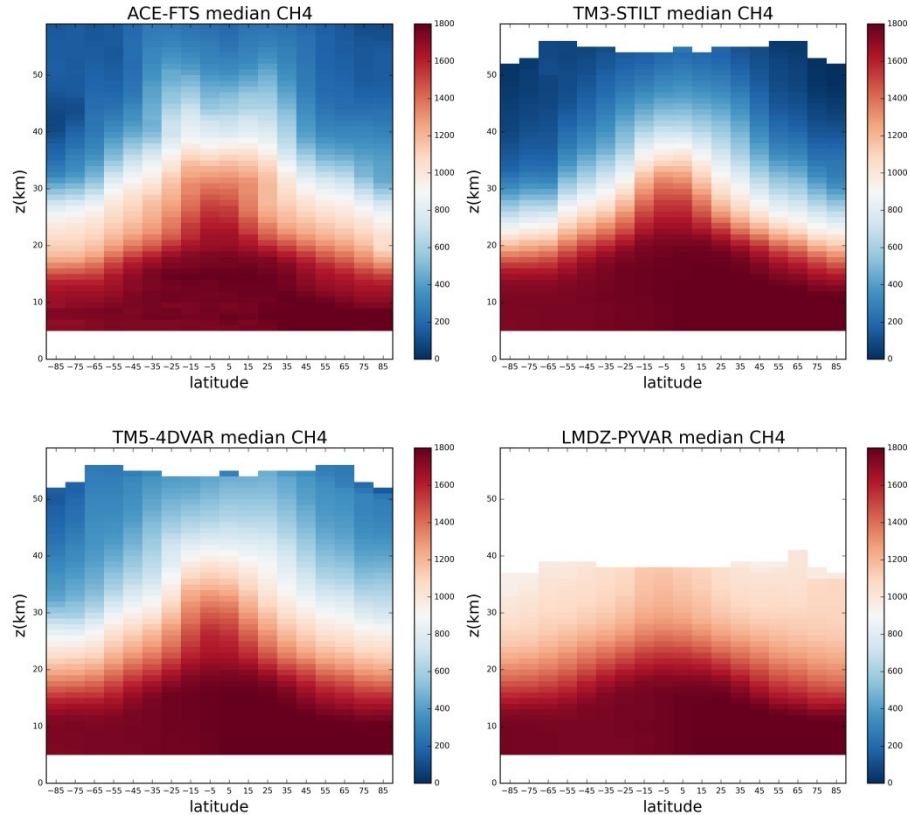
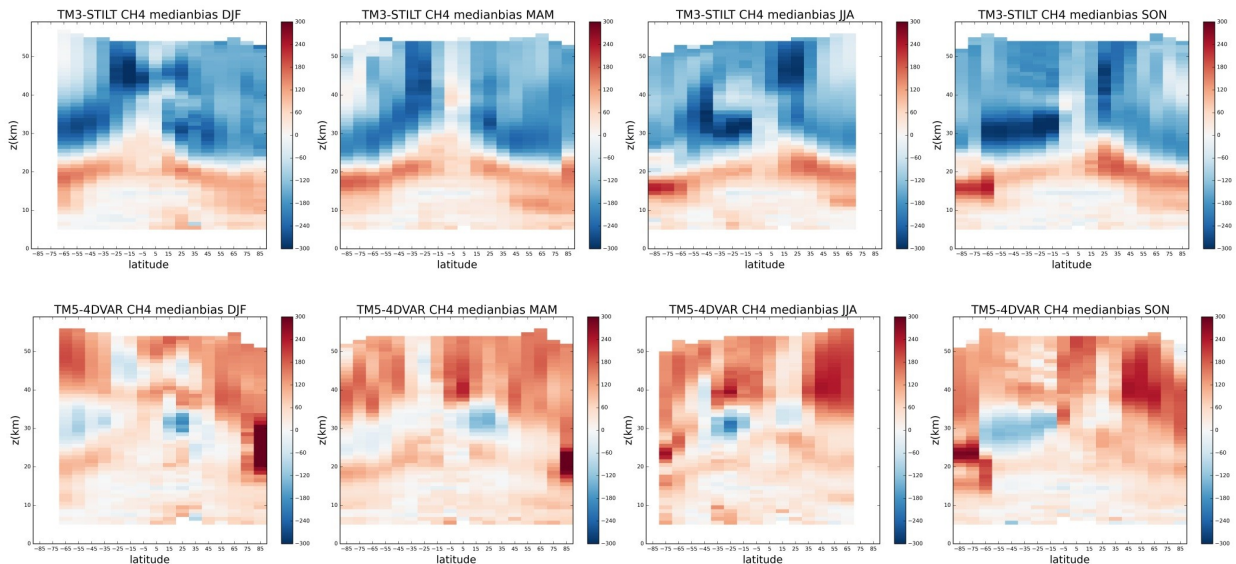


Figure 4.12. Median CH₄ concentrations as a function of latitude and altitude spanning the 2009-2011 period for ACE-FTS, TM3, TM5-4DVAR and LMDz-PYVAR.



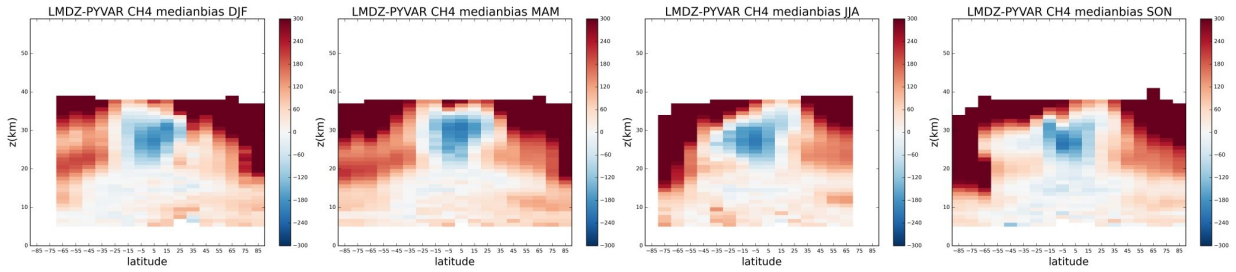


Figure 4.13. Median Model - ACE-FTS biases as a function of altitude and latitude for different seasons (DJF = December-February, MAM = March-May, etc) and models (left TM3, mid TM5-4DVAR and right LMDz-PYVAR) spanning 2009-2011 period.

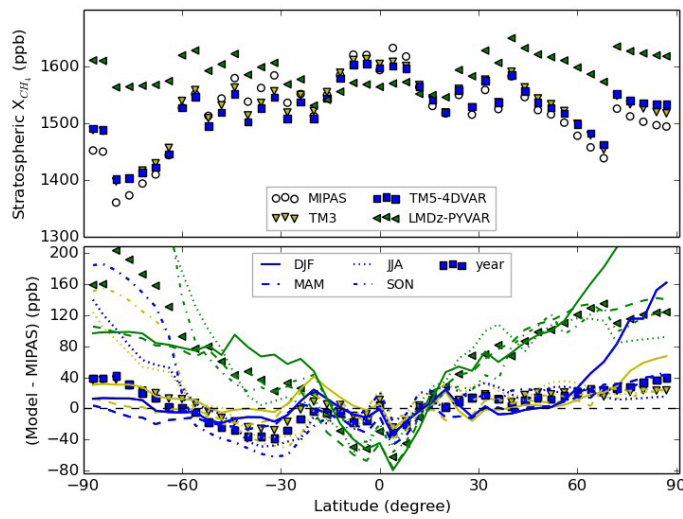


Figure 4.14. Stratospheric column-averaged CH_4 mole fraction measured by MIPAS and simulated by models (upper panel), and difference between the simulations and measurements (lower panel). The results are medians over the period 2009-2011 and along longitude, within a latitude bin of 4° . Both medians for whole year (points) and different seasons (DJF: solid; MAM: dashed; JJA: dotted; SON: dash dot) are shown. The yellow, blue and green points represent results for TM3, TM5-4DVAR and LMDz-PYVAR respectively.

4.4.3. Diagnose by Equivalent length

The equivalent length (L_e) is useful tool to quantify isentropic mixing properties in the atmosphere, which is a measure of the complexity of tracer distribution (Nakamura, 1996; Nakamura and Ma, 1997; Haynes and Shuckburgh, 2000). In the 2D case this quantity is just the length of constant tracer concentration lines if the gradient of the tracer does not change along the isolines. Mixing processes stir and scramble tracer contours and increase its complexity and then enlarge L_e .

If looking at stratospheric CH_4 distributions in Fig. 4.12 into more details, an uplift region with relative high CH_4 concentrations presents in $25^\circ\text{S} \sim 25^\circ\text{N}$ and $20 \sim 33$ km. This is the tropical

reservoir, which has weak mixing with extratropical air (Trepte and Hitchman, 1992). Among the models, TM5-4DVAR and TM3 represent high CH₄ concentration in the reservoir more or less, but the reservoir is nearly absent in LMDz-PYVAR. This is why LMDz-PYVAR modeled CH₄ decreases too quickly with altitudes in the tropics. The contrast in CH₄ concentrations between interior and exterior of the reservoir depends partly on the strength of the subtropical barrier and mixing process in extratropics. The formation of tracer concentration gradients is a result of differential mixing strength, which means small mixing in the barrier region and strong mixing in one or both sides of the barrier (Nakamura, 1996, 1997). This mechanism is applied to both the subtropical barrier and polar barrier (a region having strong tracer gradients and separating air inside polar vortex with that in mid-latitudes). In this part we calculate L_e from MIPAS measured and modeled CH₄ fields in the stratosphere. The calculation is done on isentropic surfaces in a range 450~2000 K (~18 to 49 km) in a period 2009-2011. An annual cycle of CH₄, L_e and the zonally mean zonal wind in the stratosphere is show in Figure 4.15. In this cycle the polar vortex break and rebuilt in the southern hemisphere, and built and break in the northern hemisphere.

In Oct. 2009 the southern polar vortex is still strong, large meridional CH₄ gradients around 60°S, although it start to break at levels around 1250 K (~38 km), isolines of CH₄ bend toward the pole there. In latitudes approximately 60°S~30°S it is the surf zone, which is formed by wealthy wave breaking of planetary waves propagating upward from the troposphere. The planetary wave breaking results into isentropic mixing of tracers, and then a meridional uniform distribution. The measured large L_e and uniform CH₄ along latitudes in the surf zone is consistent with our knowledge. However, in levels 450~850 K (about 18~30 km) the CH₄ in the surf zone is also almost uniform in the vertical direction. There should be vertical mixing there since CH₄ generally decreases with altitudes in the stratosphere. Some gravity-type waves are necessary to produce vertical disturbances instead of the planetary wave. At about 45°N the northern surf zone started to develop as indicated by a vertically long zone, mostly visible in levels 650~1850 K, with a little larger than its surroundings L_e .

Large L_e occurs in the latitudes 30°S~30°N as well, but is inconsistent with the results shown in Haynes and Shuckburgh (2000). In their modeled tracer fields the tropics is usually a calm region. However large L_e does not always mean strong isentropic mixing, and can be produced from diabatic movements as well. Motions cross isentropic surfaces produce anomalies on CH₄ contours on an isentropic surface due to decreasing CH₄ with altitudes. In the upper stratosphere there are diabatically vertical motions associated with the semiannual oscillation (SAO) (Kennaugh et al., 1997). Indeed, there are some correlations between the large L_e in the tropical stratosphere and the double peak structure in latitude-altitude cross sections of CH₄ in the three years results. Except for the diabatic motions, isentropic mixing is possible in the tropical stratosphere. The vertical motions in SAO are resulted from zonal forces which are due to wave breaking events. Another example is the 2-day wave (Rojas and Norton, 2007), which peaks in the mesosphere and can propagate downward to 40 km (~1350 K) and has the maximum meridional perturbation at the equator. Another difference with the results in Haynes and Shuckburgh (2000) is the highest L_e occur

poleward of 70°S/N. In their simulation mixing in both regions are really weak in this month. Strong stirring could exist inside the polar vortex but the strongest stirring locates in the surf zone (Chen et al., 1994).

Considering model performances, the polar vortex and surf zone are present in the southern hemisphere more or less. The models give a weaker mixing in the surf zone and higher CH₄ in the polar vortex, especially by TM5-4DVAR. The region with both horizontally and vertically well-mixed CH₄ is completely absent in the models. This absence is visible as a negative region of model to ACE-FTS differences during the Sep-Oct-Nov period in Fig. 4.13. This is confirmed as well by maximum underestimations or minimum overestimations by the model of FTS measured stratospheric column-average CH₄ in this season southward of 30°S (Figure 4.6). The tropical region with large L_e is represented best by TM5-4DVAR, which captures the double peak structure of CH₄ to the largest extent (not shown).

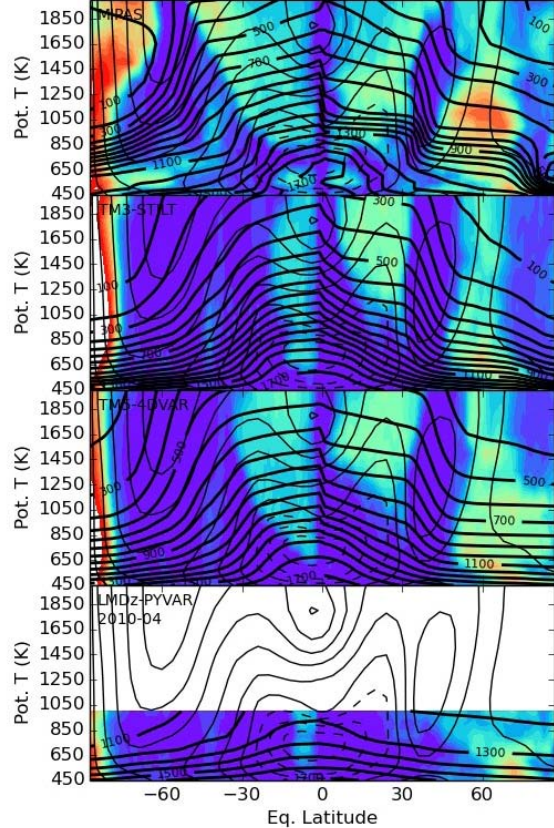
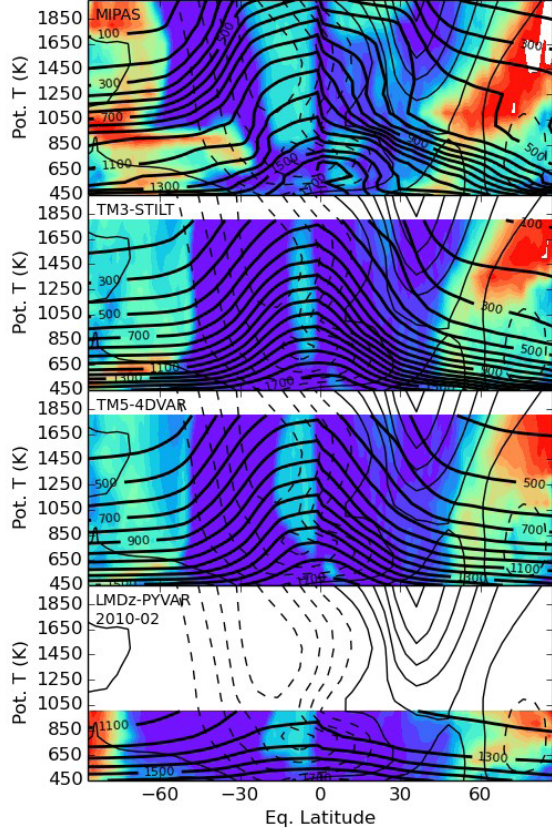
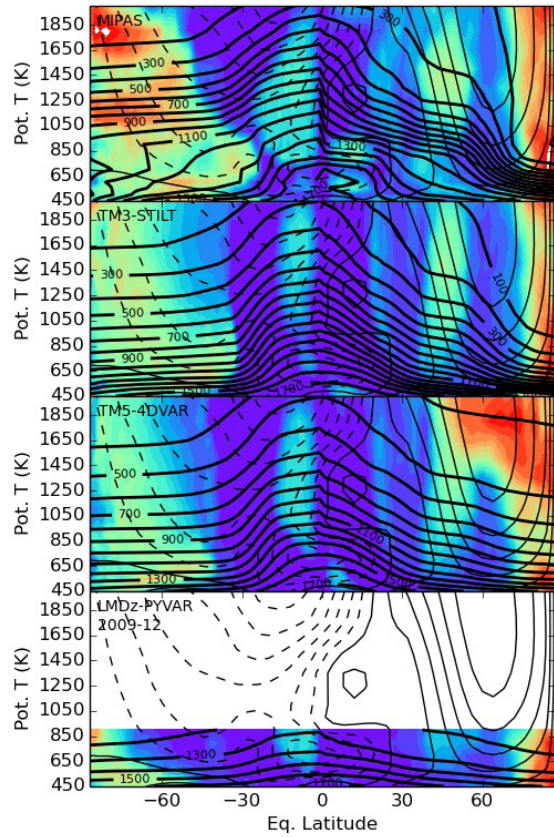
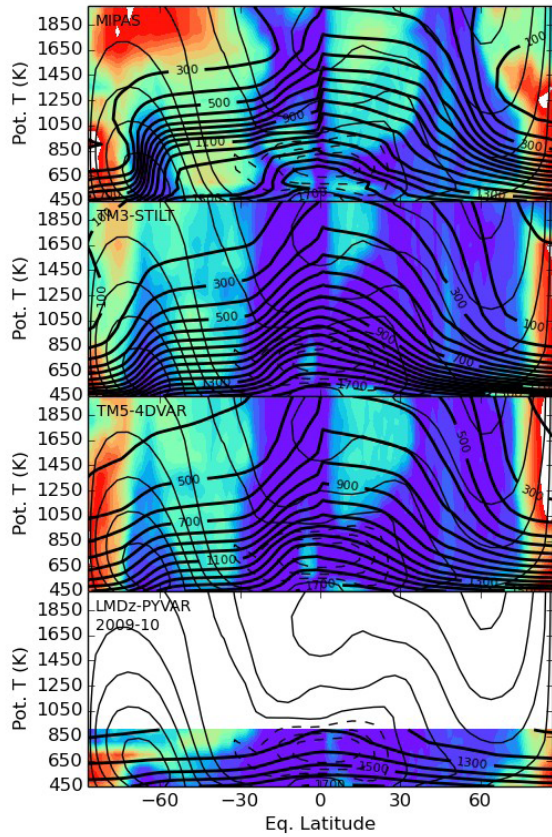
In Dec. 2009 the southern polar vortex break already, and the zonal wind changed to easterlies. The strong mixing occurred in the whole extratropics, the polar barrier with small L_e disappeared. This is consistent with the strengthening of planetary wave breaking during polar vortex breaking because of occurrence of weak zonal winds (Holton, 2004, p. 424~429). However, southern CH₄ was not well mixed at this time below 900 K (~31 km). In the northern hemisphere the polar vortex, polar barrier and surf zone was well defined now. The surf zone seemed to split into two regions above 850 K (~30 km) with smaller L_e in the region between them, or was extending toward the tropics. Similar to the southern hemisphere, a region (about 20°N~60°N and 450~850 K) with small gradients in both vertical and horizontal directions occurred. In the models southern CH₄ is horizontally uniform southward of 30°S unrealistically, and northern surf zone is represented well. CH₄ inside the northern polar vortex is overestimated, and most significantly in the case of TM5-4DVAR again.

The northern polar vortex broke above 1050 K (~35 km) in Feb. 2010 and strong stirring occurred as it was in the southern hemisphere. However, it was reestablished in the April but in smaller extent (the polar barrier located northward of 75°N) and without the polar westerly jet. During this period only weak easterlies with a maximum of 10 m/s in February and below it in April occurred northward of 60°N. The surf zone became wider (30°N~70°N) shows stronger isentropic mixing in the April than its counterpart in the February (about 35°N~45°N). The stronger mixing is consistent with weakened westerlies that are suitable for quasi-stationary planetary wave propagation and breaking. In addition, the subtropical barrier is visible, which located along subtropical jet axis and showed low L_e . In the April there is large L_e almost symmetrically distributing in the two hemispheres in the tropics above 850 K. It is this month when the double peak structure in CH₄ distributions was the most significant and occurred at altitudes above 10 hpa (~30 km) in this year as expected (Randel et al., 1998). In the southern hemisphere the situation in February is similar to that in December. But the large L_e could result from remnants from the southern polar vortex breaking (Hess, 1991) instead of strong stirring since stationary planetary wave can not propagate in easterlies. The equivalent length quantifies complexity of instantaneous contours but does not reveal the reason to it.

The model simulations show CH₄ and L_e patterns similar to measurements in February and April. The L_e southward of 60°S is underestimated in the models in February. That could reflect a too fast dissipation of polar vortex remnants. The reappearing of the northern polar vortex is represented by TM3 but a too weak contrast in CH₄ between outside and inside it. The wide and strongly stirring surf zone is replaced by a narrow and weakly mixing region in this model. In TM5-4DVAR CH₄ is completely uniform in the horizontal direction northward of ~60°N.

In Jun. 2010 the polar vortex disappeared in the northern hemisphere with a strongly stirred region left northward of 50°N and easterlies established. In the southern hemisphere the polar vortex and surf zone started to build themselves. The developing isentropic stirring in the mid-latitudes mixed with the deceasing tropical large L_e region at that time. Propagation of the planetary wave started around 40°S at 450 K level and tilt along isolines of zonal wind, consistent with the theory that the quasi-stationary planetary wave propagates in westerlies weaker than an upper limit (Holton, 2004, p. 424). That is reflected in the models as well, but with underestimated amplitudes again. The largely stirring region above 850 K and southward of ~40°S in the southern hemisphere is completely absent in the models. As a result, modeled CH₄ presents too large meridional gradients there.

In Aug. 2010 the polar vortex and surf zone matured at last in the southern hemisphere. The meridional distribution of southern CH₄ is roughly captured by the models. The deficiencies of the models are too weak isentropic mixing in the surf zone. Large departures occur at the level around 1050 K and below 700 K (~26 km) in the mid-latitudes.



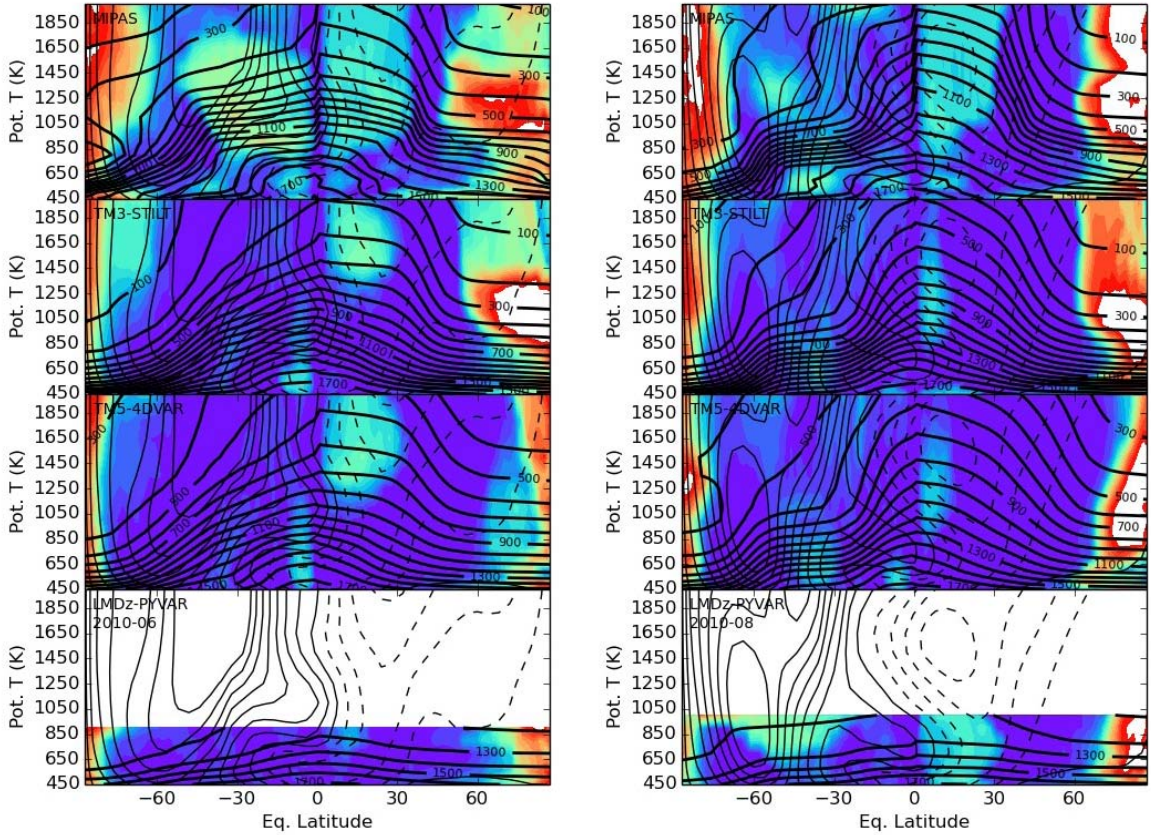


Figure 4.15. Cross sections in Oct. 2009~Aug. 2010 of equivalent length (color: the red indicates large values and the blue for small values and color is plotted on a logarithmic scale, the white means no data or larger values), contour of CH_4 (thick black line with an increment of 100 ppb) and zonal mean zonal wind (thin black lines with solid for westerlies and zero values and dashed lines for easterlies, the increment is 10 m/s) along equivalent latitudes (but latitudes for wind) and potential temperatures. The equivalent latitude φ_e is defined by $A = 2\pi a^2(1 - \sin \varphi_e)$, A is the area bounded by a constant CH_4 line on an isentropic surface and a is the earth radius. The equivalent length has been scaled by $2\pi r \cos \varphi_e$ and is unitless. Results for MIPAS, TM3, TM5-4DVAR and LMDz-PYVVAR are shown, respectively, starting from the uppermost panel.

4.4.4. Validation of simulated CH_4 vertical profiles

The algorithm retrieving CH_4 profiles described in Sect. 3.2 has not been calibrated with in situ measurements. There is only an empirical validation using in situ surface CH_4 . It can be seen that the retrieved low tropospheric $x\text{CH}_4$ follows variations of the in situ surface CH_4 well at Ny-Ålesund. There are significant differences between them at Bremen, but the retrieval is capable to follow the seasonal behavior of the surface CH_4 . With a DOFS (the degrees of freedom for signal) of around 2.5 in the retrieval stratospheric CH_4 variabilities are distinguished from those in the troposphere. Validation of simulated CH_4 profiles could provide further insight on performances of the models.

Comparisons of CH₄ profiles, partial columns above 11 km and the lower tropospheric xCH₄ between FTS and models are given in Figure 4.16 and 4.17. CH₄ is well mixed in the troposphere because of its lifetime of about 10 years and strong convection mixing there. The CH₄ concentration deceases rapidly with altitude in the stratosphere due to oxidations by OH, Cl and O(¹D). The tropopause height varies seasonally with a maximum in summer, and meridional with an increase toward the tropics. The retrieved profiles change following the tropopause as showed by Figure 4.16. In wintertimes of some years measured profiles shift downward as a whole, along with decreasing tropopause, e.g. the year 2007, 2010, 2011 and 2012 at Ny-Ålesund, 2010 and 2012 at Bremen. The shift could be caused by air subsidence associated with the polar vortex, which is stronger in winter and has larger influences at high latitudes. Total and stratospheric columns of CH₄ are small in this period.

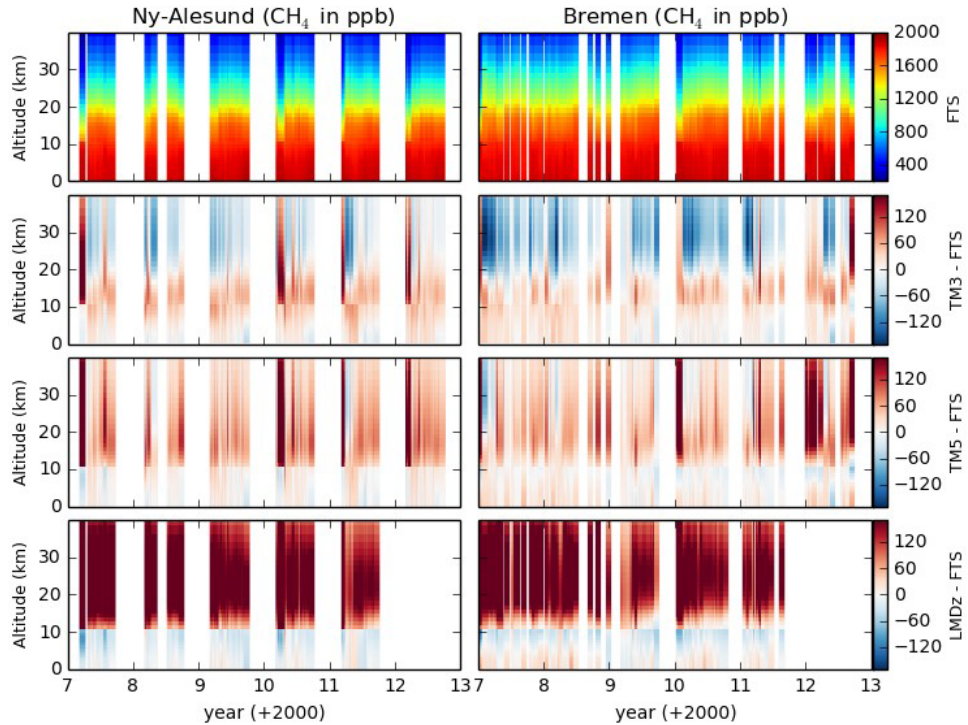


Figure 4.16. Comparison between FTS retrieved CH₄ profiles and those simulated by models at Ny-Ålesund (left) and Bremen (right). The model profiles have been smoothed with averaging kernels of the retrieval taking a prior into account. The first row is the retrieved profiles, and following rows are differences between retrieval and simulation for TM3, TM5-4DVAR and LMDz-PYVAR respectively. The colors indicate CH₄ mole fractions.

Differences of stratospheric CH₄ between FTS and the models are largest for LMDz-PYVAR. Overestimation of CH₄ in the stratosphere by this model is consistent with the results in Sect. 4.4.2.

TM3 overestimates CH₄ in the lower stratosphere and underestimates in the upper stratosphere. TM5-4DVAR overestimates in the whole stratosphere, but has the best agreement with FTS concerning the shape of stratospheric CH₄ profiles. However, overestimation of partial columns by TM3 and TM5-4DVAR are not consistent with their underestimation for the stratospheric xCH₄ showed in Sect. 4.4.2. FTS measured CH₄ profiles should be calibrated with in situ measurements before a clear conclusion is drawn. In the period influenced by the polar vortex, all the models overestimate CH₄ mole fractions in the stratosphere significantly. It is indicated by positive difference zones spreading in the whole stratosphere in Figure 4.16, and large partial column differences in Figure 4.17, with a strength increasing for TM3, TM5-4DVAR and LMDz-PYVAR.

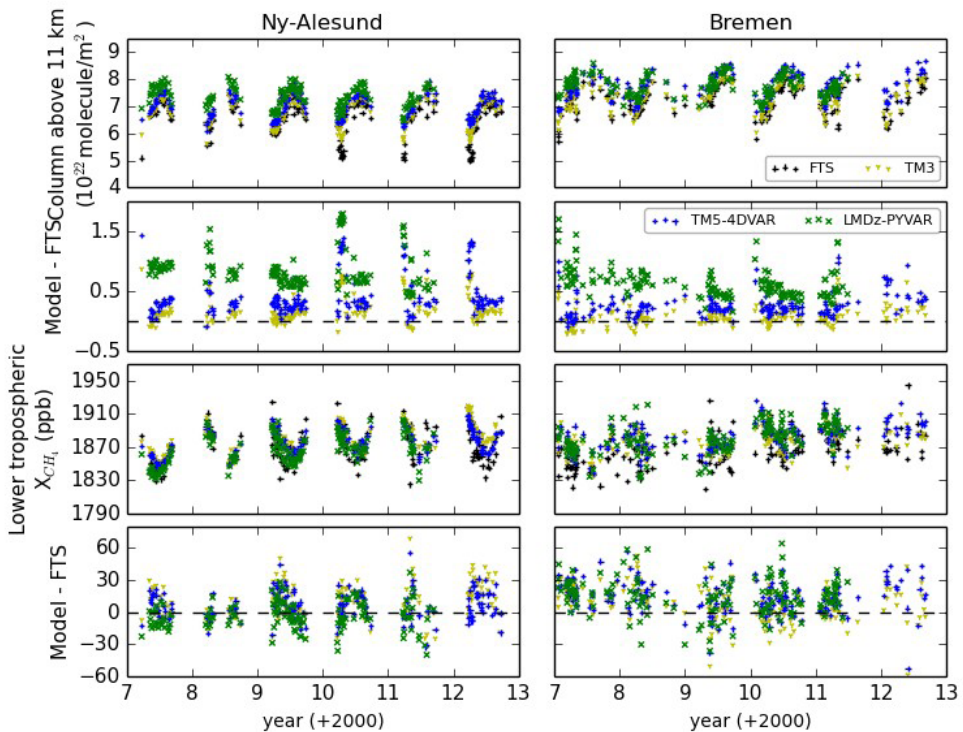


Figure 4.17. Comparisons of partial column of CH₄ (first two rows) and lower tropospheric column-averaged CH₄ mole fraction (last two rows) between FTS measurements and model simulations at Ny-Ålesund (left) and Bremen (right). The partial column is an integration of CH₄ profile from 11 km to TOA (top of the atmosphere). The lower tropospheric column-averaged CH₄ mole fraction is a mean mole fraction of profile below about 2.4 km. The shown results are daily medians.

The bias in the LMDz-PYVAR partial column deceases with time at both sites, and does not change for the other models. Because such a trend does not occur in differences of the lower tropospheric xCH₄, and of the tropospheric xCH₄ as shown in Sect. 4.4.2, it could not be source-related. Since the method retrieving the lower tropospheric xCH₄ is not calibrated against in situ measurement, no

conclusion will be drawn on relative performances of the models.

4.5. Summary

In this chapter, the simulated CH₄ mole fractions by three European inverse modeling are validated using the measurements from ground-based FTS and satellites, and in situ measurements at surface. The aim is to determine whether most of model biases are located in the stratosphere or troposphere. With FTS stratospheric and tropospheric xCH₄, retrieved from total column FTS measurements, it is shown that model bias amplitudes are 7.4±5.1 ppb, 6.72±4.8 ppb and 7.1±5.6 ppb in the troposphere for TM3, TM5-4DVAR and LMDz-PYVAR. For the stratosphere we get 4.3±9.9 ppb, 4.7±9.9 ppb and 10.3±15.9 ppb, respectively. The tropospheric model bias exhibits a North-South gradient with an overestimation in northern high-latitude for all models. There is not a latitudinal pattern existing through the year in the stratospheric model bias except for LMDz-PYVAR, which overestimates stratospheric CH₄ at high-latitudes and underestimates in the tropics.

The evaluation of the models at surface shows a smaller bias compared to the tropospheric xCH₄. We assume that the tropospheric model biases are mainly located in the middle and upper troposphere although comparisons at the surface are only limited to sites where the measurements have been assimilated into the models. Comparisons with HIPPO show that there are significant underestimations in the southern upper troposphere while biases in the lower troposphere are smaller. HIPPO and FTS reveal different behaviors in tropospheric model biases. A sensitive test shows that differences between thermal/dynamical and chemical tropopause could be the reason, as well as for the FTS revealed North-South gradient in the tropospheric model biases.

The equivalent length is calculated to investigate the causes of model biases in the stratosphere. The modeled surf zone in the southern hemisphere is not developed to the same extent as in the measurement because a too weak planetary wave breaking there. Especially in Jun-Jul-Aug period stratospheric CH₄ in southern mid-latitudes presents much larger isentropic gradients in the models than measurements. During the development of the southern surf zone, a region with both vertically and horizontally well mixed CH₄ occur between 450 and 850 K (~18 and 30 km) in surf zone latitudes. Such a region is absent in the models, and underestimations of CH₄ within it are visible in comparisons with ACE-FTS and MIPAS measured CH₄ profiles, and FTS measured stratospheric CH₄ columns. More work are needed to uncover which kinds of atmospheric movement provided this vertical mixing. The modeled polar vortex breaks too fast compared to the measurements. Modeled CH₄ concentrations in the polar vortex rise at all levels at same time instead of at high levels initially as in the measurements.

5. Retrieval of the isotopic composition of atmospheric CO₂ from ground-based FTS solar absorption measurements

The isotopic composition of carbon is different between its global reservoirs, for example, the ratio ¹³C/¹²C increases for fossil fuel, terrestrial biosphere, the ocean and the atmosphere successively. Exchanges of carbon between two carbon reservoirs usually occur along with a distinct selection of one isotope over the other. The photosynthesis of the plants prefers ¹²C over ¹³C, and respiration releases more ¹²C isotope. The relative abundance of carbon isotopes is expressed in parts per thousand, for example, for ¹³C/¹²C,

$$\delta^{13}C = \left(\frac{{}^{13}C / {}^{12}C_{sample}}{{}^{13}C / {}^{12}C_{standard}} - 1 \right) 1000. \quad (5.1)$$

The standard value of ¹³C/¹²C is PDB (Pee Dee Belemnite) that is 0.0112372. The $\delta^{13}C$ is about -6.7 to -7.4 for atmospheric CO₂ (Keeling, 1960) that is a major molecule containing carbon in the atmosphere, -10 for the ocean, -12 to -28 with a mean of -26 for the plants (Craig, 1953) and -21 to -28 with a mean of -24 for fossil fuel (Craig, 1953). Measurements of both concentration and $\delta^{13}C$ of atmospheric CO₂ can help to infer contributions of various sources and sinks. Atmospheric CO₂ is produced mainly by respiration and the burning of fossil fuels, removed mainly by uptake of plants, and exchanged with the CO₂ in the oceans. While the exchange with ocean does not significantly influence the isotopic composition of CO₂, respiration and fossil fuels burning release more ¹²CO₂ into the atmosphere, and photosynthesis uptake more ¹²CO₂ into the plants. An increase in atmospheric CO₂ concentration caused by fuel combustion will be accompanied by a decrease in $\delta^{13}C$, such as the well-known increasing atmospheric CO₂ concentration and the accompanied decreasing $\delta^{13}C$ since the industrial revolution. In a region where the plants have influence on the atmospheric CO₂ concentration, CO₂ mole fraction will be anti-correlated to the $\delta^{13}C$ (Keeling et al., 1958, 1979; Mook et al., 1983). The atmospheric CO₂ concentration presents minimum in summer when the photosynthesis is strong and the $\delta^{13}C$ has the least negative value. When there is only a small to zero fraction of CO₂ originated from the plants, the anti-correlation between atmospheric CO₂ and $\delta^{13}C$ will be weak. From a limited measurements (Keeling et al., 1984) the $\delta^{13}C$ of atmospheric CO₂ increased steadily southward from -7.55 near 16°N to -7.47 near 17°S, as expected from a dominant CO₂ source from fossil fuel combustion in northern hemisphere.

While all the existed data of ¹³C/¹²C are from in situ measurements, remote sensing could provide additional data source. In this chapter, the possibility of retrieving ¹³CO₂/¹²CO₂ from ground-based FTS solar spectra will be explored.

5.1. Problems of retrieving atmospheric CO₂ isotopes from ground-based FTS spectra

Because the variation of ¹³CO₂/¹²CO₂ is on an order of one per thousand, a measurement needs have

a precession and accuracy above one per thousand. The total column measured by TCCON can achieve a precession of about 0.1% under clear condition. However, the TCCON measurements present an airmass-dependent artifact that causes the retrievals to be approximately 1% larger at 20° SZA (solar zenith angle) than at 80° SZA. The reasons resulting in this phenomenon could be spectroscopic inadequacies and instrumental problems. Currently an empirical correction is applied to remove this artifact, which represents the error as a function of SZA (Wunch et al., 2011). If considering spectroscopic inaccuracies only, it can be proved (Appendix B) that the retrieved quantity can be expressed as,

$$\hat{x} = [I + C \left(\frac{Y_1 P_s}{\cos(SZA)}, \tilde{y}_1; \dots; \frac{Y_J P_s}{\cos(SZA)}, \tilde{y}_J \right)] [x + (A - I)(x - x_a)], \quad (5.2)$$

where, \hat{x} , x , x_a are the retrieved, true and a prior state. A is the averaging kernel and I is a unit matrix, C is a diagonal matrix function representing influence of spectroscopic inaccuracies. \tilde{y}_j is the mole fraction profile of the j th gas normalized by its column-averaged mole fraction Y_j . P_s is surface pressure. The physical meaning is clear that influences of the spectroscopic error depend on abundances and vertical distributions of atmospheric gases, surface pressure in addition to SZA. For a profile scaling retrieval, such as being done in GFIT, the state is the scale factors for a prior profiles. The diagonal elements of the matrix C is a constant for each retrieved gas. When interference between different gases is ignored and variabilities of vertical profile shape is ignored, which is small for atmospheric CO₂, Eq. 5.2 can be written as,

$$\hat{Y} = \left(\int_0^{P_s} [y + (A - I)(y - y_a)] dp \right) [1 + C \left(\frac{Y P_s}{\cos(SZA)} \right)]. \quad (5.3)$$

In this case the function C can be derived from retrievals in some days with clear sky when variabilities of the column-averaged mole fraction are small and that of SZA is as large as possible. Then the variabilities of the retrieval are totally from the function C except for an absolute scale. Although an empirical correction is possible to approximately remove airmass-dependent artifact, it is always preference to reduce retrieval error through improving spectroscopic parameters and instrument performance.

Interference error is another important error source (Sussmann and Borsdorff, 2007), especially that from H₂O for ground-based remote sensing. Interference error originates from spectral residuals due to interfering gases whose spectral features overlap with the signatures of the target gases. Its amplitude depends on vertical profiles and spectroscopic errors of the interfering gases and airmass. H₂O interferes retrievals of most gases because of its widely spread absorption lines in infrared region. The profile and concentration of H₂O in the atmosphere is highly variable, the same is true for its interference.

5.2. Spectroscopy aspect

When solar radiation passes through the atmosphere, interactions between the radiation and the

molecules in the atmosphere take place. The molecules can absorb and emit radiation at frequencies that are specialized for each kind of molecule. The internal states of the molecules are discrete and the same are the energies associated with them. The absorption and emission are achieved through transitions from initial states to final sates. The lifetimes of molecular states are limited value, then the energies of the states spread over a range whose width is anti-proportional to the length of the lifetime according to the Heisenberg uncertainty principle. Consequently, the absorption and emission associating with each pair of initial and final states spread over a range of frequency as well, which is described by the spectral line function. For a molecule free from the collision with other molecules and without thermal motion, the lifetime of its states is mainly determined by spontaneous photon emission, the spectral line has negligible width, and can not be resolved by current experimental techniques.

The molecule in the atmosphere undergoes thermal motion all the time. The motion leads to the Doppler shift for the absorbed and emitted radiation frequency. The speed of the motion is described by the Maxwell-Boltzmann distribution, assuming the atmosphere satisfies the local thermal equilibrium condition. The resulted spectral line is broadened, and expressed as,

$$I_D(\omega) = \frac{1}{\sqrt{\pi} \Delta \omega_D} e^{-((\omega - \omega_0)/\Delta \omega_D)^2}, \quad (5.4)$$

where, ω is angular frequency, ω_0 is the frequency at the maximum under zero pressure condition. $\Delta \omega_D = \omega_0 \sqrt{2 k_B T / m} / c$ is the Doppler half width at the $1/e$ maximum, T is temperature, m the mass of the molecule, c the light speed and k_B the Boltzmann constant.

Collisions between molecules can change the thermal equilibrium distribution of molecular speed. Because the molecular speed prefers changes toward smaller value, the speed distribution is narrowed. As a result, the Doppler line shape is narrowed, namely the Dicke narrowing effect. But it is important for the light molecule only, such as H₂ and HF, and is much less important than another collisional effect in the atmosphere. During the collisions there is energy transfer between the energy associated with molecular states and translational energy of the molecules. Because kinetic energy of the molecular thermal motion is much larger than the energy associated with molecular rotation, this energy transfer is efficient to change rotational states of the molecules. The lifetime of molecular states is deceased due to the collisions, and spectral line resulted from the state transition is broadened. The collision-broadened line shape, namely Lorentz profile, can be expressed as,

$$I_L(\omega) = \frac{1}{\pi} \frac{\gamma P}{(\omega - \omega_0 - \delta P)^2 + (\gamma P)^2}, \quad (5.5)$$

where, P is pressure and δ is collision-induced shift coefficient and γ is collision-induced broadening coefficient. The Lorentz profile is derived under the impact approximation, which states that the time spent to the collision is much smaller than the time for the molecule to move freely, and the binary collision assumption that states only two molecules participate during each collision.

When ignoring the Dick narrowing effect, considering both the Doppler and collision broadening,

the resulted spectral line shape is called Voigt profile. The Voigt profile can be expressed as (Hartmann et al., 2008, p. 79),

$$I_V(x, y) = \int_{-\infty}^{\infty} I_D(\tilde{x}') I_L(x - \tilde{x}', y) d\tilde{x}' = \frac{1}{\sqrt{\pi}} \operatorname{Re} \left(\frac{i}{\pi} \int_{-\infty}^{\infty} \frac{e^{-t^2}}{x - t + iy} dt \right), \quad (5.6)$$

where,

$$\begin{aligned} \tilde{x} &= \frac{\omega - \omega_0}{\Delta \omega_D}, \quad x = \frac{\omega - \omega_0 - \delta P}{\Delta \omega_D}, \quad y = \frac{\gamma P}{\Delta \omega_D}, \\ I_D(\tilde{x}) &= \frac{1}{\sqrt{\pi}} \exp(-\tilde{x}^2), \quad I_L(x, y) = \frac{1}{\pi} \frac{y}{x^2 + y^2} \end{aligned}$$

The collision-induced broadening and shift present a dependence on the speed of absorber. An empirical model, the quadratic model (Rohart et al., 1994), is used describe this behavior,

$$\gamma(v) = \gamma + \gamma_2 \left(\frac{v^2}{\tilde{v}^2} - \frac{3}{2} \right), \quad \delta(v) = \delta + \delta_2 \left(\frac{v^2}{\tilde{v}^2} - \frac{3}{2} \right),$$

where v is the speed and \tilde{v} is the most probable speed. γ and δ are broadening and shift coefficient averaged over the Maxwell-Boltzmann distribution of the speed. γ_2 and δ_2 are corresponding speed-dependence parameters. After taking the speed dependence, the spectral line shape can be written as (Hartmann et al., 2008, p. 98),

$$\begin{aligned} I_{sdV}(\omega) &= \frac{1}{\pi} \operatorname{Re} \left\{ \int f_M(\vec{v}) [\gamma(v)P - i(\omega - \omega_0 - \delta(v)P - \vec{k}\vec{v})]^{-1} d\vec{v} \right\}, \\ &= \operatorname{Re}[J_{sdV}(\omega)] \end{aligned} \quad (5.7)$$

where, $f_M(\vec{v})$ is the Maxwell-Boltzmann distribution of the velocity of the absorber. \vec{k} is radiation propagation vector and $\vec{k}\vec{v}$ is the Doppler shift. In this thesis only γ_2 is considered, and speed-dependence of collisional shift is ignored.

Except for narrowing and broadening, there is a further effect resulted from the collisions, namely line mixing. The molecules in the atmosphere spread over all possible internal states according to Maxwell-Boltzmann distribution under the condition of local thermodynamic equilibrium. The equilibrium distribution is achieved through frequent collisions between molecules, which cause exchange of the population of the molecules at each state with the other states. A photon with a frequency ω_f is absorbed by a molecule through the transition from initial state i to final state f , $f \leftarrow i$. Because of the collisions there exist transfers between populations of different states, for example $i \leftrightarrow i'$ and $f \leftrightarrow f'$, which are not related to absorption or emission. The initial state can change to i' and transit to f' through absorbing a photon with a frequency $\omega_{f'i'}$, and then the state f' changes to f after the collisions. The second path $f \leftarrow f' \leftarrow i' \leftarrow i$ actually contributes absorption with a frequency associating with a different transition $f' \leftarrow i'$. Of course, the transition $f' \leftarrow i'$ can contribute absorption at the frequency possessed by the transition $f \leftarrow i$ as well. The strength of the line mixing

effect depends on the efficiency of collision-induced transfer between different states. The transfer is possible for rotational states of the same kind of molecule and isotope, so the line mixing occurs between lines within the same vibrational band. The transfer efficiency increases with collision frequency and then pressure. To keep an equilibrium distribution the transfer from the state with high population to that with low population needs to be less efficient than the inverse direction. Consequently, the line mixing decreases absorption of weak lines and increases that of strong lines. In a frame of the Rosenkranz first-order approximation, ignoring the speed-dependence of collisional effects, the spectral line density accounting for the line mixing effect can be expressed as (Hartmann et al., 2008, p. 160),

$$I(x, y) = \frac{S}{\sqrt{\pi}} \operatorname{Re}[(1 - iPY) \frac{i}{\pi} \int_{-\infty}^{\infty} \frac{e^{-t^2}}{x - t + iy} dt], \quad (5.8)$$

where, Y is the first-order line mixing coefficient. S is integrated intensity of the line, and has a form,

$$S = \frac{8\pi^3}{3hc} \frac{\omega_0}{\Delta\omega_D} [1 - \exp(-h\omega/2\pi k_B T)] \rho d^2,$$

where, ρ is the equilibrium relative population of the initial state of the line, d is the reduced matrix element of the dipole moment that couples radiation and the molecules. When both the line mixing and speed-dependence of collisional broadening are taken into account, the spectral line density will become (Hartmann et al., 2008, p. 338),

$$I(\omega) = S \operatorname{Re}[(1 + iPY) J_{sdV}(\omega)] \quad (5.9)$$

There are several other mechanisms influencing spectral line shape, but not considered in the thesis. As a summary, the parameter describing the absorption coefficient of a line are, intensity, pressure broadening and shift coefficient, first-order line mixing coefficient, speed-dependence parameter of collision-induced broadening and those specifying their temperature-dependence.

5.2.1. Inversion of spectroscopy parameter from ground-based FTS spectra

With function format of spectral line shape at hand, the next step is to determine the parameters in the function. The parameters can be predicted theoretically (Hartmann et al., 2013; Lamouroux et al., 2010; Gabard and Boudon, 2010) or determined from laboratory measured spectra (Toth, 2005; Jenouvrier et al., 2007; Devi et al., 2007). An alternative approach is retrieving the line shape parameters from the solar spectra measured by ground-based FTS (Schneider and Hase, 2009). While for the measurements in the laboratory the pressure, temperature and constituents of the gas can be controlled, it is not the case for atmospheric spectra. A further problem is that the vertical distribution of the gas in the atmosphere is variable and not easy to measure. During measurements, the atmospheric state usually changes, which make it not feasible to measure over a long time in order to reduce noise, as being done in laboratory. However, the amount of the gas in the atmosphere can be much larger than that can be provided in the laboratory, for example H_2O and

CO_2 . The solar line is an exception, which is resulted from absorption by the sun itself, must be investigated using, either ground- or space- based solar spectra (Hase et al., 2010).

In this section, the spectroscopy parameters of H_2O , solar line and CO_2 are retrieved using ground-based FTS solar spectra. The influences of these derived parameters on the retrieval of these gases are checked. The algorithm is based on the optimal estimation theory (OE), as described in Chapter 2. The code basically contains two parts: 1) execute GFIT/PROFFIT to adjust amount of atmospheric gases and fit solar spectra; 2) adjust spectroscopy parameters of target gas based the OE theory to fit the spectra further. The step 1 and 2 are iteratively executed until a convergence of the retrieved parameter is achieved. Spectroscopic parameters usually present a smooth variation along with quantum number m , which is $-J''$, J'' and $J''+1$, respectively, for P , Q and R branch transitions and J'' is rotational quantum number of initial state. The algorithm allows a usage of a smooth constraint for variations along m . Instead of using the Gauss-Newton method to search spectroscopy parameters minimizing fitted residuals, the Levenberg-Marquardt method (Kelley, 1999, p. 56) is used,

$$x_{i+1} = x_i + (S_a^{-1} + k_i^T S_\epsilon^{-1} k_i + \lambda B_1^T B_1 + v D)^{-1} [k_i^T S_\epsilon^{-1} (y - f(x_i)) - (S_a^{-1} + \lambda B_1^T B_1)(x_i - x_a)],$$

where D is a diagonal matrix with the same diagonal elements with the matrix $S_a^{-1} + k_i^T S_\epsilon^{-1} k_i + \lambda B_1^T B_1$, the other symbols have the same meaning as in Chapter 2. The factor λ determines the strength of the smooth constraint. B_1 is the second matrix in Eq. 2.12, but its rows and columns are rearranged because spectroscopic parameters are not arranged along m (along wavenumber of spectral lines here) in x . Only the rows of B_1 corresponding the parameters with smooth constraint applied have non-zero elements. The scale factor v is used to adjust step size and direction, and is determined based on the trust region method (Kelley, 1999, p. 57). the a prior covariance S_a is constructed using uncertainties given in HITRAN database, the measurement error covariance is diagonal and its elements are estimated from measured spectra. The state vector x contains the parameters of all lines, y and $f(x)$ are vectors containing all measured and calculated spectra. The Jacobean k contains derivatives of the line parameters with respect to all the calculated spectra.

The evaluation of the Jacobean of spectroscopy parameters uses numerical perturbation method and is time-consuming. An approximate method is applied when a lot of spectra and absorption lines are involved. When calculating perturbation effects of parameters of a line, only the absorption of this line is considered. Then the Jacobean is obtained through multiplying the perturbation effects by spectra containing absorption of all lines. The calculation would be accurate if ignoring instrumental effect, which convolves spectra with the instrumental line shape function.

The information about spectroscopy parameters contained in the ground-based spectra is much less than that can be obtained from laboratory spectra since temperature, pressure and gas concentration in the atmosphere vary in much smaller ranges than those achieved in the laboratory. Including spectra measured at FTS stations at different altitudes can enlarge pressure variability, and measured

at different latitudes and seasons enlarge temperature variability. The spectra measured at larger SZA contain more contribution from lower atmosphere, and then increase equivalently pressure. At the same time, the amount of absorbers increases approximately with $1/\cos(SZA)$, then changing SZA is an efficient method to control it.

5.2.2. H₂O

Although there is a large amount of work on the H₂O spectroscopy already, the accuracies of them are still not enough for atmospheric remote sensing using ground-based observation, such as TCCON and NDACC spectra. In the region around 4901 cm⁻¹ where a strong ¹³CO₂ band presents there is strong H₂O absorption as well. There is some residual features corresponding to H₂O lines always exist when using either GFIT spectroscopy parameter, which is basically from Toth (2005) with some weak lines added, or HITRAN 12 for H₂O. These residuals could inference the retrieval of ¹³CO₂, especially when air is humid and SZA is large.

Near-infrared spectra at TCCON site: Darwin (12.456°N, 130.892°E, 30 masl), Orléans (47.970°N, 2.113°E, 130 masl), Bialystok (53.231°N, 23.026°E, 183 masl) and Lamont (36.604°N, 97.486°W, 320 masl), totally 13 records, are used. Because large variabilities of H₂O vertical distribution, in situ measurements are used to prescribe the vertical profile shape. At Darwin and Lamont, Vaisala RS92 radiosonde (Miloshevich et al., 2009) measurements are used, together with a correction for RS92 H₂O measurements. The aircraft measurements from the IMECC campaign (see Sect. 3.1.2) are used for the spectra measured at Orléans and Bialystok. The in situ measurements are matched with the FTS measurements within 5 minutes. The measured H₂O, temperature and pressure profiles will act as a prior, in the case of H₂O, or forward model parameter, in the case of Tp profiles, in the retrieval code GFIT/PROFFIT. The temperature and H₂O profiles are shown in Figure 5.1. For a H₂O line with an intensity of 8.5×10^{-25} cm⁻¹ the DOFS is about 4.8 when the six parameters (vacuum wavenumber, intensity, air- and self- broadened half width, air pressure-induced shift, temperature-dependence exponent for the air-broadened half width) are fitted.

The algorithm is applied to invert H₂O spectroscopy in the region 4724.40 to 4773.60 cm⁻¹, where absorption is dominated by H₂O and with small contribution from CO₂ and N₂O. The a prior H₂O spectroscopy is the GFIT one (Toth, 2005). Only the lines with intensities larger than 2.0×10^{-26} cm⁻¹ are considered. For lines stronger than 1.5×10^{-25} cm⁻¹, four parameters (vacuum wavenumber, intensity, air- and self- broadened half width) are adjusted, and only the first three for others. In this test, GFIT is executed to fit measured spectra. The a prior profiles are scaled for species, H₂O, ¹²CO₂, ¹³CO₂, C¹⁸OO and N₂O and just kept as climatologies for all other species.

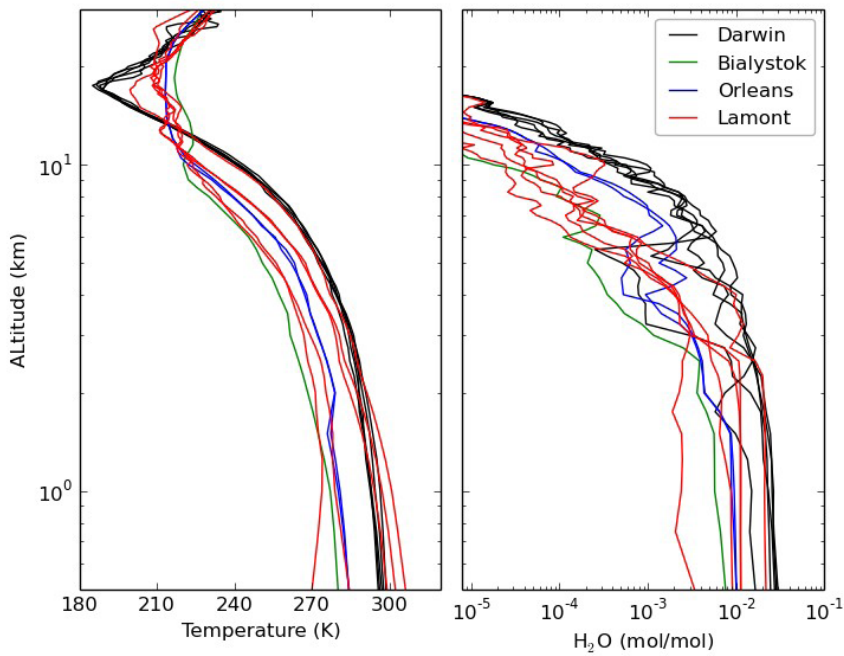


Figure 5.1. Temperature (left) and H₂O (right) profiles measured by radiosonde (Darwin and Lamont) and aircraft (Bialystok and Orléans) near the time of FTS measurements used for inverting H₂O spectroscopy parameter.

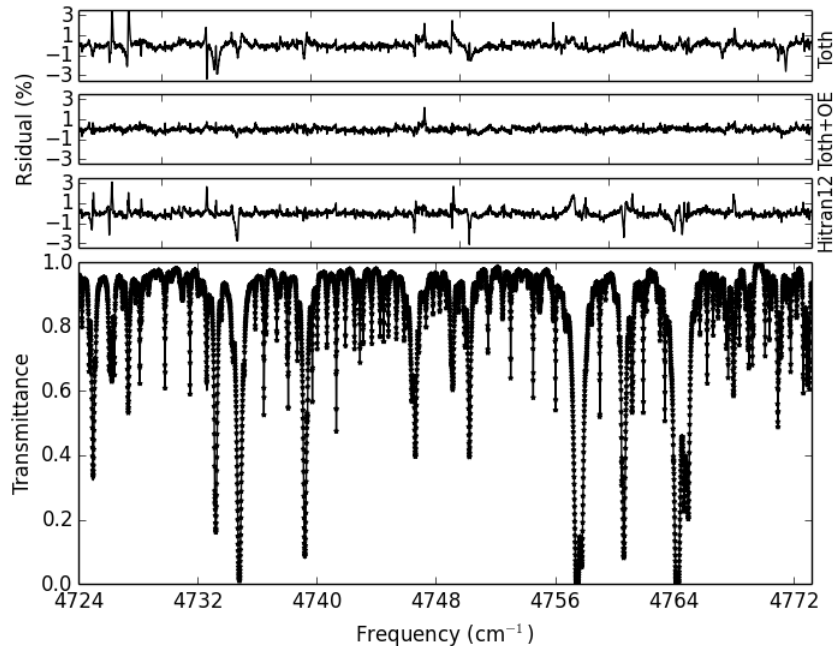


Figure 5.2. Example fit effect using H₂O spectroscopy from Toth (2005) (the first panel), inversion (the second panel), HITRAN 12 (the third panel). The lowest panel gives transmission measured (dot) and calculated (solid line). The spectrum is measured at TCCON site Bremen.

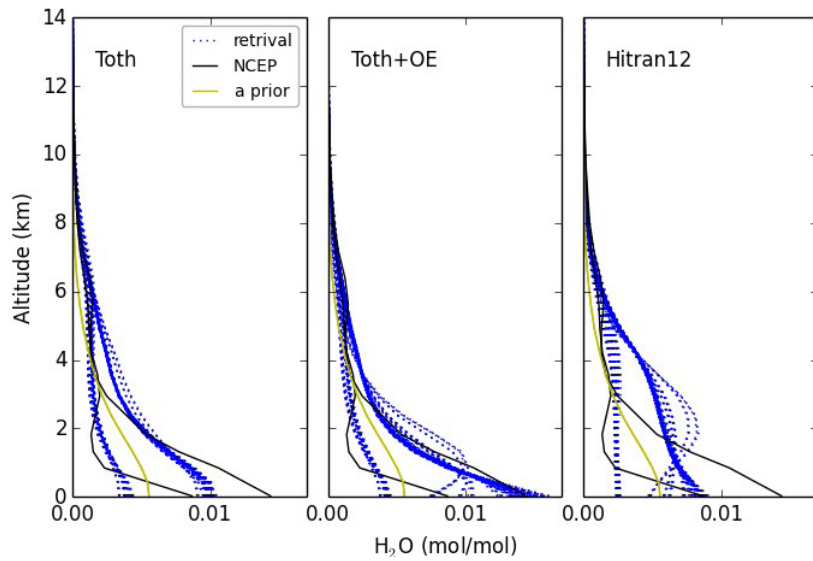


Figure 5.3. Retrieved H_2O profiles (Blue dashed line) from the spectra measured at Bremen using three different spectroscopy, Toth (2005) (left), Inverted (middle) and HITRAN 12 (right). The black line is NCEP daily mean H_2O profile and yellow is a prior.

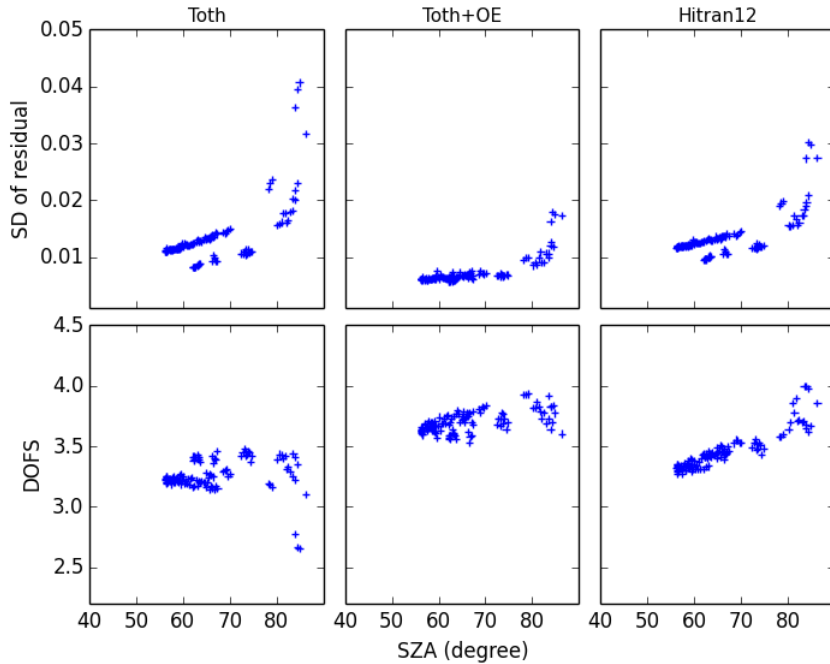


Figure 5.4. Standard deviation (upper panel) of residual and DOFS (lower panel) for the retrieval in Figure 5.3.

The spectra measured at TCCON site Bremen on the days 15 and 01 Oct. 2011 are analyzed with PROFFIT to retrieve H_2O profiles. The same spectral region as that used for inverting H_2O

spectroscopy is used. The considered species are H₂O, N₂O and ¹²CO₂, ¹³CO₂ and all other isotopes of CO₂. A first-order Tikhonov-Phillips constraint is applied for H₂O profile retrieval, which is performed on a logarithmic scale. The profile scaling approach is applied to retrievals of other species, and a prior profiles are GFIT a prior. Three sets of spectroscopy from Toth (2005) (used in GFIT), inversion and HITRAN 12, are compared for H₂O, and only GFIT spectroscopy is used for CO₂ and N₂O. Figure 5.2 shows the residual reduction when using the inverted spectroscopy compared to Toth (2005) and HITRAN 12. Atmospheric temperature and pressure profiles are from NCEP reanalysis data, and intra-day variabilities are allowed. Figure 5.3 and 5.4 show retrieved profiles, the standard deviation of residual and the DOFS. The H₂O profile from Toth (2005) and inverted spectroscopy have better agreement with NCEP profile than HITRAN 12, and the inverted spectroscopy gives a better agreement than Toth (2005) on the humid day. Together with the reduction of residual, the DOFS using the inverted spectroscopy increases. The overestimation of H₂O mole fraction in mid troposphere and underestimation in the boundary layer when using HITRAN 12 could indicate too large air-broaden half width.

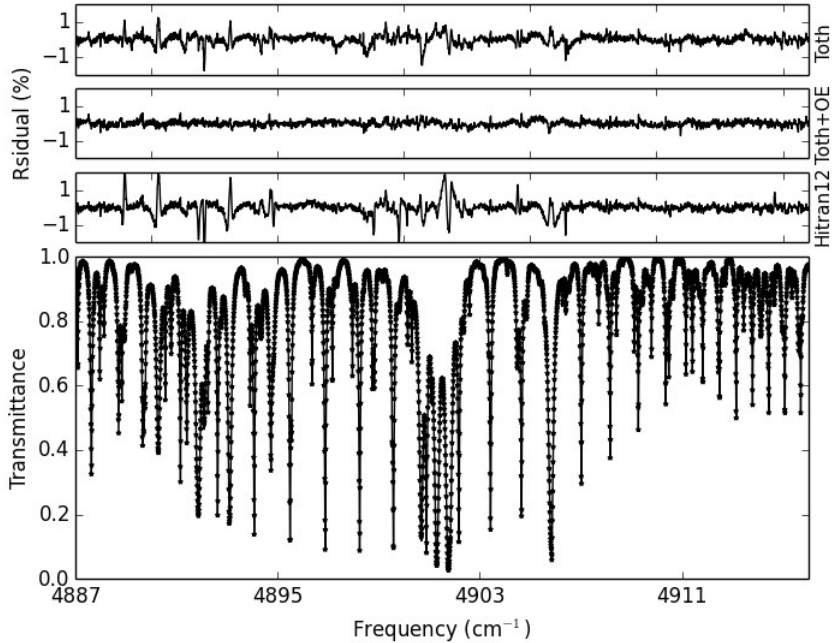


Figure 5.5. Same as for Fig. 5.2 except for a region 4886.70 to 4916.30 cm⁻¹ and that line mixing effect is modeled for CO₂, and there is not N₂O absorption in this region.

The test reveals that the algorithm of inverting H₂O spectroscopy is feasible. It is then applied to the region 4884.50 to 4917.50 cm⁻¹ to reduce residuals from H₂O lines there. Because there is strong CO₂ absorption, the region is split into several smaller windows and the algorithm is applied in each of them separately. Then another algorithm is applied to the whole region to make sure the inversion

for the small windows are consistent with each other. It adjusts intensity scales and vacuum wavenumber shifts only that are shared by all lines within each small window. The other details on the inversion is the same as for the region 4724.40 to 4773.60 cm⁻¹. Figure 5.5 gives a comparison between different sets of H₂O spectroscopy, the inverted one reduces residual compared to Toth (2005) and HITRAN 12.

5.2.3. Solar line

The solar spectrum is not a smooth blackbody spectrum, in contrast, there are a lot of absorption features on it resulted from the solar photosphere. They should be taken into account in analysis of ground-based spectra. The absorption species include molecules CO, OH and CN etc., and atoms Fe, Si, Mg and C etc. A solar line contains absorptions occurring in a depth of the solar photosphere where both pressure and temperature vary considerably. Summation of these absorptions can result in various line shapes. The solar rotation leads to Doppler-broadening in observed solar line if the field view covers a part only of solar disk. The width and strength of solar lines change with respect to the projected distance from the solar disk center. Accounting for all these effects, Hase et al. (2006) give an empirical line shape model and corresponding database in the infrared region. Line shape model is expressed as,

$$I(\Delta\sigma) = A \exp\left(\frac{-(\Delta\sigma)^2}{\sqrt{b^4 + w(-0.54b^4 + 0.33b^3|\Delta\sigma| + 0.12b^2(\Delta\sigma)^2 + 0.342b|\Delta\sigma|^3)}}\right),$$

where A is the amplitude, $b/\ln 2$ is the half width at half maximum, $\Delta\sigma$ is the distance from line center measured in wavenumber (cm⁻¹). w is a parameter adjusting line shape, which is Gaussian ($w=0$), Lorentzian ($w=1$) and cusp-shaped ($1 < w \leq 1.85$). In addition, the line parameters A and b are allowed to vary as a function of projected solar disk radius ρ for describing the center-limb variation of line width and strength, $A(\rho)=A(0)(1+V_A\rho^2)$, $b(\rho)=b(0)(1+V_b\rho^2)$, $0 \leq \rho \leq 1$.

The line-by-line model of solar line is used in the forward model of PROFFIT. However, the line parameters are not accurate enough in the region 6180.00 to 6260.00 cm⁻¹ where a strong CO₂ band exists that is used to retrieve ¹²CO₂ in this Chapter. To reduce residuals from solar line, a set of ground-based spectra is used to improve the line parameters based on OE theory. The spectra are measured at TCCON site Bialystok, under lower SZA and dry air condition. All lines with strength larger than 1.0×10^{-2} are inverted, in which six parameters, center wavenumber, A , b , w , V_A and V_b , are adjusted for lines stronger than 5.0×10^{-1} , only the first four for lines stronger than 5.0×10^{-2} and only the first three for other lines. A prior is just taken as the database used by PROFFIT (Hase et al., 2006), uncertainties are estimated as 0.01 cm⁻¹ for center wavenumber, 25% for A , 40% for b and w , 40% and 50% for V_A and V_b respectively. And the allowed minimum uncertainties for the last five parameters are 1.0×10^{-4} , 1.0×10^{-2} cm⁻¹, 1.0×10^{-2} , 5.0×10^{-3} and 5.0×10^{-3} . The PROFFIT is executed to fit the spectra, and considered species are CO₂, H₂O, and CH₄.

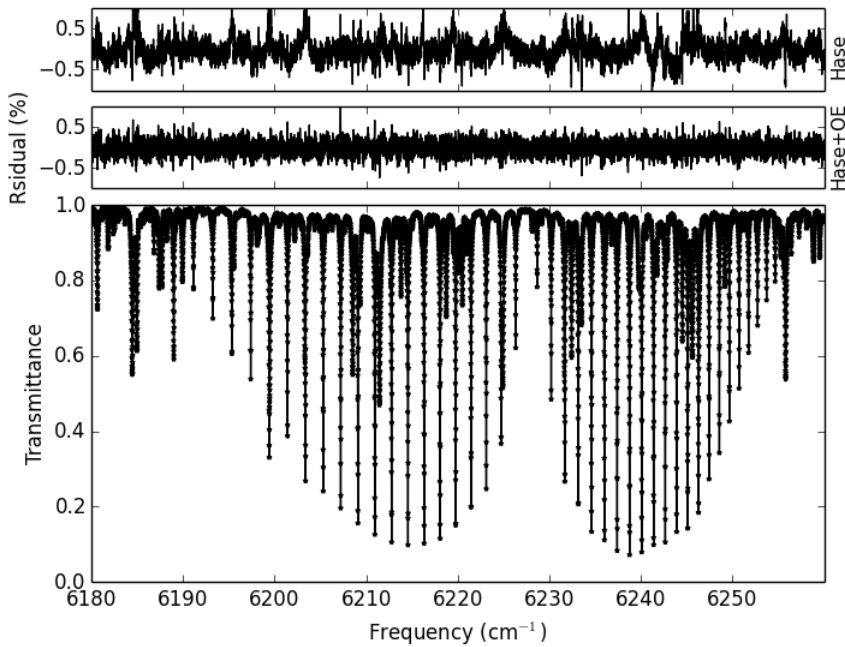


Figure 5.6. Example fit effect using solar line database of PROFFIT (the first panel) and from inversion (the second panel). The lowest panel gives transmission measured (dot) and calculated (solid line). The spectrum is measured at TCCON site Bialystok.

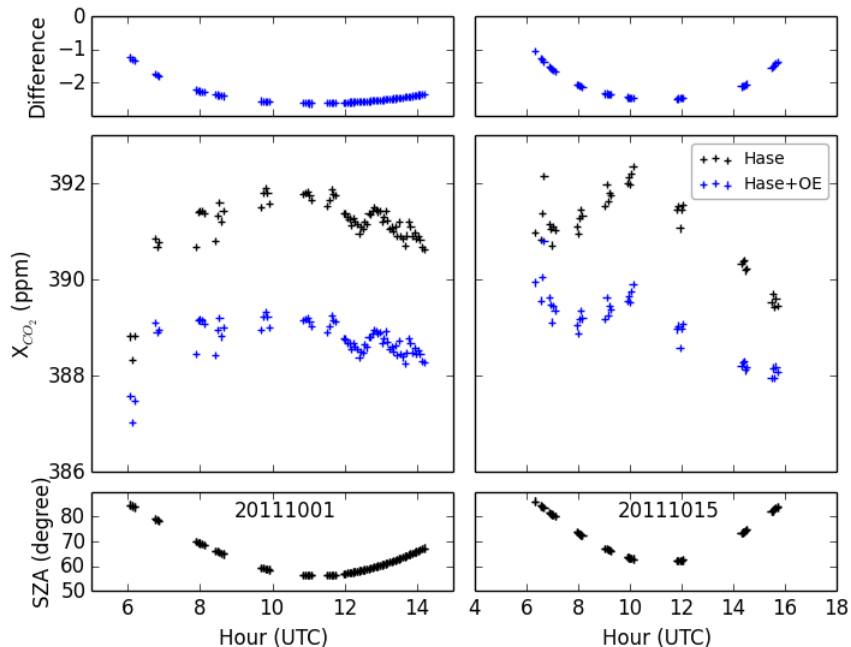


Figure 5.7. CO₂ column-averaged mole fraction retrieved from spectra measured at Bremen using solar line database of PROFFIT (black) and that inverted (blue). The first panel is difference, the second CO₂ mole fraction, the third SZA. Air column is derived from surface pressure.

CO_2 spectroscopy is from Toth (2008a) (used in GFIT) with an addition of line mixing parameter of PROFFIT, which is calculated using the software (Lamouroux et al., 2010), H_2O from Toth (2005) and CH_4 from HITRAN 12. Profiles are adjusted with the first-order Tikhonov-Phillips constraint for CO_2 and GFIT a prior is scaled for others. In the case where adjusting line parameters can not reduce residual to a required level, the solar line will be split into several lines. Figure 5.6 shows a reduction of residual by using the inverted solar line parameter. The spectra measured at Bremen are used to test influences of solar line parameter on retrieval of CO_2 in this region. The retrieval is done with PROFFIT, considered species are $^{12}\text{CO}_2$, other isotopes of CO_2 , CH_4 and H_2O . The used spectroscopy is the same as that used in inverting solar line parameters, except for only Toth (2008) is used for CO_2 without line mixing taken into account. GFIT a priors are scaled for retrievals of all species. T_p is from NCEP reanalysis and intra-day variabilities are included. As can be seen from Figure 5.7, inverted solar line parameters reduce CO_2 column by about 2 ppm and the airmass-dependence by 2 ppm. This reduction could be similar for all measurements, except for the high-altitude site. Because the influence of solar lines does not depend on atmospheric state except for CO_2 concentration, which is quite uniform globally.

This algorithm is also applied to the region 4887.00 to 4916.00 cm^{-1} , however, solar line is weak there, reduction of residual is small and will not shown here.

5.2.4. CO_2

The majority of CO_2 spectroscopy is given assuming a Voigt line shape (Toth et al., 2008a), and a few studies consider line mixing and speed-dependence effect in limited regions (Devi et al., 2007; Predoi-Cross et al., 2007; Miller et al., 2005). A theoretical method is developed to predict line mixing of CO_2 in Lamouroux et al. (2010), which is applied to all CO_2 lines. There are a lot of work contributing to measurement of all relevant line parameters for the main isotope $^{12}\text{CO}_2$ lines, such as the region 6180.00 to 6260.00. However, the measurements for minor isotopes, such as $^{13}\text{CO}_2$ band used in this Chapter in the region 4887.00 to 4916.00, are limited to vacuum wavenumber and intensity only (Miller et al., 2004; Toth et al., 2008b). The other parameters of $^{13}\text{CO}_2$ lines are predicted with theory.

The CO_2 line parameters in the regions around 6220 and 4901 cm^{-1} are inverted from ground-based solar spectra measured at TCCON site Bialystok, totally 14 records the SZA of which range from 30° to 82° . The code PROFFIT is executed to fit the spectra. For the $^{12}\text{CO}_2$ region 6180.00 to 6260.00 cm^{-1} , considered species are $^{12}\text{CO}_2$, other isotopes of CO_2 , H_2O , HDO and CH_4 . The used spectroscopy database are Toth et al. (2008a) with addition of line mixing parameter of PROFFIT for CO_2 that acts as a prior spectroscopy in inverting line parameter step, Toth (2005) for H_2O and HDO and HITRAN 12 for CH_4 . Profile retrieval under the first-order Tikhonov-Phillips constraint is applied to $^{12}\text{CO}_2$, and scaling GFIT a prior is used for other species. For $^{13}\text{CO}_2$ region 4886.70 to 4916.30 cm^{-1} , considered species are H_2O , $^{12}\text{CO}_2$, $^{13}\text{CO}_2$, CO^{18}O and other isotopes of CO_2 . The used spectroscopy database is the inverted one for H_2O , and the same as in $^{12}\text{CO}_2$ region for CO_2 . The inverted solar line parameters are used for both regions. Profile retrievals with the first-order

Tikhonov-Phillips constraint are performed for H₂O on a logarithmic scale, and for CO₂ on a linear scale. For the profile retrieval in both regions, a prior is from WACCM climatology for H₂O, and a mean profile of CarbonTracker for CO₂ at Bialystok. The channeling is considered in both regions, and Tp profiles are from NCEP reanalysis with intra-day variability allowed.

Spectroscopy parameter inversions with and without speed-dependence of air-broadening effect taken into account are performed, and both of which with line mixing taken into account. Spectroscopy of lines with intensity larger than $1.0 \times 10^{-24} \text{ cm}^{-1}$ only are inverted and involved parameters are intensity S and air-broaden half width γ_{air} at 296 K, first-order line mixing coefficient at 260 K Y_{260} . In the case that the speed-dependence parameter of air broadening γ_2 at 296 K is inverted, it is adjusted for lines stronger than 3.0×10^{-24} only. A prior of the speed-dependent parameter is taken as zero. The uncertainty of the line mixing coefficient is set to be 0.0035 atm^{-1} , and that of the speed-dependent parameter $0.01 \text{ cm}^{-1}\text{atm}^{-1}$. A smooth constraint for variations along m is applied for the speed-dependent parameter. J'' is rotational quantum number of lower states.

Figure 5.8 and 5.9 give an example for fitting effect using different sets of spectroscopy for CO₂ in both regions. It can be seen that inverted line parameters reduce the residual. Taking speed-dependence of air-broadening into account does not improve the fit any further.

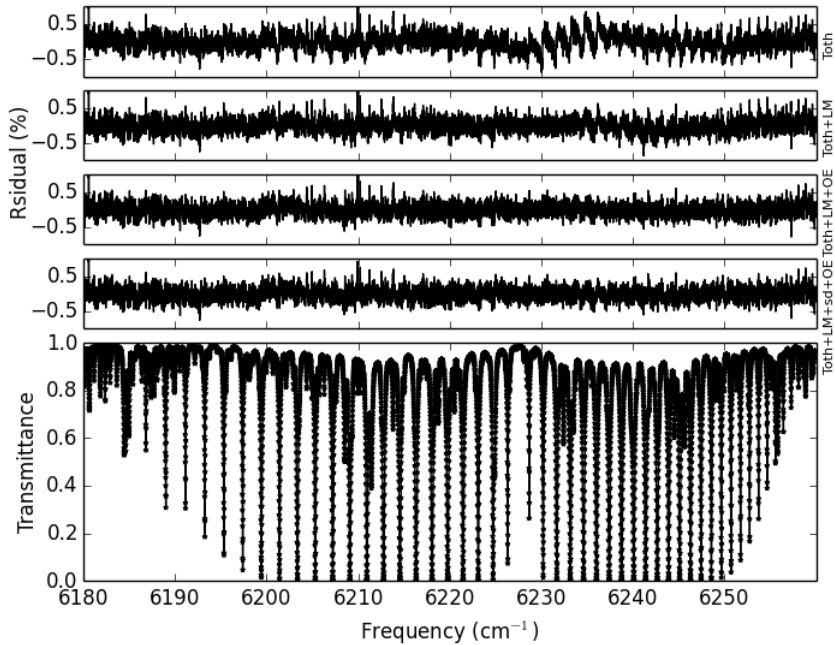


Figure 5.8. residual variations when using different spectroscopy, Toth (2008a) (the first panel), Toth (2008a) with line mixing (the second panel), optimized Toth (2008a) with line mixing (the third panel) and optimized Toth (2008a) with line mixing and speed-dependence of air-broadening effect (the fourth panel), for CO₂ in region 6180–6260 cm^{-1} . The lowest panel give transmission, the spectrum is measured at Bialystok under a SZA of 81.7°.

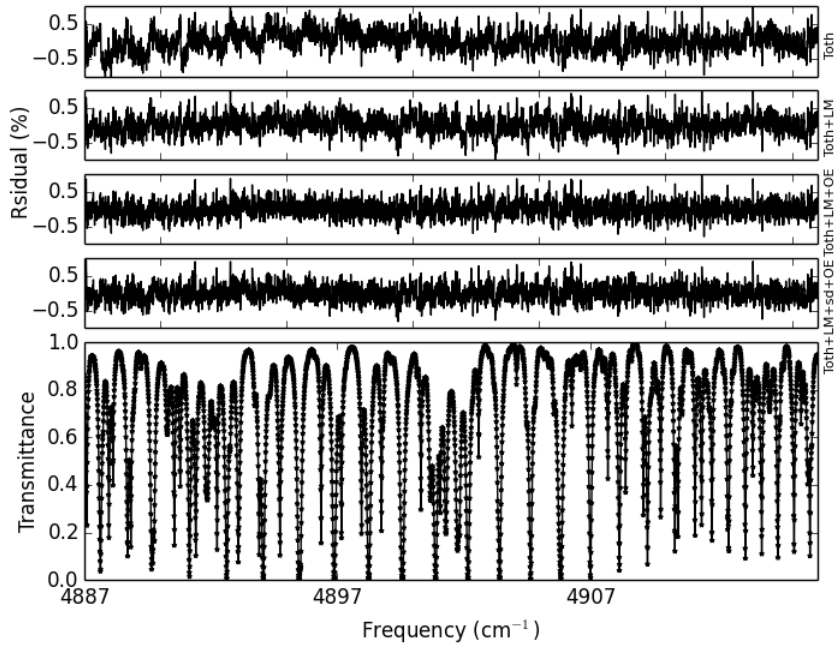


Figure 5.9. Same as Fig. 5.8 except for region 4887-4916 cm^{-1} .

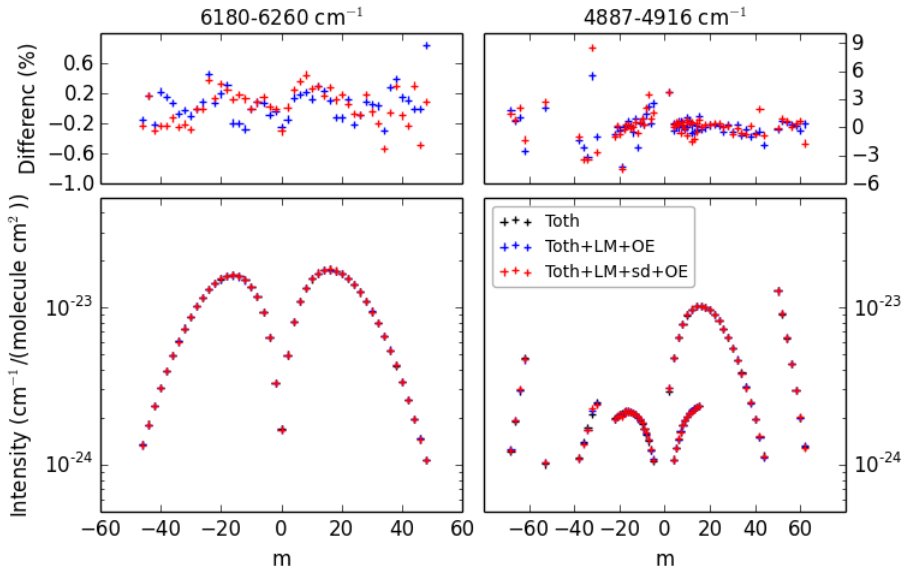


Figure 5.10. Comparison of intensities at 296 K of CO_2 lines in regions 6180-6260 cm^{-1} (left) and 4887-4916 cm^{-1} between Toth (2008a) (black), optimized with line mixing (blue) and both line mixing and speed-dependence of air-broadening (red) taken into account. The first panel give percent differences and the second absolute value.

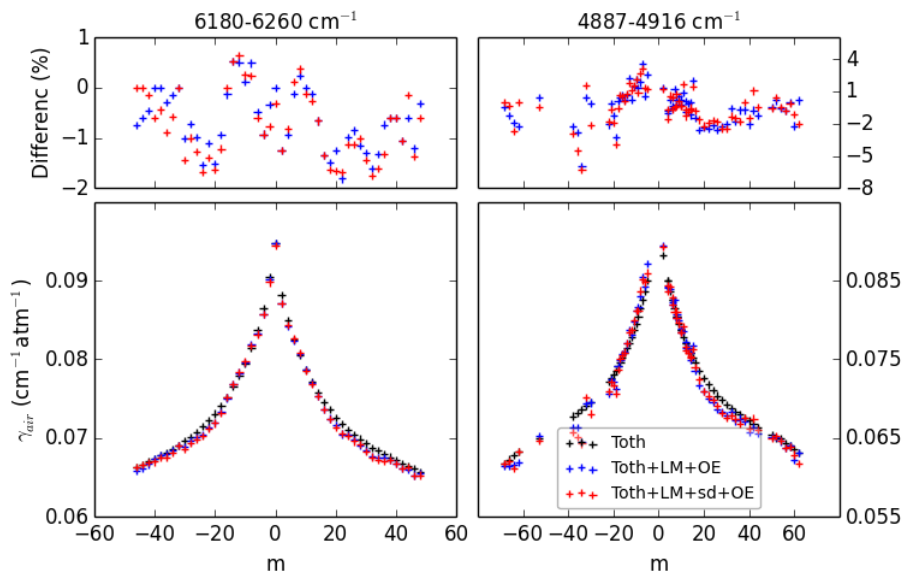


Figure 5.11. Same as Fig. 5.10 except for air-broaden half width at 296 K, γ_{air} .

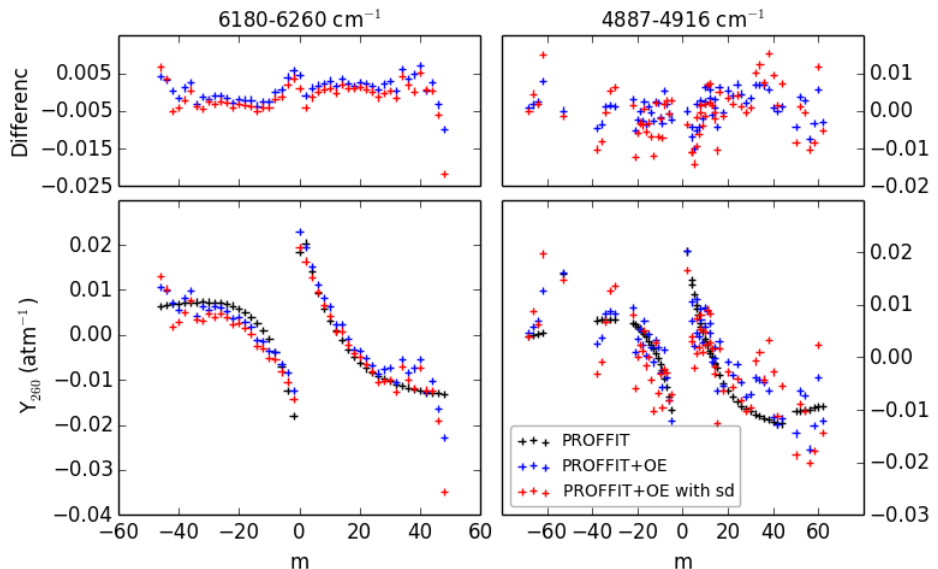


Figure 5.12. Same as Figure 5.10 except for the first-order line mixing coefficient at 260 K, Y_{260} .

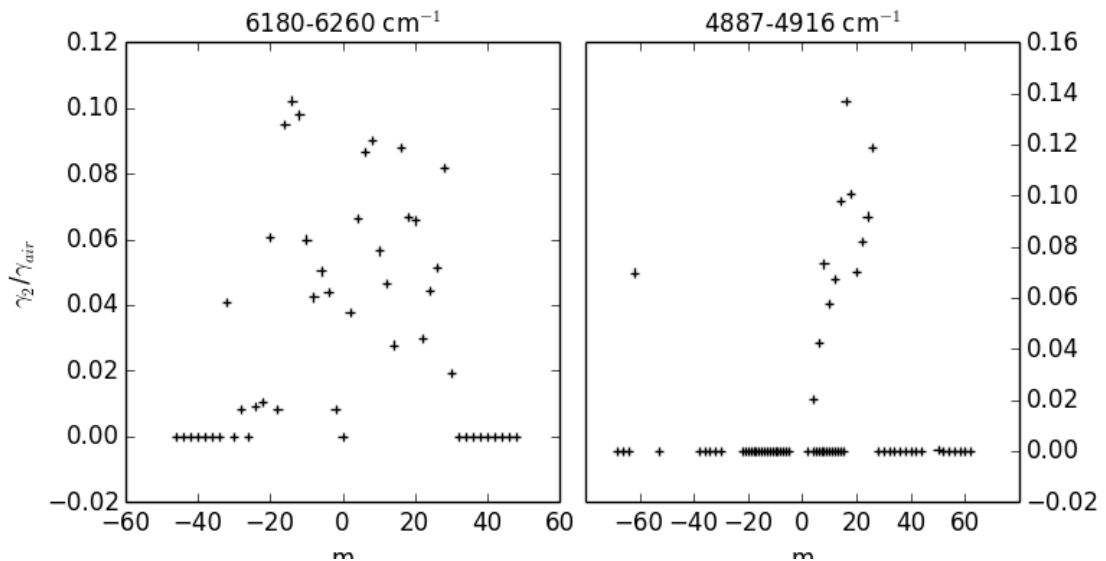


Figure 5.13. Inverted speed-dependence parameter for air-broadening at 296 K, γ_2 .

The comparisons between the inverted and a prior line parameters of CO_2 in both regions are given in Figure 5.10-5.13. The differences of S , γ_{air} and Y_{260} between inversions and a prior are smaller in region $6180\text{-}6260\text{ cm}^{-1}$ than $4887\text{-}4916\text{ cm}^{-1}$. It reflects that there is a lot of laboratory measurements in the first region and then the uncertainties of S and γ_{air} given in HITRAN are smaller than that in the second region. The larger difference and scatter of Y_{260} in the region $4887\text{-}4916\text{ cm}^{-1}$ could come from a strong interference between different isotopes of CO_2 or weaker line mixing effect due to smaller line strength. The absorption of CO_2 in region $6180\text{-}6260\text{ cm}^{-1}$ is almost completely from a $^{12}\text{CO}_2$ band $30013\leftarrow 00001$ and each line locates distinct from the others. In both regions, the inverted γ_{air} is smaller than a prior around $|m|=20$, which exists for both inversions with and without speed-dependence parameter taken into account. It is not clear whether the laboratory or atmospheric measurement is closer to the true value. The inverted speed-dependence parameter only differs from a prior (zero) for strong lines, and presents large scatter. It indicates information about this parameter is rare in the current set of spectra. If additional spectra measured at high-altitude sites are included, the information on speed-dependence of air-broadening effect could be improved.

The measurements at Bremen are used to test influences of different spectroscopies on the retrieval of CO_2 . The retrieval is done with PROFFIT and its setup is same as for inverting CO_2 spectroscopy except for that scaling GFIT a prior and a profile retrieval based on the optimal estimation theory, which will be detailed in Sect. 5.3.2, are applied to CO_2 . In region $4887\text{-}4916\text{ cm}^{-1}$, only scaling GFIT a prior is used for CO_2 isotopes other than $^{13}\text{CO}_2$. The channeling is not taken into account. There are four sets of line parameters compared for CO_2 , which are Toth (2008a), Toth (2008a) with line mixing parameters of PROFFIT, the optimized Toth (2008a) and line mixing parameters, and the optimized Toth (2008a) with line mixing and speed-dependent parameters together. Figure 5.14

shows variations of CO₂ columns resulted from using different spectroscopies for CO₂. The inverted line parameter reduces airmass-dependence of ¹³CO₂ columns by about 5 ppm, and about 1-2 ppm for ¹²CO₂ on these two days. Including speed-dependence parameter only create positive shift than without it, which is 0.5-1 ppm at SAZ above 80°. Addition of line mixing parameters has negligible influence without an optimization applied. Figure 5.15 presents variations of $\delta^{13}C$, reduction of its airmass-dependence by using the optimized spectroscopy of CO₂ is about 7 with a slight better performance from including both line mixing and speed-dependence of air-broadening effect.

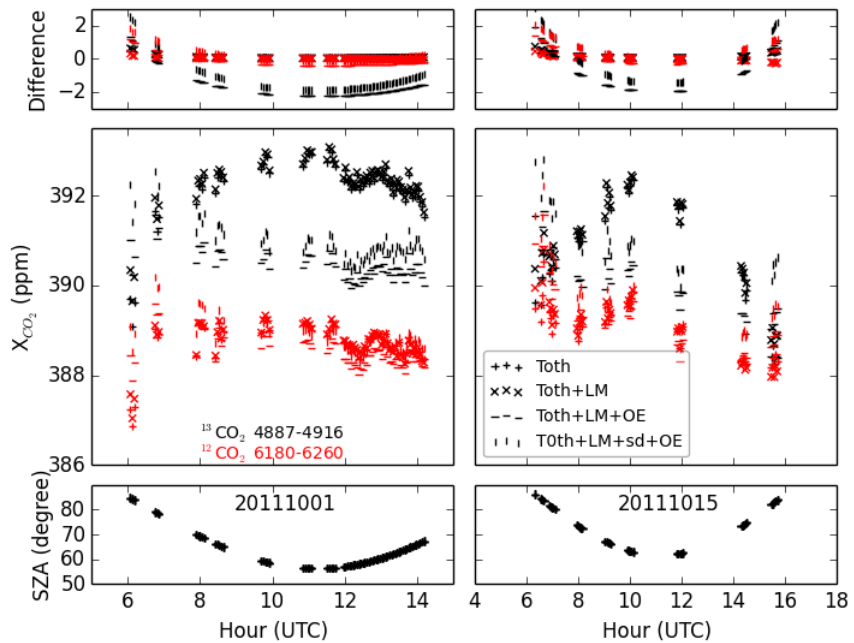


Figure 5.14. Comparison of column-averaged ¹²CO₂ (red) and ¹³CO₂ (black) mole fractions retrieved from two days measurements at Bremen using different spectroscopy, Toth (2008a) (plus), Toth (2008a) with line mixing parameter (cross), optimized with line mixing (horizontal line) and both line mixing and speed-dependence of air-broadening (vertical line) taken into account. The first panel is difference, the second CO₂ mole fraction and the third SZA. Surface pressure is used to calculate air column.

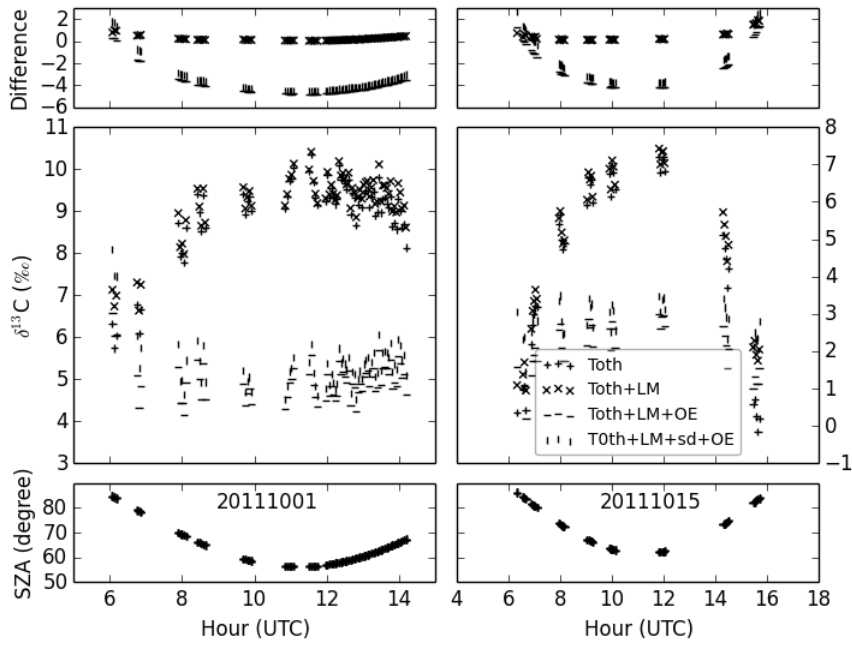


Figure 5.15. Same as Fig. 5.14 except for $\delta^{13}\text{C}$.

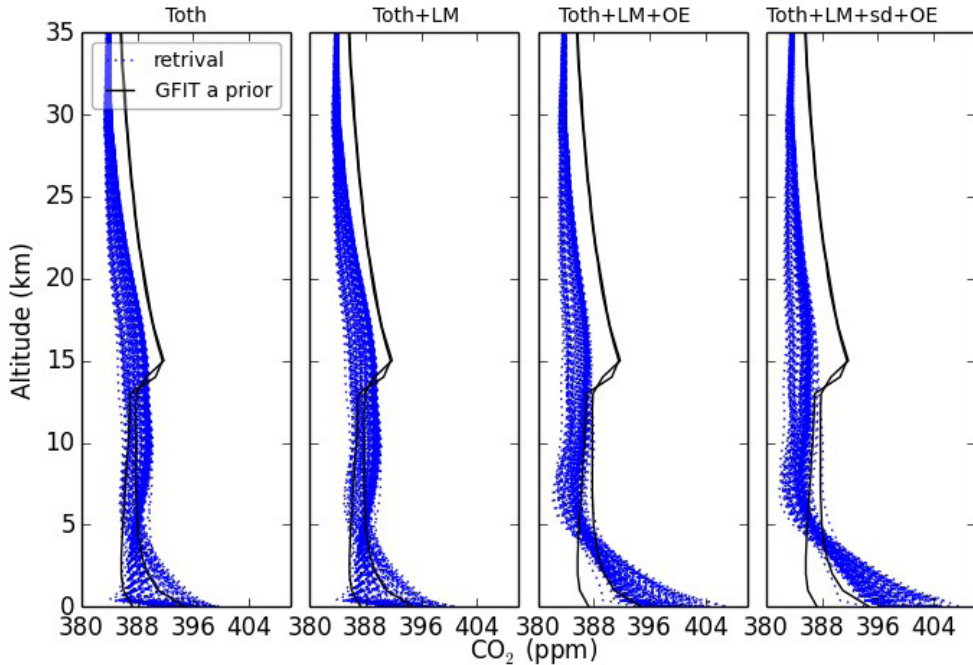


Figure 5.16. Comparison of $^{12}\text{CO}_2$ profiles retrieved from two days measurements at Bremen using different spectroscopy, Toth (2008a) (the first panel from the left), Toth (2008a) with line mixing parameter (the second panel from the left), optimized with line mixing (the third panel from the left) and both line mixing and speed-dependence of air-broadening (the fourth panel from the left) taken into account. The blue line is the retrieval and black is GFIT a prior.

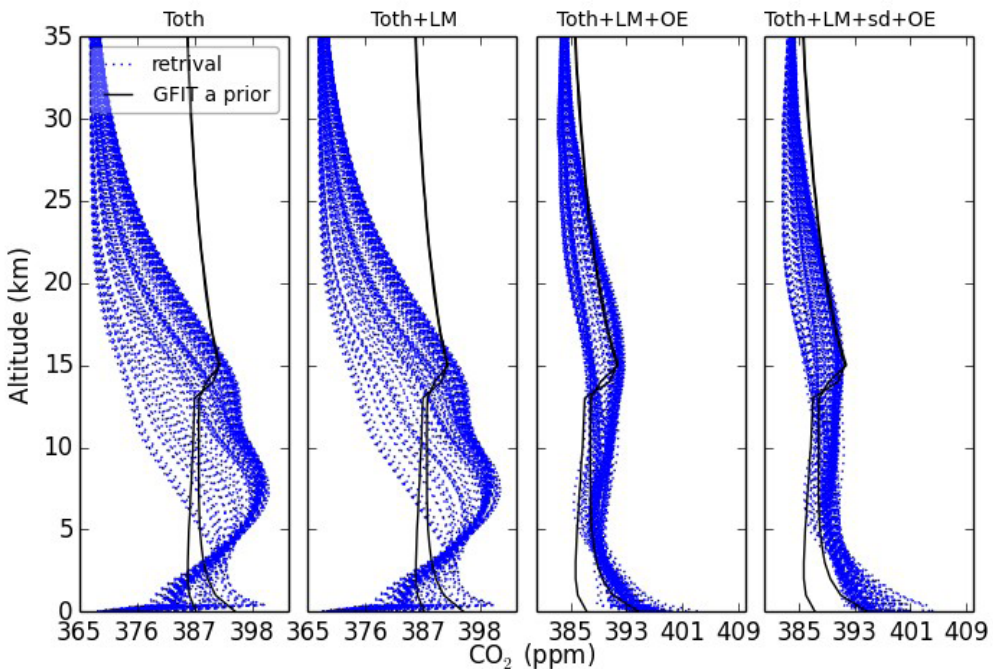


Figure 5.17. Same as Fig. 5.16 except for $^{13}\text{CO}_2$ profiles. Note a different x axis scale is used for the first two panels from the left.

Figure 5.16 and 5.17 show variations of retrieved $^{12}\text{CO}_2$ and $^{13}\text{CO}_2$ profiles using different spectroscopies. The inverted spectroscopy largely improves $^{13}\text{CO}_2$ profiles, by increasing mole fractions in the stratosphere and lower troposphere and deceasing them in the mid and upper troposphere, which indicates an overestimation of γ_{air} in Toth (2008a). However, it is hard to say if $^{12}\text{CO}_2$ profiles are improved or degraded. Including speed-dependence effect increases mole fractions in the boundary layer, because the air-broaden half width averaged over the thermal distribution of molecular speed is smaller than that at the mean speed (Hartmann et al., 2008, p.92).

5.3. Retrieval aspect

The column of CO_2 could differ among different retrieval setups, e.g. profile scaling or a profile retrieval is applied to CO_2 itself; treatment of interference species, like H_2O ; Tp profiles, e.g. use NCEP reanalysis or retrieve them simultaneously.

5.3.1. Influence of Interference species

The only important inference species is H_2O in region $4887\text{-}4916 \text{ cm}^{-1}$ for $^{13}\text{CO}_2$ retrieval. The influence of H_2O depends on its concentration and vertical distribution, which can be retrieved through scaling a profile, e.g. that from NCEP reanalysis, or adjusting its profile. In addition, the accuracy of H_2O spectroscopy could matter as well.

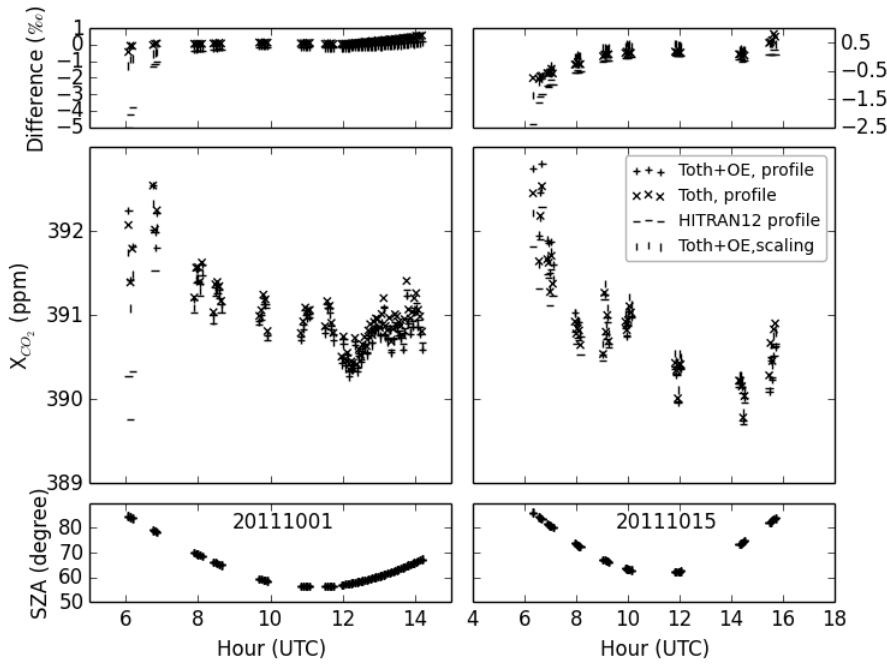


Figure 5.18. Variations of $^{13}\text{CO}_2$ column using different setups for fitting H_2O , using optimized Toth (2005) line parameter and adjusting profile (plus), using Toth (2005) line parameter and adjusting profile (cross), using HITRAN 12 line parameter and adjusting profile (horizontal line), using optimized Toth (2005) line parameter and scaling (vertical line) GFIT a prior. In all cases, $^{13}\text{CO}_2$ is retrieved thorough scaling GFIT a prior and using the optimized Toth (2008a) with both line mixing and speed-dependence of air-broadening taken into account.

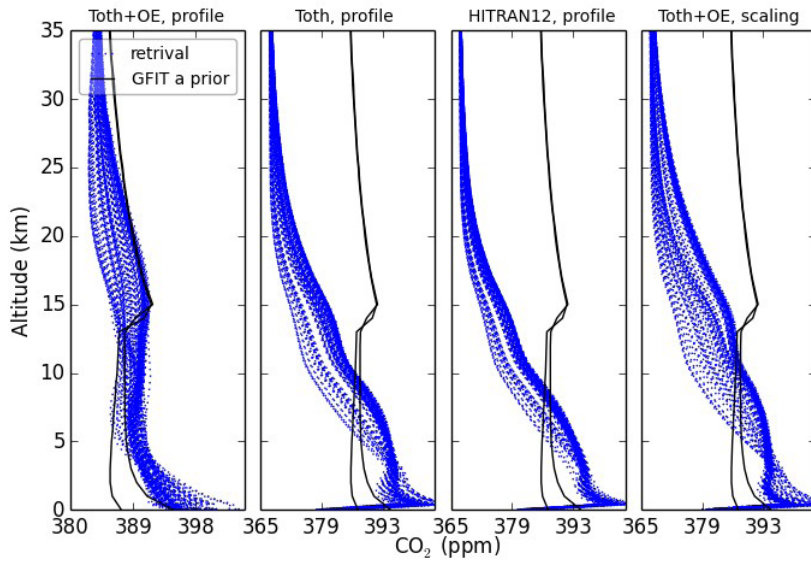


Figure 5.19. The $^{13}\text{CO}_2$ profiles, which are retrieved using optimal estimation approach, under various H_2O fitting setups as in Fig. 5.18. Note a different x axis scale is used for the first panel from the left.

Figure 5.18 and 5.19 show influences of H₂O retrieval setups on the retrieval of ¹³CO₂ columns and profiles for the two days measurements at Bremen. Four setups are compared, which are using optimized Toth (2005) line parameters and adjusting H₂O profiles under the first-order Tikhonov-Phillips constraint, as the former except for using Toth (2005) line parameters, as the first except for using HITRAN 12 and using optimized Toth (2005) line parameters but scaling GFIT a prior to fit H₂O absorption. The ¹³CO₂ column and profile are retrieved by scaling GFIT a prior for retrieving columns, and using optimal estimation approach for retrieving profiles, respectively. The CO₂ spectroscopy is the optimized Toth (2008) including line mixing and speed-dependence effect of air-broadening. Other details are the same as in Sect. 5.2.4.

Comparing with the first setup of H₂O retrieval, using HITRAN 12 leads to the largest difference as expected because the large residuals resulted from it. The second largest difference is from using the profile scaling, up to 2‰. An interesting thing is that the difference from applying the profile scaling is larger for a day with less humidity. It could indicate an importance of adjusting H₂O profile for in a retrieval of $\delta^{13}\text{C}$. Using H₂O spectroscopy that is not optimized creates the smallest difference, about 1‰. However, the conclusion might not be general since only two days measurements are used. The influence of H₂O on retrieved ¹³CO₂ profiles is much more significant, the variation is up to 20 ppm in the stratosphere. Because stratospheric CO₂ is known quite well, as shown by the GFIT a prior, the results using the first setup for H₂O should be the closest to true profiles.

5.3.2. Influence of retrieval method

The column averaging kernels of ¹³CO₂ and ¹²CO₂ should be similar as much as possible for a correct retrieval of their ratio. The stronger a CO₂ line is, the larger the weight of a retrieval in lower atmosphere is. The retrieval with more DOFS has vertically uniformer column sensitivity, e.g. a profile retrieval compared to a profile scaling approach. In this section, two retrieval strategies are compared for CO₂, scaling GFIT a prior and profile retrieval using the optimal estimation theory.

A prior covariance of CO₂ is constructed empirically, with diagonal elements derived from CarbonTracker simulations implemented by WACCM in upper atmosphere. Off-diagonal elements are calculated as $S_{a,ij} = \sigma_i \sigma_j \exp[-(z_i - z_j)^2/l^2]$, where σ is the square root of the diagonal elements and z_i is the altitude of the i th grid on which CO₂ profiles are sampled, $l=3\text{ km}$. A prior profile is the average of the merged model profiles, which is scaled to follow interannual increase of atmospheric CO₂. The DOFS is about 1-2 for both ¹²CO₂ and ¹³CO₂. The used spectroscopy is, optimized Toth (2008a) added with line mixing and speed-dependence of air-broadening for CO₂, the optimized Toth (2005) for H₂O. Profile retrieval and scaling are used for H₂O in regions 4887-4916 cm⁻¹ and 6180-6260 cm⁻¹, respectively. Other aspects of setups in both the regions are the same as in the former sections.

Figure 5.20 shows the correlation matrix $r_{ij} = \exp[-(z_i - z_j)^2/l^2]$ and a prior profile of CO₂. The CO₂

mole fraction at the lowest layer is assumed to be uncorrelated with that at other layers, since there are a lot of small-scale variations in the boundary layer. Figure 5.12 presents column averaging kernels of CO₂ in both regions. It is clear that the column averaging kernel for profile retrieval has less a difference between the two regions, and variabilities with SZA.

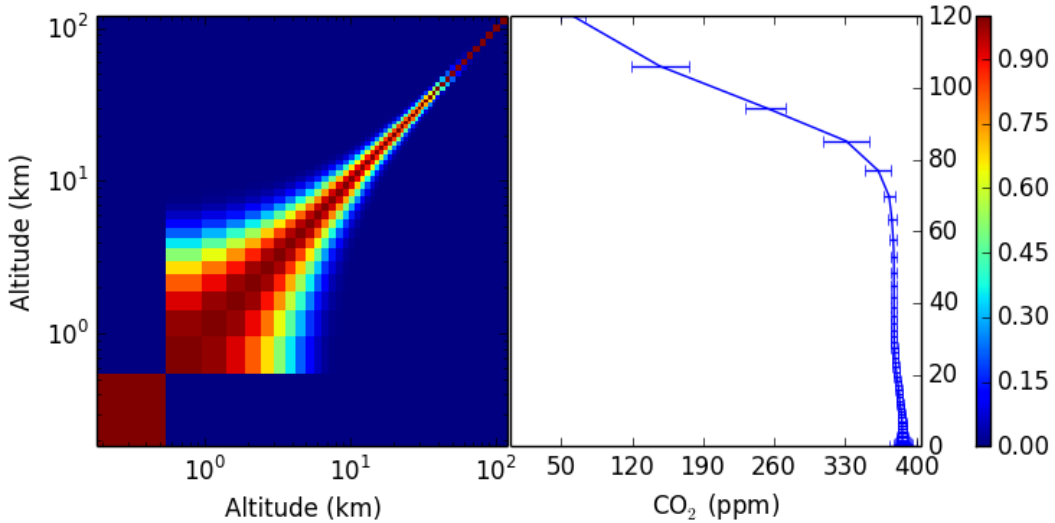


Figure 5.20. Correlation matrix of a prior covariance $r_{ij} = S_{a,ij}/(\sigma_i \sigma_j)$ (left) and a prior profile with square root of diagonal elements of a prior covariance represented by the error bar (right).

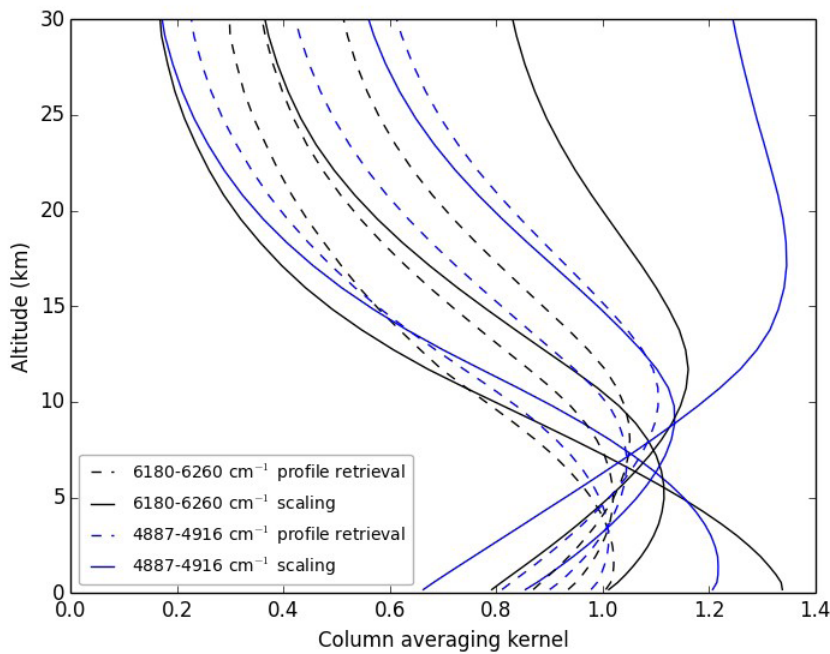


Figure 5.21. Column averaging kernels of CO₂ retrieval for region 6180-6260 cm⁻¹ (black) and 4887-4916 cm⁻¹ (blue) using profile retrieval (solid line) and scaling (dashed line). The kernels are

from three example spectra measured at Bialystok and with SZA of 30°, 70° and 81°.

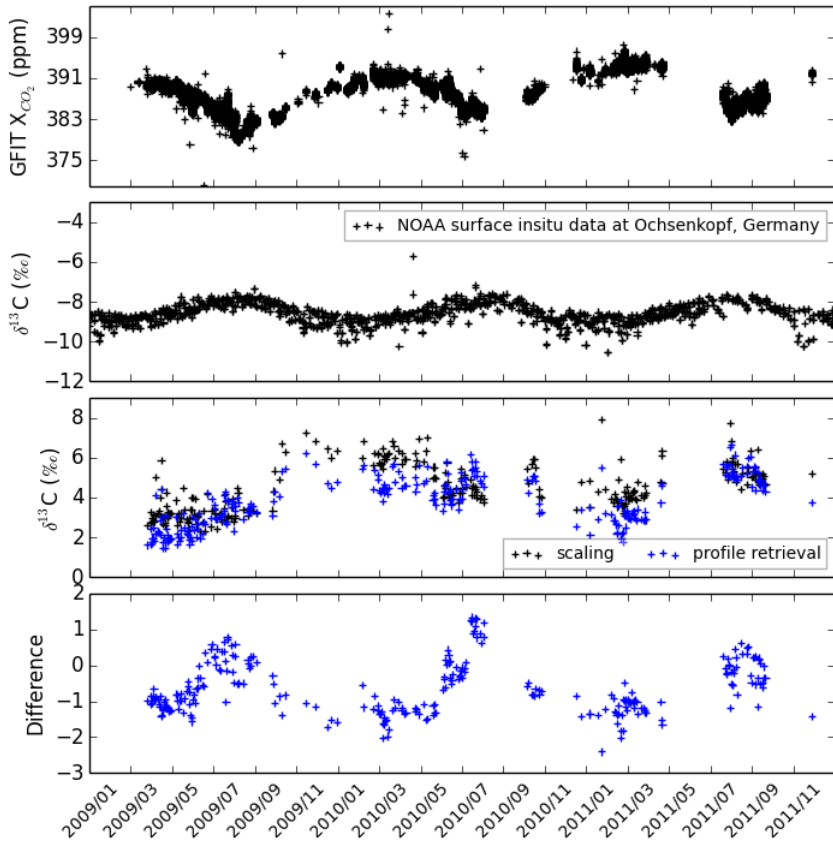


Figure 5.22. Daily mean of retrieved $\delta^{13}C$ from spectra measured at Bialystok in the period 2009-2011 through scaling GFIT a prior (the third panel, black) and profile retrieval (the third panel blue) for fitting CO₂, and the difference between them (the fourth panel). The together showed are GFIT X_{CO_2} (the first panel), NOAA surface $\delta^{13}C$ (the second panel) measured at Ochsenkopf (50.030°N, 11.808°E, 1009 masl), Germany.

Near-infrared spectra measured at Bialystok during 2009-2011 are used to test the two methods of retrieving CO₂, and the results are showed in Figure 5.22. The difference of $\delta^{13}C$ between the two methods presents a seasonal behavior in a range of -2 to 1, because the influence of the averaging kernel depends on CO₂ profiles that vary seasonally. The seasonal cycles of $\delta^{13}C$ from FTS are similar to that of in situ measurements. Mole fractions of CO₂ peak and $\delta^{13}C$ reaches minima in winter because of a release of CO₂ by the respiration of the plants which is enriched in ¹²C relative to atmospheric CO₂. The opposite occurs in summer because the plants fix CO₂, with a preference to ¹²CO₂. However, disagreements occur in the period August of 2009 to March of 2010. The FTS was not evacuated in that period, one of its effects is scaling the measured frequency by a factor that

depends the refractive index of air at that frequency and the laser frequency of a FTS. However, applying a calibration to the measured frequency did not produce any significant difference.

5.3.3. Influence of atmospheric T, P profiles

In all the former setups of CO_2 retrievals, Tp profiles are from NCEP reanalysis data. However, it is also possible to retrieve atmospheric temperature from the spectra, and pressure can be calculated based on the barometric formula given surface pressure. The strength of a molecular absorption line is related to the equilibrium relative population of the initial state, as showed in Eq. 5.7, which can be expressed as $\rho \propto \exp(-E/k_B T)$, where E is the initial state energy. The lines with different initial states will differ in the temperature-dependence of their strength. Atmospheric temperature can be retrieved based on such dependence.

In this section, retrievals with and without fitting temperature are compared. The profile retrieval based on optimal estimation is applied to both $^{13}\text{CO}_2$ and $^{12}\text{CO}_2$, used spectroscopy databases and other details are the same as in Sect. 5.3.2. While the same region 4887-4916 cm^{-1} is used for $^{13}\text{CO}_2$ and temperature retrieval, there are additional microwindows, where H_2O lines with various initial state energies present, used except for the region 6180-6260 cm^{-1} to improve information on temperature in the case of $^{12}\text{CO}_2$. These windows are 4724.00-4728.30, 4732.30-4736.50, 4738.70-4740.70, 4750.00-4751.50 and 4755.70-4766.40 cm^{-1} . The optimized Toth (2005) is used for H_2O , and a profile retrieval is applied to it. Temperature profiles are retrieved based on an optimal estimation approach in both regions.

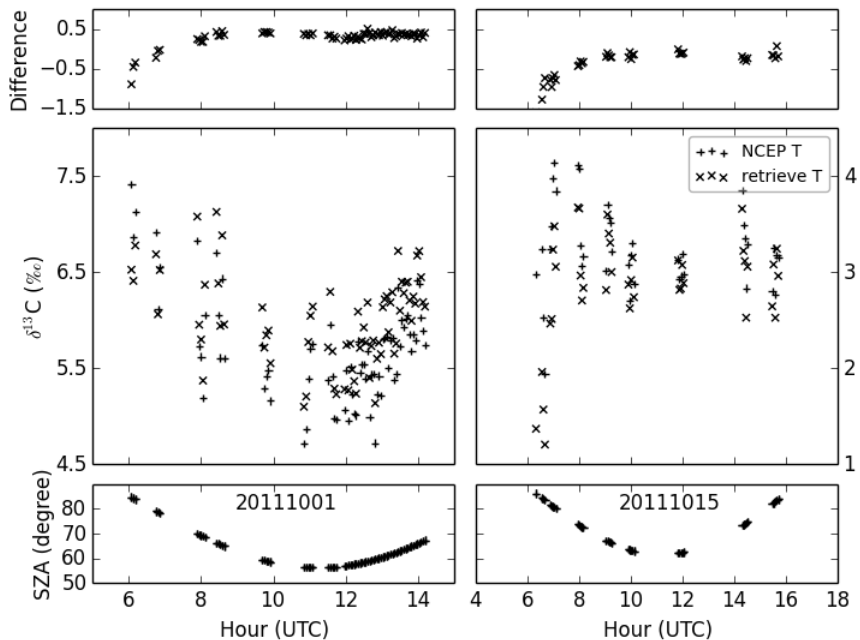


Figure 5.23. Comparison of $\delta^{13}\text{C}$ between with (cross) and without (plus) fitting temperature. The

spectra are measured at Bremen on two days.

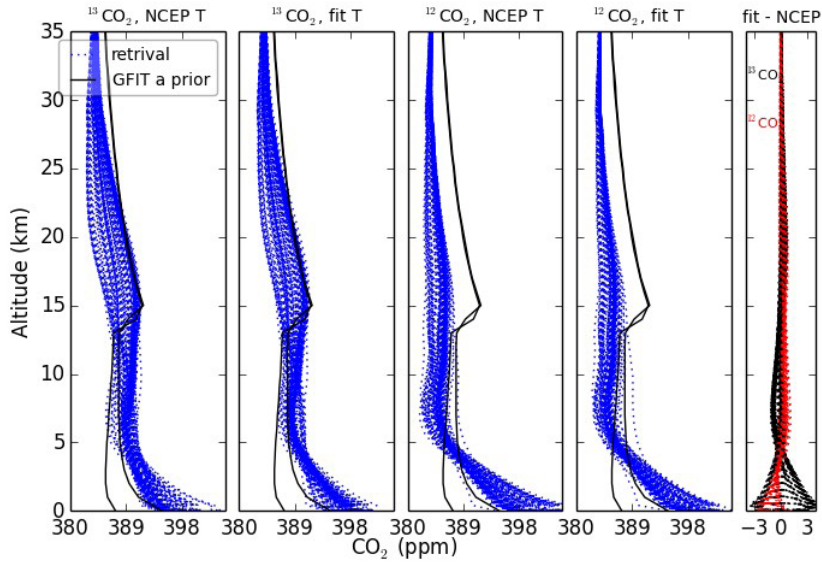


Figure 5.24. Comparison of $^{13}\text{CO}_2$ (the first and second columns) and $^{12}\text{CO}_2$ (the third and fourth columns) profiles retrieved from spectra measured at Bremen on two days. Blue lines are retrieval and black are GFIT a prior. The fifth column presents differences between with and without fitting temperature for $^{13}\text{CO}_2$ (black) and $^{12}\text{CO}_2$ (red).

Figure 5.23 and 5.24 show comparisons for columns and profiles of CO_2 retrieved from spectra measured at Bremen on two days. Fitting temperature does not improve retrievals of $\delta^{13}\text{C}$ and CO_2 profiles on these two days.

5.4. Instrumental aspect

In this section, the influences of errors arising from instrumental imperfection are investigated. Retrieval setups for $^{12}\text{CO}_2$ and $^{13}\text{CO}_2$ are kept unchanged in this section. It is a profile retrieval based optimal estimation for $^{12}\text{CO}_2$ and $^{13}\text{CO}_2$, a profile retrieval with the first-order Tikhonov-Phillips constraint for H_2O in the region $4887\text{-}4916\text{ cm}^{-1}$, scaling GFIT a prior for other species and H_2O in the $6180\text{-}6260\text{ cm}^{-1}$ region. The optimized Toth (2008a) with line mixing and speed-dependence is used for CO_2 , optimized Toth (2005) for H_2O . Tp profiles from NCEP reanalysis are used. Other details are the same as in the former sections.

5.4.1. Laser sampling error

The interferogram recorded with a FTS is sampled on discrete values of optical path difference (OPD). Errors in assumed OPD values could result in artifact spectral lines. The interferogram is sampled at the zero crossings of reference laser interferogram, the laser is fed into the spectrometer

and goes in the same ways as signal being measured, e.g. solar radiation. An incorrect mean intensity level of laser interferogram can lead to a periodic sampling error, and distortions of the true spectrum after Fourier transformation (Dohe et al., 2013). The spectra measured at Bialystok during the period 2009-2011 are used to investigate influences of the laser sampling error on CO₂ retrievals. The laser sampling error (LSE) represented in a fraction of sampling increment ranges -0.004 to 0.004 in this period. Figure 5.25 and 5.26 present influences of LSE on retrievals of δ¹³C and CO₂ profiles. It can be seen that the influences on the both are small, -0.4 to 0.4 for δ¹³C and -5 to 5 ppm for CO₂ profiles.

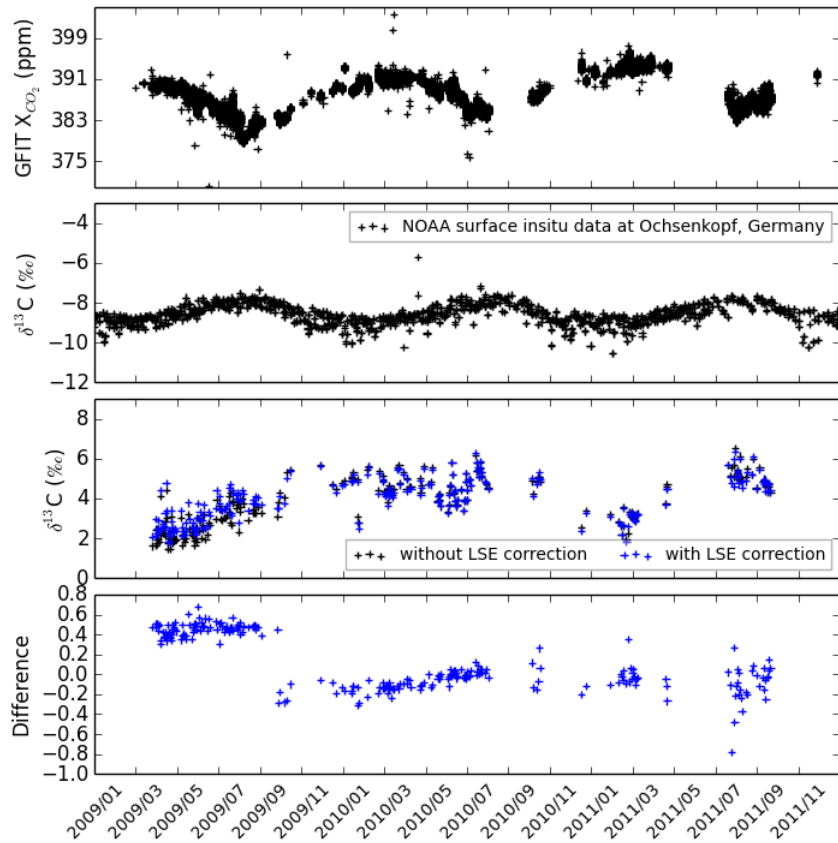


Figure 5.25. Daily mean of retrieved δ¹³C from spectra measured at Bialystok in the period 2009-2011 with and without LSE correction, and the difference between them (the fourth panel). The together showed are GFIT X_{CO_2} (the first panel), NOAA surface δ¹³C (the second panel) measured at Ochsenkopf (50.030°N, 11.808°E, 1009 masl), Germany.

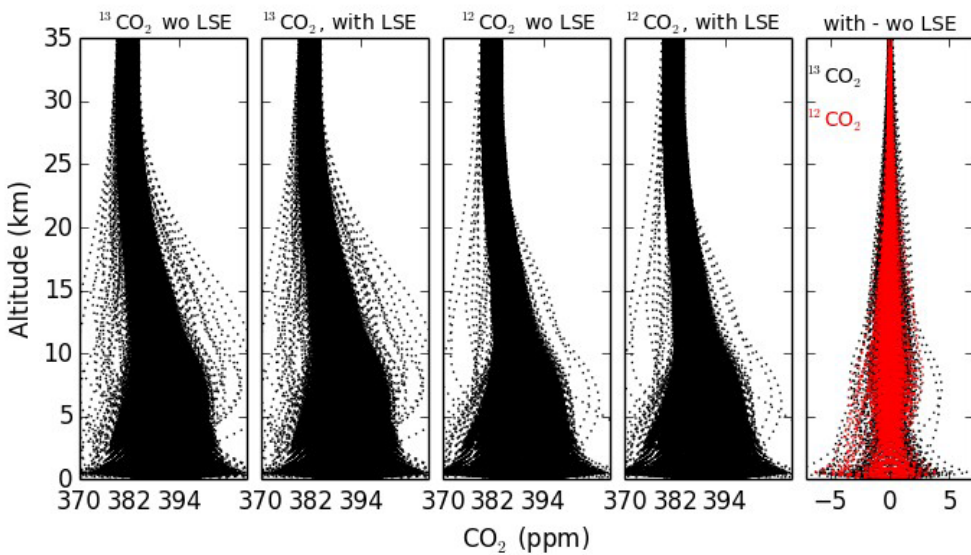


Figure 5.26. Comparison of $^{13}\text{CO}_2$ (the first and second columns) and $^{12}\text{CO}_2$ (the third and fourth columns) profiles retrieved from spectra measured at Bialystok in the period 2009-2011 with (the second and fourth columns) and without (the first and third columns) LSE correction. The fifth column presents differences between with and without LSE correction for $^{13}\text{CO}_2$ (black) and $^{12}\text{CO}_2$ (red).

5.4.2. Instrumental line shape

In all the former retrieval, the instrumental line shape (ILS) is assumed to be a nominal one. In this section the true ILS retrieved from laboratory HCL cell measurements with code LINEFIT 14 (Hase et al., 1999) are used and its influences are investigated. The spectra measured at Bialystok in the period 2009-2011 are used, to which LSE corrections has been applied.

Figure 5.27 and 5.28 give retrieved ILS and parameters characterizing them. The FTS at Bialystok is not evacuated between August of 2009 and August of 2010, correspondingly retrieved H_2O columns from the laboratory spectra significantly depart from zero. Maximum phase error shows larger scatter in this period. As mentioned before, the retrieved $\delta^{13}\text{C}$ presents incorrect seasonal behavior. Firstly it was expected the distorted ILS contributes to the abnormal $\delta^{13}\text{C}$. However, retrievals accounting for these distortions in ILS do not differ from that using nominal ILS too much, as can be seen in Figure 5.29. The difference of $\delta^{13}\text{C}$ between using the two kinds of ILS is only about -0.5 to 0.1. It need to be noted here that the nominal ILS is used for spectra in 2011 because tests in 2009-2010 do not show any improvement and then the retrieval applying the retrieved ILS was not continued.

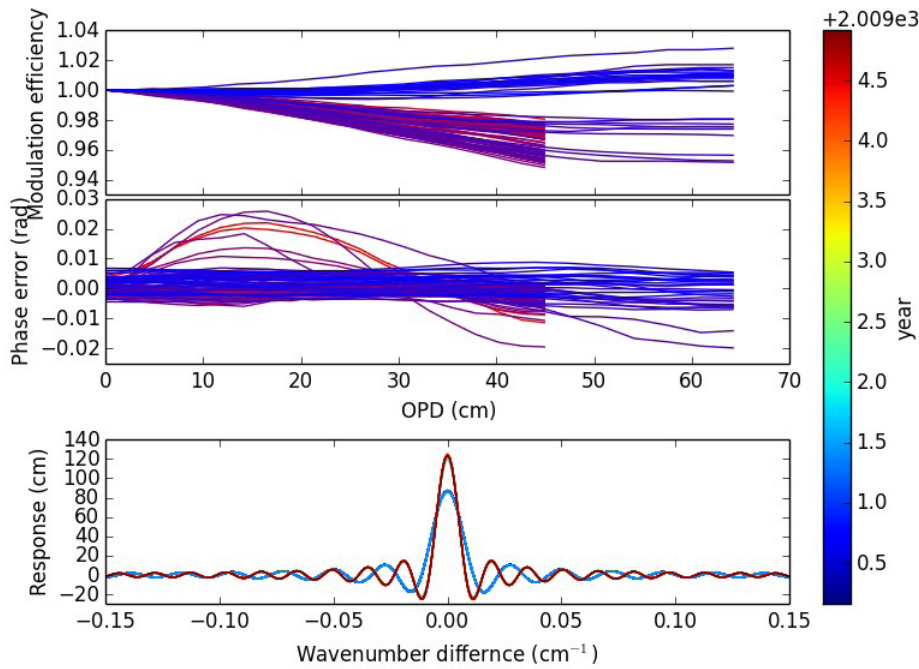


Figure 5.27. The ILS of FTS at Bialystok retrieved from laboratory measurements. The first panel shows modulation efficiency and the second phase error variabilities along with OPD. The third panel is ILS functions. The colors indicate time.

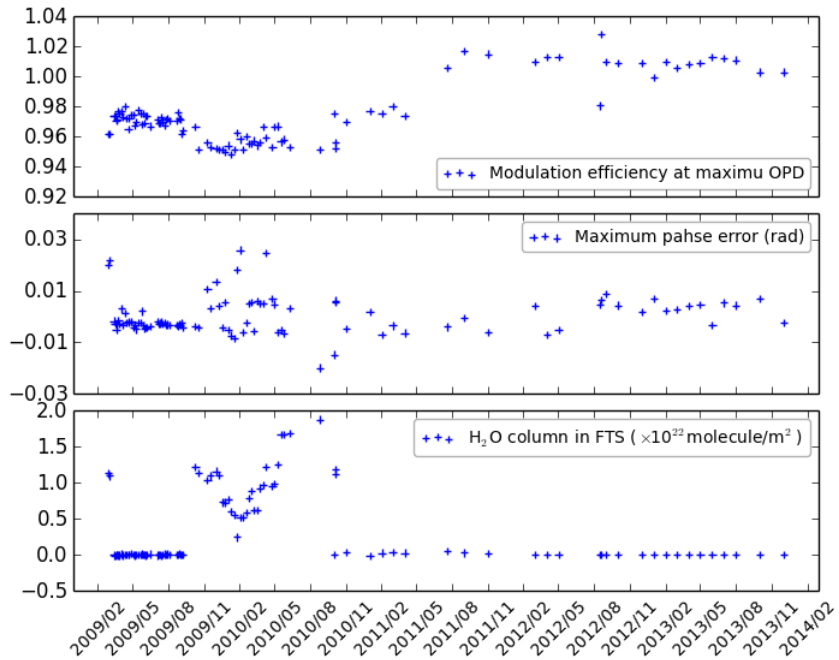


Figure 5.28. The modulation efficiency at maximum OPD (the first panel) and maximum phase error over the whole OPD (the second panel), and H₂O in the FTS (the third panel). The period with significant H₂O indicate that the FTS was not evacuated there.

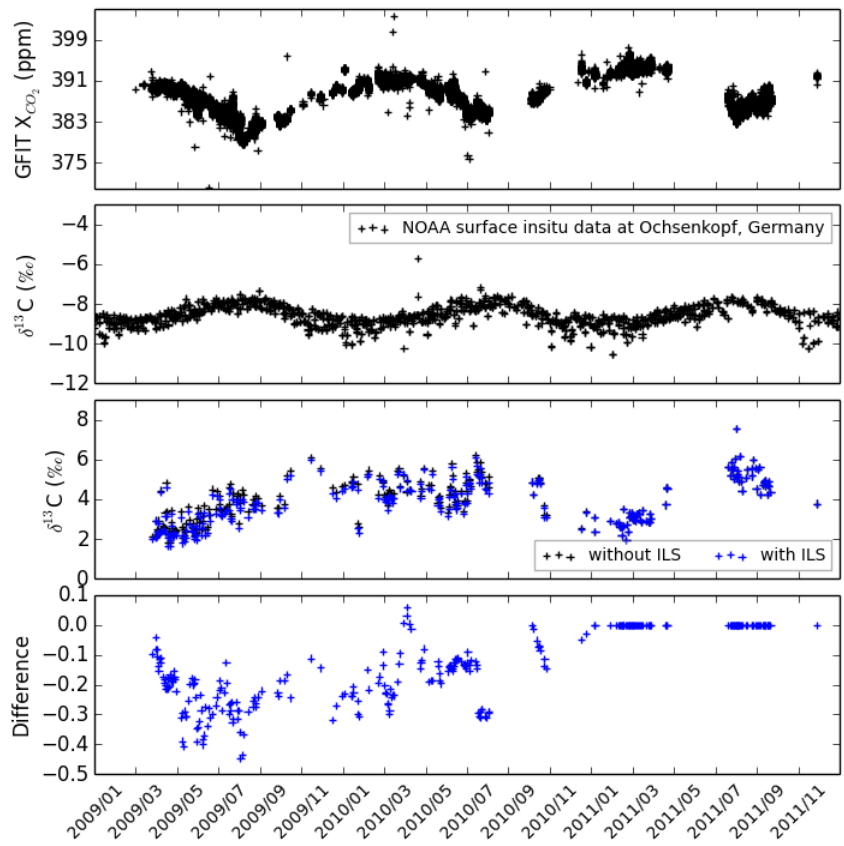


Figure 5.29. Daily mean of retrieved $\delta^{13}C$ (the third panel) from spectra measured at Bialystok in the period 2009-2011 with nominal (black) and retrieved ILS (blue) and the difference (the fourth panel). The together showed are GFIT X_{CO_2} (the first panel), NOAA surface $\delta^{13}C$ (the second panel) measured at Ochsenkopf ($50.030^\circ N$, $11.808^\circ E$, 1009 masl), Germany.

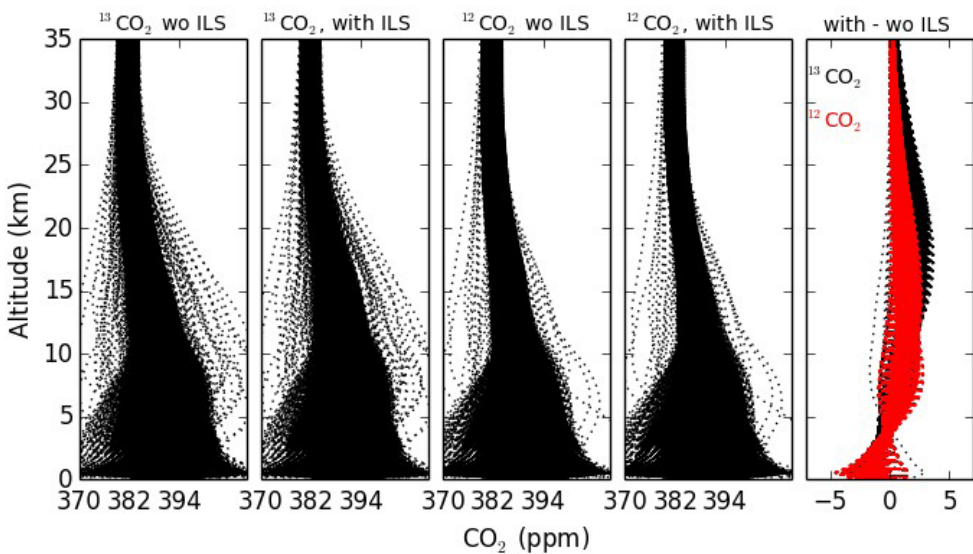


Figure 5.30. Comparison of $^{13}\text{CO}_2$ (the first and second columns) and $^{12}\text{CO}_2$ (the third and fourth columns) profiles retrieved from spectra measured at Bialystok in the period 2009-2011 with nominal (the second and fourth columns) and retrieved (the first and third columns) ILS. The fifth column presents differences between with nominal and retrieved ILS for $^{13}\text{CO}_2$ (black) and $^{12}\text{CO}_2$ (red).

Influences of ILS on the retrieval of CO_2 profiles concentrate in the stratosphere, instead of the troposphere such as those of LSE, with a larger amplitude in the case of $^{13}\text{CO}_2$. This is because non-ideal ILS distorts the center of a spectral line more significantly, which mostly comes from contribution of molecular absorption in the stratosphere where the absorption line is narrow. The absorption lines of $^{13}\text{CO}_2$ are weaker and less saturated than $^{12}\text{CO}_2$ lines and then more sensitive to the distortion at line center.

5.5. Summary

In this chapter, the possibility of retrieving $\delta^{13}\text{C}$ from ground-based solar FTS spectra is explored. To correct inaccuracies of spectroscopic parameters of H_2O , solar line and CO_2 , an algorithm retrieving molecular spectroscopy from ground-based FTS spectra is developed. It is applied to H_2O , solar line and CO_2 . While the Voigt line shape is assumed in the case of H_2O , both line mixing and speed-dependence of air-broadening are taken into account for CO_2 .

Comparisons with other existing spectroscopic datasets demonstrate applicability of the algorithm. While the inverted spectroscopic parameter reduces H_2O interference and the airmass-dependence artifact in CO_2 retrieval that mainly arises from errors in CO_2 spectroscopy, the retrieved $\delta^{13}\text{C}$ is still not reasonable enough. Tests on retrieval method setup are taken as well, a profile retrieval is applied to CO_2 instead of a commonly used profile scaling approach. Results reveal that column averaging kernels of $^{12}\text{CO}_2$ and $^{13}\text{CO}_2$ become closer to each other when the profile retrieval is used compared to the scaling approach. Differences in $\delta^{13}\text{C}$ between the two retrieval methods are significant, varying from -2 to 1. However, there still exists some incorrect seasonal behavior for spectra measured at Bialystok. Tests on H_2O retrieval setups indicate a necessity of using correct H_2O spectroscopic data and adjusting its profile in retrieving both $\delta^{13}\text{C}$ and CO_2 profiles correctly. The last test is about imperfect instrumental performances, namely the laser sampling error and non-ideal instrumental line shape. Using spectra with LSE corrections applied results in minor differences in $\delta^{13}\text{C}$, -0.2 to 0.6 only. When ILS retrieved from laboratory HCL cell spectra is used, the retrieved $\delta^{13}\text{C}$ differs from that using nominal ILS by -0.5 to 0.1 only. The incorrect seasonal behavior of $\delta^{13}\text{C}$ in some period of measurements at Bialystok still presents.

There are more error sources, probably in the instrument, left to be identified before obtaining correct isotopic compositions of CO_2 from ground-based FTS spectra.

6. Conclusions

A posterior correction method is developed to derive the tropospheric column-averaged mole fraction of CH₄ from total columns of CH₄ and N₂O. The N₂O column is used to infer contribution of stratospheric CH₄. Validation with in situ measurements reveals an accuracy of about 5 ppb for the method. Comparisons with other methods, e.g. the HF method and direct profile retrieval, reveal a more stable behavior of the developed method with respect to H₂O interference and variations of instrumental performance. A remaining problem of the method is the assumption about tropospheric N₂O mole fractions, which are not suitable to regions influenced by significant N₂O sources.

The method is applied to column measurements at TCCON sites, and derived tropospheric together total column-averaged CH₄ mole fractions are compared with three inverse modeling simulations. A combination of total and tropospheric column-averaged CH₄ separates biases in the simulations between the troposphere and stratosphere. While stratospheric bias has mostly dynamical reasons, the bias in the troposphere contains both sources (sinks) -related and transport reasons. The isentropic mixing processes in the stratosphere are diagnosed using the equivalent length. The modeled southern surf zone is not developed enough because of a too weak planetary wave breaking there. Consequently, in Jun-Jul-Aug period stratospheric CH₄ in southern mid-latitudes presents much larger isentropic gradients in the models than measurements. During the development of the southern surf zone, a region with both vertically and horizontally well mixed CH₄ occur between 450 and 850 K (~18 and 30 km) in surf zone latitudes. Such a region is absent in the models. The modeled polar vortex breaks too fast compared to the measurements. Modeled CH₄ concentrations in the polar vortex rise at all levels at same time instead of at high levels initially as in the measurements.

Retrieval of isotopic compositions of atmospheric CO₂ from ground-based FTS spectra is investigated. There are three aspects explored, spectroscopy, retrieval method and instrumental performance. An algorithm is developed to invert spectroscopic parameters using ground-based solar FTS spectra. The spectral line parameters of the molecules H₂O, CO₂, and solar line are inverted in several regions. The line mixing and speed-dependence of air-broadening effect are taken into account in inverting CO₂ spectroscopy. The inverted parameters reduce residuals of spectra fit which arise from the lines of these species, improve profile retrievals in the case of H₂O and ¹³CO₂, and weaken airmass-dependence of retrieved ¹²CO₂ and ¹³CO₂ columns. Tests on retrieval methods reveal that importance of H₂O interference on ¹³CO₂ retrieval, and applying profile retrieval for both ¹²CO₂ and ¹³CO₂ in a retrieval of the isotopic ratio of CO₂. On deficiencies of FTS instrument, only laser sampling errors and distortions of instrumental line shape are examined and results show their minor influence. More works are needed to explore other aspects of instrumental performance.

Appendix

A. Derivation of formula for integrating in situ profile

The formula Eq. 3.11 for integrating in situ profile to validate a derived tropospheric column-averaged mole fraction of CH₄ is derived here. Inserting the expression for retrieved total column Eq. 3.9 into Eq. 3.10 and considering the expression of φ_y , we have,

$$X_{CH_4}^{trop} = \frac{\int_0^{P_s} a_{CH_4} f_t^{CH_4} \frac{dp}{mg} - b \mu_y \left(\int_0^{P_s} a_y (f_t^y - X_y^{trop}) \frac{dp}{mg} \right)}{\varphi_{CH_4} VC_{air}}. \quad (\text{A.1})$$

The integration in the second term in the numerator contains the averaging kernel of species y , and the multiplier μ_y in front of it is used to convert it into an integration contain the averaging kernel of CH₄. The calculation of this multiplier needs the true profile of y as shown in Eq. 3.10. But in practice the true profile is not available, and approximated by a subsided reference profile as being described in section 3.1.3. Assuming such approximation creates only small error, then

$$X_{CH_4}^{trop} = \frac{\int_0^{P_s} a_{CH_4} f_t^{CH_4} \frac{dp}{mg} - b \left(\int_0^{P_s} a_{CH_4} (f_t^y - X_y^{trop}) \frac{dp}{mg} \right)}{\varphi_{CH_4} VC_{air}}. \quad (\text{A.2})$$

Because $f_y - X_y^{trop}$ is zero in the troposphere, and splitting integration for the true profile of CH₄ into the troposphere and stratosphere,

$$X_{CH_4}^{trop} = \frac{\int_{P_t}^{P_s} a_{CH_4} f_t^{CH_4} \frac{dp}{mg} + \int_0^{P_t} a_{CH_4} [f_t^{CH_4} - b(f_t^y - X_y^{trop})] \frac{dp}{mg}}{\varphi_{CH_4} VC_{air}}, \quad (\text{A.3})$$

where P_t is tropopause pressure. According to Eq. 3.1 the mole fractions of y and CH₄ are linearly correlated in the stratosphere, then the term $f_t^{CH_4} - b(f_t^y - X_y^{trop})$ is a constant representing tropospheric CH₄ concentration. The first term in the numerator of Eq. A.3 is the tropospheric column of CH₄, and can be rewritten as,

$$\left[\left(\int_{P_t}^{P_s} a_{CH_4} f_t^{CH_4} \frac{dp}{mg} \right) / \left(\int_{P_t}^{P_s} a_{CH_4} \frac{dp}{mg} \right) \right] \int_{P_t}^{P_s} a_{CH_4} \frac{dp}{mg} \quad (\text{A.4})$$

Assuming the tropospheric CH₄ concentration represented by the constant $f_t^{CH_4} - b(f_t^y - X_y^{trop})$ is a same quantity as the term in the square bracket in Eq. A.4, and considering the expression of φ_{CH_4} , we have,

$$X_{CH_4}^{trop} = \left(\int_{P_t}^{P_s} a_{CH_4} f_t^{CH_4} \frac{dp}{mg} \right) / \left(\int_{P_t}^{P_s} a_{CH_4} \frac{dp}{mg} \right) \quad (\text{A.5})$$

B. Derivation of formula for correcting airmass-dependent artifact

From Eq. 2.10 the retrieved quantity include contribution from true and a prior quantity, error in forward model parameters, error in forward model and measurement noise. Replacing Δf in Eq. 2.10 with the difference between forward function and forward model using Eq. 2.9, ignoring measurement noise and rearranging, we have following equation,

$$\hat{x} = x + (A - I)(x - x_a) + G(f(x, b, b') - F(x, \hat{b})), \quad (\text{B.1})$$

where, G is a $n \times m$ matrix representing sensitivity of the retrieval to the measurements, n is the dimension of state vector x and m is the dimension of measurement vector describing accurately by the forward function f or approximated by the forward model F . b and b' are known and unknown forward function parameters, \hat{b} is an estimation of the known parameters in the forward function. Here, the hat symbol always means an estimation of a corresponding quantity. Averaging kernel A , which has a dimension of $n \times n$, and sensitivity matrix G are both evaluated at the retrieved state \hat{x} but hat notations are drop for convenience. I is a unit matrix with the same dimension with the averaging kernel. \hat{x} , x , x_a are retrieved, true and a prior state vectors with a dimension of n , respectively. For ground-based FTS spectra, ignoring instrumental effects the forward function can be written as,

$$f(x, b, b') = CL(\sigma) \exp \left(- \sum_i \sum_j g_{ij}(\sigma) S_{ij} \tilde{y}_{ij} d_i l_i \frac{Y_j P_s}{\cos(SZA_i)} \right), \quad (\text{B.2})$$

where, CL is solar radiation at top of the atmosphere, σ is wavenumber that is a vector with a dimension of m . g_{ij} , S_{ij} , \tilde{y}_{ij} are line shape function, line intensity and mole fraction normalized by total column-averaged mole fraction Y_j , the subscript j means the j th gas and i the i th altitude level. d_i , l_i , SZA_i are number density of air molecule normalized by surface pressure P_s and vertical length of the i th level and solar zenith angle at that altitude. Correspondingly, the forward model can be expressed as,

$$F(x, \hat{b}) = \hat{CL}(\sigma) \exp \left(- \sum_i \sum_j \hat{g}_{ij}(\sigma) \hat{S}_{ij} \tilde{y}_{ij} d_i l_i \frac{Y_j P_s}{\cos(SZA_i)} \right). \quad (\text{B.3})$$

Ignoring the difference between CL and its estimation, and because spectroscopic errors are constant, the difference between the forward function and forward model can be expressed as,

$$f(x, b, b') - F(x, \hat{b}) = \begin{pmatrix} \ddots & & 0 \\ & \prod_{j=1}^J h\left(\frac{Y_j P_s}{\cos(SZA)}, \tilde{y}_j\right) - 1 & \\ 0 & & \ddots \end{pmatrix} \times F(x, \hat{b}),$$

$$\equiv E \times F(x, \hat{b}) \quad (\text{B.4})$$

where,

$$h\left(\frac{Y_j P_s}{\cos(SZA)}, \tilde{y}_j\right) = \exp\left(-\sum_i (g_{ij} S_{ij} - \hat{g}_{ij} \hat{S}_{ij}) \tilde{y}_j d_i l_i \frac{Y_j P_s}{\cos(SZA)}\right). \quad (\text{B.5})$$

In deriving Eq. B.4, the variation of SZA along path of solar radiation is ignored. Because the sensitivity matrix G means doing a retrieval, from Eq. B.1 we have,

$$GF(x, \hat{b}) = x + (A - I)(x - x_a). \quad (\text{B.6})$$

The error terms in Eq. B.1 have been disregarded since the measurement is just the forward model F vector. Since matrix E is a function of $Y_j P_s / \cos(SZA)$ and \tilde{y}_j , then we might have following relation,

$$GEF(x, \hat{b}) = C\left(\frac{Y_1 P_s}{\cos(SZA)}, \tilde{y}_1; \dots; \frac{Y_J P_s}{\cos(SZA)}, \tilde{y}_J\right)[x + (A - I)(x - x_a)], \quad (\text{B.7})$$

where, C is a diagonal matrix function and J is the total number of the gases considered. Inserting Eq. B.7 into Eq. B.1, we have,

$$\hat{x} = [I + C\left(\frac{Y_1 P_s}{\cos(SZA)}, \tilde{y}_1; \dots; \frac{Y_J P_s}{\cos(SZA)}, \tilde{y}_J\right)][x + (A - I)(x - x_a)]. \quad (\text{B.8})$$

If correction function C is known, the error in the retrieval, including airmass-dependent artifact, resulted from spectroscopic inaccuracies could be removed.

List of Tables

4.1. Overview of TCCON sites used for evaluation of models.....	36
4.2. The models used in the comparison with solar absorption measurements.....	38
4.3. The sites used for comparison of FTS tropospheric column-averaged CH ₄ mole fraction and in situ surface/tower CH ₄ mole fraction.....	39

List of Figures

1.1. Sources and sinks of atmospheric CH ₄ with errorbar indicating spread of the reported values. There are not uncertainties given for the fresh water and Cl in marine BL because their measurements are rare.....	3
1.2. Satellite measurements of column-averaged CH ₄ concentration for 2003-2005. [Courtesy of M. Buchwitz, IUP, University of Bremen.].....	8
1.3. Zonally averaged representation of the global distribution of CH ₄ at the earth surface (mostly in the marine boundary layer). [Courtesy of NOAA/ESRL.].....	8
2.1. Diagram sketch of a Fourier transform infrared spectrometry. r and t represent reflection and transmission coefficients, their subscripts denote corresponding object. x_1 and x_2 are paths of two beams.....	10
3.1. Correlations between the stratospheric mole fractions of N ₂ O (right) and HF (left) with CH ₄ on a global scale. Correlation coefficient, slope and intercept are indicated in the legend. The data are from the ACE-FTS satellite.....	19
3.2. The residual yearly mean N ₂ O at each latitude band relative to globally yearly mean (left), and residual monthly mean N ₂ O relative to yearly mean at each latitude band (right). The residuals are averaged over all measurement years. The residuals are derived from N ₂ O data from NOAA/ERSL in situ measurements at ground level.....	20
3.3. The averaging kernels of HF, N ₂ O and CH ₄ at Bialystok for all spectra from 2010. the colors indicate the solar zenith angle (SZA) of the corresponding measurements.....	21
3.4. Results at Ny-Ålesund, the red points correspond to the tropospheric column-averaged CH ₄ mole fraction derived from N ₂ O, the blue to those derived using HF and the open circles are in situ CH ₄ data measured at Zeppelin mountain. The upper panel shows the difference between the in situ and tropospheric column-averaged CH ₄ mole fractions, the middle panel is the difference between the results using N ₂ O and HF.....	25
3.5. Same as Fig. 3.4 except for at the Orléans site and with the black circles lower panel representing tropospheric column-averaged CH ₄ mole fraction from low altitude aircraft profiles..	25
3.6. Same with Fig. 3.4 except for at Bialystok.....	26
3.7. Results at Darwin.....	26
3.8. The multi-annual mean seasonal cycles of tropospheric column-averaged CH ₄ mole fraction for four sites. The red points correspond to the results derived from N ₂ O and the blue to HF.....	27
3.9. Comparison results of FTS tropospheric column-averaged CH ₄ mole fraction with aircraft data. The aircraft profiles are smoothed using GFIT averaging kernels in troposphere using Eq. 3.11. The FTS data are averaged through aircraft measurements periods, and the error bars of FTS data are	

standard deviations of these averaged data.....	28
3.10. Relative error estimation of the tropospheric column-averaged CH ₄ mole fraction using Gaussian error propagation equation for four sites, the blue corresponds to the error for the method using HF and the red to that of method using N ₂ O.....	29
3.11. Same as Fig. 3.10 except for that the relative error is estimated as the standard deviation of tropospheric column-averaged CH ₄ mole fractions during one day divided by the daily mean.....	29
3.12 The five microwindows used for the retrieval of CH ₄ profiles for an example spectrum at Bremen. Lower panel is the transmission with black points representing measurements and black line representing simulation. Upper panel are the differences between the measurement and simulation.....	32
3.13 The averaged CH ₄ profiles and its characteristics at Ny-Ålesund in the period 2007-2012. Left panel is the a prior (dashed line) and average of retrieval (solid line, error bar is the standard deviation). Right panel is the average of averaging kernel, with the red lines representing averaging kernels of CH ₄ mole fractions at lowest six layers.....	32
3.14 The tropospheric column-averaged CH ₄ mole fraction from the posterior correction method using N ₂ O (red pluses) and lower tropospheric column-averaged CH ₄ mole fraction (blue crosses) at Ny-Ålesund (mid panel) and Bremen (lower panel). Black circles represent in situ surface CH ₄ measured at Zeppelin mountain (upper panel) and Mace Head (lower panel). Upper panel is the difference of FTS CH ₄ to in situ CH ₄ at Ny-Ålesund, difference is not performed at Bremen because of the large distance between the FTS and in situ sites. Daily medians are shown for all measurements.....	33
4.1. Validation results of FTS derived tropospheric column-averaged CH ₄ mole fractions with in situ measurements. The in situ profiles are smoothed using GFIT CH ₄ averaging kernels in troposphere as described in Sect. 3.1.5. The FTS data are averaged through th aircraft measurements periods...41	41
4.2. Global distribution of surface sampling/in situ sites at which measurements are assimilated into TM3 (square), TM5-4DVAR (diamond) and LMDz-PYVAR (horizontal line) in their inversion run.....	41
4.3. Comparison between FTS derived tropospheric column-averaged CH ₄ and in situ surface/tower CH ₄ . In the left panel, the black and blue crosses represent the daily median of in situ CH ₄ and tropospheric column-averaged CH ₄ , respectively. The curves are fitted long-term variations with time scale longer than 1.4 years. The lines in the right panel represent the difference between the long-term variations of tropospheric and in situ CH ₄ (black), and the long term increase rate of tropospheric (green) and in situ (blue) CH ₄42	42
4.4. Differences of total (right) and tropospheric (left) column-averaged CH ₄ concentration between FTS measurements and model simulations at European sites. The differences are shift for clarity and black dash line indicate zero position for each site. The increment of Y-axis is 30 ppb. The	

green, blue and yellow points represent difference between FTS measurement and TM3, TM5-4DVAR and LMDz-PYVAR simulations. Each point is the average over 7 days.....	43
4.5. Anomalies of measured (black) and simulated (yellow: TM3; blue: TM5-4DVAR; green: LMDz-PYVAR) vertical gradient of CH ₄ in the troposphere with respect to their averages. The anomalies have been shifted for clarity and dashed line indicate zero level for each site.....	44
4.6. Annual mean total, tropospheric and stratospheric column-averaged CH ₄ mole fractions plotted as a function of latitude. The upper panel is the results of FTS measurements while the lower panels is the difference between the measurements and the TM3 (yellow), TM5-4DVAR (blue) and LMDz-PYVAR (green) simulations. The annual mean is calculated as yearly mean of the fitted long-term variation. Medians over all time, and also split into different seasons, are shown for the differences.....	46
4.7. Total column-averaged CH ₄ mole fraction measured by GOSAT (upper panel) and difference with simulations by the models (lower panel). The results are averaged over the period 2009-2011 and along longitude, with a latitude bin of 4°. Both averages for whole year (marked solid line) and different seasons (DJF: solid; MAM: dashed; JJA: dotted; SON: dash dot) are shown. The yellow, blue and green points represent results for TM3, TM5-4DVAR and LMDz-PYVAR respectively.....	47
4.8. Measured (black) and simulated (yellow: TM3, blue: TM5-4DVAR, green: LMDz-PYVAR) vertical gradients of CH ₄ in the troposphere (top panel) and differences between the measurement and simulations (lower panel) against latitude.....	47
4.9. Yearly and seasonal medians of the stratospheric and tropospheric contributions in modeled total column biases at TCCON sites. The white bar denotes the tropospheric bias, the grey bar the stratospheric bias. The scale factor for the model bias is the air column fraction P _t /1000 (stratosphere) and (1-P _t /1000) (troposphere), where P _t is the tropopause pressure. The standard deviations of the bias amplitudes are shown separately for the troposphere (black error bar) and the stratosphere (blue error bar). The results are averaged for 2007-2011 where FTS measurements are available.....	48
4.10. Same as Fig. 4.9 except for medians of model bias amplitudes (absolute model to FTS differences). The standard deviations of the bias amplitudes are shown separately for the troposphere (black error bar) and the stratosphere (blue error bar).....	49
4.11. HIPPO measured CH ₄ distribution in the stratosphere (short panel) and the troposphere (high panel) and differences with model simulations. The results are averages for five HIPPO missions, for latitudinal bins of 4° and vertical increments of 10 hPa.....	50
4.12. Median CH ₄ concentrations as a function of latitude and altitude spanning the 2009-2011 period for ACE-FTS, TM3, TM5-4DVAR and LMDz-PYVAR.....	51
4.13. Median Model - ACE-FTS biases as a function of altitude and latitude for different seasons	

(DJF = December-February, MAM = March-May, etc) and models (left TM3, mid TM5-4DVAR and right LMDz-PYVAR) spanning 2009-2011 period.....	53
4.14. Stratospheric column-averaged CH ₄ mole fraction measured by MIPAS and simulated by models (upper panel), and difference between the simulations and measurements (lower panel). The results are medians over the period 2009-2011 and along longitude, within a latitude bin of 4°. Both medians for whole year (points) and different seasons (DJF: solid; MAM: dashed; JJA: dotted; SON: dash dot) are shown. The yellow, blue and green points represent results for TM3, TM5-4DVAR and LMDz-PYVAR respectively.....	53
4.15. Cross sections in Oct. 2009~Aug. 2010 of equivalent length (color: the red indicates large values and the blue for small values and color is plotted on a logarithmic scale, the white means no data or larger values), contour of CH ₄ (thick black line with an increment of 100 ppb) and zonal mean zonal wind (thin black lines with solid for westerlies and zero values and dashed lines for easterlies, the increment is 10 m/s) along equivalent latitudes (but latitudes for wind) and potential temperatures. The equivalent latitude φ_e is defined by $A=2\pi a^2(1-\sin \varphi_e)$, A is the area bounded by a constant CH ₄ line on an isentropic surface and a is the earth radius. The equivalent length has been scaled by $2\pi r \cos \varphi_e$ and is unitless. Results for MIPAS, TM3, TM5-4DVAR and LMDz-PYVAR are shown, respectively, starting from the uppermost panel.....	58
4.16. Comparison between FTS retrieved CH ₄ profiles and those simulated by models at Ny-Ålesund (left) and Bremen (right). The model profiles have been smoothed with averaging kernels of the retrieval taking a prior into account. The first row is the retrieved profiles, and following rows are differences between retrieval and simulation for TM3, TM5-4DVAR and LMDz-PYVAR respectively. The colors indicate CH ₄ mole fractions.....	59
4.17. Comparisons of partial column of CH ₄ (first two rows) and lower tropospheric column-averaged CH ₄ mole fraction (last two rows) between FTS measurements and model simulations at Ny-Ålesund (left) and Bremen (right). The partial column is an integration of CH ₄ profile from 11 km to TOA (top of the atmosphere). The lower tropospheric column-averaged CH ₄ mole fraction is a mean mole fraction of profile below about 2.4 km. The shown results are daily medians.....	60
5.1. Temperature (left) and H ₂ O (right) profiles measured by radiosonde (Darwin and Lamont) and aircraft (Bialystok and Orléans) near the time of FTS measurements used for inverting H ₂ O spectroscopy parameter.....	69
5.2. Example fit effect using H ₂ O spectroscopy from Toth (2005) (the first panel), inversion (the second panel), HITRAN 12 (the third panel). The lowest panel gives transmission measured (dot) and calculated (solid line). The spectrum is measured at TCCON site Bremen.....	69
5.3. Retrieved H ₂ O profiles (Blue dashed line) from the spectra measured at Bremen using three different spectroscopy, Toth (2005) (left), Inverted (middle) and HITRAN 12 (right). The black line is NCEP daily mean H ₂ O profile and yellow is a prior.....	70
5.4. Standard deviation (upper panel) of residual and DOFS (lower panel) for the retrieval in Figure	

5.3.....	70
5.5. Same as for Fig. 5.2 except for a region 4886.70 to 4916.30 cm ⁻¹ and that line mixing effect is modeled for CO ₂ , and there is not N ₂ O absorption in this region.....	71
5.6. Example fit effect using solar line database of PROFFIT (the first panel) and from inversion (the second panel). The lowest panel gives transmission measured (dot) and calculated (solid line). The spectrum is measured at TCCON site Bialystok.....	73
5.7. CO ₂ column-averaged mole fraction retrieved from spectra measured at Bremen using solar line database of PROFFIT (black) and that inverted (blue). The first panel is difference, the second CO ₂ mole fraction, the third SZA. Air column is derived from surface pressure.....	73
5.8. residual variations when using different spectroscopy, Toth (2008a) (the first panel), Toth (2008a) with line mixing (the second panel), optimized Toth (2008a) with line mixing (the third panel) and optimized Toth (2008a) with line mixing and speed-dependence of air-broadening effect (the fourth panel), for CO ₂ in region 6180-6260 cm ⁻¹ . The lowest panel give transmission, the spectrum is measured at Bialystok under a SZA of 81.7°.....	75
5.9. Same as Fig. 5.8 except for region 4887-4916 cm ⁻¹	76
5.10. Comparison of intensities at 296 K of CO ₂ lines in regions 6180-6260 cm ⁻¹ (left) and 4887-4916 cm ⁻¹ between Toth (2008a) (black), optimized with line mixing (blue) and both line mixing and speed-dependence of air-broadening (red) taken into account. The first panel give percent differences and the second absolute value.....	76
5.11. Same as Fig. 5.10 except for air-broaden half width at 296 K, γ_{air}	77
5.12. Same as Figure 5.10 except for the first-order line mixing coefficient at 260 K, Y_{260}	77
5.13. Inverted speed-dependence parameter for air-broadening at 296 K, γ_2	78
5.14. Comparison of column-averaged ¹² CO ₂ (red) and ¹³ CO ₂ (black) mole fractions retrieved from two days measurements at Bremen using different spectroscopy, Toth (2008a) (plus), Toth (2008a) with line mixing parameter (cross), optimized with line mixing (horizontal line) and both line mixing and speed-dependence of air-broadening (vertical line) taken into account. The first panel is difference, the second CO ₂ mole fraction and the third SZA. Surface pressure is used to calculate air column.....	79
5.15. Same as Fig. 5.14 except for $\delta^{13}C$	80
5.16. Comparison of ¹² CO ₂ profiles retrieved from two days measurements at Bremen using different spectroscopy, Toth (2008a) (the first panel from the left), Toth (2008a) with line mixing parameter (the second panel from the left), optimized with line mixing (the third panel from the left) and both line mixing and speed-dependence of air-broadening (the fourth panel from the left) taken into account. The blue line is the retrieval and black is GFIT a prior.....	80

5.17. Same as Fig. 5.16 except for $^{13}\text{CO}_2$ profiles. Note a different x axis scale is used for the first and second panel from the left.....	81
5.18. Variations of $^{13}\text{CO}_2$ column using different setups for fitting H_2O , using optimized Toth (2005) line parameter and adjusting profile (plus), using Toth (2005) line parameter and adjusting profile (cross), using HITRAN 12 line parameter and adjusting profile (horizontal line), using optimized Toth (2005) line parameter and scaling (vertical line) GFIT a prior. In all cases, $^{13}\text{CO}_2$ is retrieved thorough scaling GFIT a prior and using the optimized Toth (2008a) with both line mixing and speed-dependence of air-broadening taken into account.....	82
5.19. Same as Fig. 5.18 except for that $^{13}\text{CO}_2$ profiles are retrieved using optimal estimation approach.....	82
5.20. Correlation matrix of a prior covariance $r_{ij} = S_{a,ij}/(\sigma_i \sigma_j)$ (left) and a prior profile with square root of diagonal elements of a prior covariance represented by the error bar (right).....	84
5.21. Column averaging kernels of CO_2 retrieval for region 6180-6260 cm^{-1} (black) and 4887-4916 cm^{-1} (blue) using profile retrieval (solid line) and scaling (dashed line). The kernels are from three example spectra measured at Bialystok and with SZA of 30°, 70° and 81°.....	84
5.22. Daily mean of retrieved $\delta^{13}\text{C}$ from spectra measured at Bialystok in the period 2009-2011 through scaling GFIT a prior (the third panel, black) and profile retrieval (the third panel blue) for fitting CO_2 , and the difference between them (the fourth panel). The together showed are GFIT X_{CO_2} (the first panel), NOAA surface $\delta^{13}\text{C}$ (the second panel) measured at Ochsenkopf (50.030°N, 11.808°E, 1009 masl), Germany.....	85
5.23. Comparison of $\delta^{13}\text{C}$ between with (cross) and without (plus) fitting temperature. The spectra are measured at Bremen on two days.....	86
5.24. Comparison of $^{13}\text{CO}_2$ (the first and second columns) and $^{12}\text{CO}_2$ (the third and fourth columns) profiles retrieved from spectra measured at Bremen on two days. Blue lines are retrieval and black are GFIT a prior. The fifth column presents differences between with and without fitting temperature for $^{13}\text{CO}_2$ (black) and $^{12}\text{CO}_2$ (red).....	87
5.25. Daily mean of retrieved $\delta^{13}\text{C}$ from spectra measured at Bialystok in the period 2009-2011 with and without LSE correction, and the difference between them (the fourth panel). The together showed are GFIT X_{CO_2} (the first panel), NOAA surface $\delta^{13}\text{C}$ (the second panel) measured at Ochsenkopf (50.030°N, 11.808°E, 1009 masl), Germany.....	88
5.26. Comparison of $^{13}\text{CO}_2$ (the first and second columns) and $^{12}\text{CO}_2$ (the third and fourth columns) profiles retrieved from spectra measured at Bialystok in the period 2009-2011 with (the second and fourth columns) and without (the first and third columns) LSE correction. The fifth column presents differences between with and without LSE correction for $^{13}\text{CO}_2$ (black) and $^{12}\text{CO}_2$ (red).....	89
5.27. The ILS of FTS at Bialystok retrieved from laboratory measurements. The first panel shows	

modulation efficiency and the second phase error variabilities along with OPD. The third panel is ILS functions. The colors indicate time.....	90
5.28. The modulation efficiency at maximum OPD (the first panel) and maximum phase error over the whole OPD (the second panel), and H ₂ O in the FTS (the third panel). The period with significant H ₂ O indicate that the FTS was not evacuated there.....	90
5.29. Daily mean of retrieved δ ¹³ C (the third panel) from spectra measured at Bialystok in the period 2009-2011 with nominal (black) and retrieved ILS (blue) and the difference (the fourth panel). The together showed are GFIT X _{CO₂} (the first panel), NOAA surface δ ¹³ C (the second panel) measured at Ochsenkopf (50.030°N, 11.808°E, 1009 masl), Germany.....	91
5.30. Comparison of ¹³ CO ₂ (the first and second columns) and ¹² CO ₂ (the third and fourth columns) profiles retrieved from spectra measured at Bialystok in the period 2009-2011 with nominal (the second and fourth columns) and retrieved (the first and third columns) ILS. The fifth column presents differences between with nominal and retrieved ILS for ¹³ CO ₂ (black) and ¹² CO ₂ (red).....	91

Publications

Wang, Z., Deutscher, N. M., Warneke, T., Notholt, J., Dils, B., Griffith, D. W. T., Schmidt, M., Ramonet, M., and Gerbig, C.: Retrieval of tropospheric column-averaged CH₄ mole fraction by solar absorption FTIR-spectrometry using N₂O as a proxy, *Atmos. Meas. Tech.*, 7, 3295-3305, doi:10.5194/amt-7-3295-2014, 2014.

References

- Allan, W., Struthers, H. and Lowe, D. C.: Methane carbon isotope effects caused by atomic chlorine in the marine boundary layer: Global model results compared with Southern Hemisphere measurements, *J. Geophys. Res.*, 112, D04306, 2007.
- Avallone, L. M., and Prather, M. J.: Tracer-tracer correlations: Three-dimensional model simulations and comparisons to observations, *J. Geophys. Res.*, 102, 19233-19246, 1997.
- Atkinson, R.: Kinetics of the gas-phase reactions of OH radicals with alkanes and cycloalkanes, *Atmos. Chem. Phys.*, 3, 2233-2307, doi:10.5194/acp-3-2233-2003, 2003.
- Alexe, M., Bergamaschi, P., Segers, A., Detmers, R., Butz, A., Hasekamp, O., Guerlet, S., Parker, R., Boesch, H., Frankenberg, C., Scheepmaker, R. A., Dlugokencky, E., Sweeney, C., Wofsy, S. C., and Kort, E. A.: Inverse modeling of CH₄ emissions for 2010–2011 using different satellite retrieval products from GOSAT and SCIAMACHY, *Atmos. Chem. Phys.*, 15, 113-133, doi:10.5194/acp-15-113-2015, 2015.
- Bousquet, P., Ciais, P., Miller, J. B., Dlugokencky, E. J., Hauglustaine, D. A., Prigent, C., Van der Werf, G. R., Peylin, P., Brunke, E. G., Carouge, C., Langenfelds, R. L., Lathiere, J., Papa, F., Ramonet, M., Schmidt, M., Steele, L. P., Tyler, S. C., and White, J.: Contribution of anthropogenic and natural sources to atmospheric methane variability, *Nature*, 443, 439–443, 2006.
- Bridgman, S. D., Cadillo-Quiroz, H., Keller, J. K. and Zhuang, Q.: Methane emissions from wetlands: biogeochemical, microbial, and modeling perspectives from local to global scales, *Glob Change Biol Global Change Biology*, 1325–1346, 2013.
- Bousquet, P., P. Ciais, J. B. Miller, E. J. Dlugokencky, D. A. Hauglustaine, C. Prigent, G. R. Van Der Werf, P. Peylin, E.-G. Brunke, C. Carouge, R. L. Langenfelds, J. Lathière, F. Papa, M. Ramonet, M. Schmidt, L. P. Steele, S. C. Tyler, and J. White. Contribution of anthropogenic and natural sources to atmospheric methane variability, *Nature*, 443, 2006.
- Bastviken, D., Tranvik, L. J., Downing, J. A., Crill, P. M. and Enrich-Prast, A.: Freshwater Methane Emissions Offset the Continental Carbon Sink, *Science*, 50, 2011.
- Bousquet, P., Ringeval, B., Pison, I., Dlugokencky, E. J., Brunke, E.-G., Carouge, C., Chevallier, F., Fortems-Cheiney, A., Frankenberg, C., Hauglustaine, D. A., Krummel, P. B., Langenfelds, R. L., Ramonet, M., Schmidt, M., Steele, L. P., Szopa, S., Yver, C., Viovy, N., and Ciais, P.: Source attribution of the changes in atmospheric methane for 2006–2008, *Atmos. Chem. Phys.*, 11, 3689–3700, doi:10.5194/acp-11-3689-2011, 2011.
- Bernath, P. F., et al.: Atmospheric Chemistry Experiment (ACE): Mission overview, *Geophys. Res. Lett.*, 32, L15S01, doi:10.1029/2005GL022386, 2005.
- Bergamaschi, P., Frankenberg, C., Meirink, J. F., Krol, M., Villani, M. G., Houweling, S., Dentener, F., Dlugokencky, E. J., Miller, J. B., Gatti, L. V., Engel, A. and Levin, I.: Inverse modeling of global

and regional CH₄ emissions using SCIAMACHY satellite retrievals, *J. Geophys. Res.*, 114, D22301–D22301, 2009.

Bergamaschi, P., Houweling, S., Segers, A., Krol, M., Frankenberg, C., Scheepmaker, R. A., Dlugokencky, E., Wofsy, S. C., Kort, E. A., Sweeney, C., Schuck, T., Brenninkmeijer, C., Chen, H., Beck, V., Gerbig, C.: Atmospheric CH₄ in the first decade of the 21st century: Inverse modeling analysis using SCIAMACHY satellite retrievals and NOAA surface measurements, *J. Geophys. Res.*, 118, 7350-7369. doi:10.1002/jgrd.50480, 2013.

Bergamaschi, P., Corazza, M., Karstens, U., Athanassiadou, M., Thompson, R. L., Pison, I., Manning, A. J., Bousquet, P., Segers, A., Vermeulen, A. T., Janssens-Maenhout, G., Schmidt, M., Ramonet, M., Meinhardt, F., Aalto, T., Haszpra, L., Moncrieff, J., Popa, M. E., Lowry, D., Steinbacher, M., Jordan, A., O'Doherty, S., Piacentino, S., and Dlugokencky, E.: Top-down estimates of European CH₄ and N₂O emissions based on four different inverse models, *Atmos. Chem. Phys.*, 15, 715-736, doi:10.5194/acp-15-715-2015, 2015.

Crutzen, P. J. and Andreae, M. O.: Biomass Burning in the Tropics: Impact on Atmospheric Chemistry and Biogeochemical Cycles, *Science*, 1669–1678, 1990.

Curry, C. L.: Modeling the soil consumption of atmospheric methane at the global scale, *Global Biogeochemical Cycles*, GB4012, 2007.

Connor, B.: Column averaging kernel definition, https://tccon-wiki.caltech.edu/Software/GGG/Averaging_Kernels, 2009.

Chevallier, F., Fisher, M., Peylin, P., Serrar, S., Bousquet, P., Bréon, F.-M., Chédin, A. and Ciais, P.: Inferring CO₂ sources and sinks from satellite observations: Method and application to TOVS data, *J. Geophys. Res.*, 110, D24309–D24309, 2005.

Chen, P., Holton, J. R., O'Neill, A. and Swinbank, R.: Quasi-horizontal transport and mixing in the Antarctic stratosphere, *J. Geophys. Res.*, 99(D8), 16851, 1994.

Craig, H.: The geochemistry of the stable carbon isotopes, *Geochimica et Cosmochimica Acta*, 3, 53–92, 1953.

Dutaur, L. and Verchot, L. V.: A global inventory of the soil CH₄ sink, *Global Biogeochemical Cycles*, 21, GB4013, 2007.

Dlugokencky, E. J., Bruhwiler, L., White, J. W. C., Emmons, L. K., Novelli, P. C., Montzka, S. A., Masarie, K. A., Lang, P. M., Crotwell, A. M., Miller, J. B., and Gatti, L. V.: Observational constraints on recent increases in the atmospheric CH₄ burden, *Geophys. Res. Lett.*, 36, L18803, doi:10.1029/2009GL039780, 2009.

Deutscher, N. M., Griffith, D. W. T., Bryant, G. W., Wennberg, P. O., Toon, G. C., Washenfelder, R. A., Keppel-Aleks, G., Wunch, D., Yavin, Y., Allen, N. T., Blavier, J.-F., Jiménez, R., Daube, B. C., Bright, A. V., Matross, D. M., Wofsy, S. C., and Park, S.: Total column CO₂ measurements at Darwin, Australia -- site description and calibration against in situ aircraft profiles, *Atmos. Meas.*

Tech., 3, 947-958, doi:10.5194/amt-3-947-2010, 2010.

Dlugokencky, E.J., P.M. Lang, A.M. Crotwell, and K.A. Masarie (2012), Atmospheric Methane Dry Air Mole Fractions from the NOAA ESRL Carbon Cycle Cooperative Global Air Sampling Network, 1983-2011, Version: 2012-09-24, Path: <ftp://ftp.cmdl.noaa.gov/ccg/ch4/flask/event/>.

Dlugokency, E. J., Steele, L. P., Lang, P. M., Masarie, K. A.: The growth rate and distribution of atmospheric methane, *J. Geophys. Res.*, 99, 17021-17043, 1994.

Devi, V. M., Benner, D. C., Brown, L., Miller, C. and Toth, R.: Line mixing and speed dependence in CO₂ at 6227.9 cm⁻¹: Constrained multispectrum analysis of intensities and line shapes in the 30013 ← 00001 band, *Journal of Molecular Spectroscopy*, 245, 52–80, 2007.

Dohe, S., Sherlock, V., Hase, F., Gisi, M., Robinson, J., Sepúlveda, E., Schneider, M. and Blumenstock, T.: A method to correct sampling ghosts in historic near-infrared Fourier transform spectrometer (FTS) measurements, *Atmos. Meas. Tech.*, 6, 1981–1992, 2013.

Etiope, G., Lassey, K. R., Klusman, R. W. and Boschi, E.: Reappraisal of the fossil methane budget and related emission from geologic sources, *Geophys. Res. Lett.*, 35, L09307, 2008.

Eskridge, R.E., Ku, J. Y., Rao, S.T., Porter, P. S., and Zurbenko, I. G.: Separating Different Scales of Motion in Time Series of Meteorological Variables, *Bull. Amer. Meteor. Soc.*, 78, 1473–1483, 1997.

Fleagle, R. G. and Businger, J. A.: An Introduction to Atmospheric Physics, International Geophysics Series, Academic Press, 25, 67–67, 1980.

Frankenberg, C., Aben, I., Bergamaschi, P., Dlugokencky, E. J., Hees, R. V., Houweling, S., Meer, P. V. D., Snel, R. and Tol, P.: Global column-averaged methane mixing ratios from 2003 to 2009 as derived from SCIAMACHY: Trends and variability, *J. Geophys. Res.*, 116, D04302–D04302, 2011.

Fischer, H., Birk, M., Blom, C., Carli, B., Carlotti, M., von Clarmann, T., Delbouille, L., Dudhia, A., Ehhalt, D., Endemann, M., Flaud, J. M., Gessner, R., Kleinert, A., Koopman, R., Langen, J., López-Puertas, M., Mosner, P., Nett, H., Oelhaf, H., Perron, G., Remedios, J., Ridolfi, M., Stiller, G., and Zander, R.: MIPAS: an instrument for atmospheric and climate research, *Atmos. Chem. Phys.*, 8, 2151-2188, doi:10.5194/acp-8-2151-2008, 2008.

Goody, R. M., Yung Y. L.: Atmospheric Radiation, Theoretical Basis, Oxford University Press, New York, Second edition, 1989.

Geibel, M. C., Messerschmidt, J., Gerbig, C., Blumenstock, T., Hase, F., Kolle, O., Lavrič, J. V., Notholt, J., Palm, M., Rettinger, M., Schmidt, M., Sussmann, R., Warneke, T., and Feist, D. G.: Calibration of column-averaged CH₄ over European TCCON FTS sites with airborne in-situ measurements, *Atmos. Chem. Phys. Discuss.*, 12, 1517-1551, doi:10.5194/acpd-12-1517-2012, 2012.

Gabard, T. and Boudon, V.: Line broadening coefficient calculations for methane perturbed by nitrogen, *J. Quant. Spectrosc. Radiat. Transfer*, 111, 1328–1343, 2010.

- Holton, J. R.: An Introduction to Dynamic Meteorology, fourth edition, International Geophysics Series, Elsevier Academic Press, 88, 2004.
- Hase, F., Hannigan, J., Coffey, M., Goldman, A., Höpfner, M., Jones, N., Rinsland, C. and Wood, S.: Intercomparison of retrieval codes used for the analysis of high-resolution, ground-based FTIR measurements, *J. Quant. Spectrosc. Radiat. Transfer*, 87, 25–52, 2004.
- Herman, R. L., Scott, D. C., Webster, C. R., May, R. D., Moyer, E. J., Salawitch, R. J., Yung, Y. L., Toon, G. C., Sen, B., Margitan, J. J., Rosenlof, K. H., Michelson, H. A., and Elkins, J. W.: Tropical entrainment timescales inferred from stratospheric N₂O and CH₄ observations, *Geophys. Res. Letts.*, 25, 2781–2784, 1998.
- Heimann, M., and S. Körner, The Global Atmospheric Tracer Model TM3: Model description and users manual release 3.8a, Tech. Rep. 5, Max Planck Inst. for Biogeochem., Jena, Germany, 2003.
- Hourdin, F., Musat, I., Bony, S., Braconnot, P., Codron, F., Dufresne, J.-L., Fairhead, L., Filiberti, M.-A., Friedlingstein, P., Grandpeix, J.-Y., Krinner, G., Levan, P., Li, Z.-X. and Lott, F.: The LMDZ4 general circulation model: climate performance and sensitivity to parametrized physics with emphasis on tropical convection, *Climate Dynamics*, 27, 787–813, 2006.
- Haynes, P. and Shuckburgh, E.: Effective diffusivity as a diagnostic of atmospheric transport: 1. Stratosphere, *Journal of Geophysical Research: Atmospheres J. Geophys. Res.*, 105(D18), 22777–22794, 2000.
- Hess, P. G.: Mixing Processes Following the Final Stratospheric Warming, *J. Atmos. Sci.*, 48(14), 1625–1641, 1991.
- Hartmann, J.-M., Boulet, C. and Robert, D.: Collisional Effects on Molecular Spectra, Elsevier B.V., ISBN: 978-0-444-52017-3, 2008.
- Hartmann, J.-M., Tran, H., Ngo, N. H., Landsheere, X., Chelin, P., Lu, Y., Liu, A.-W., Hu, S.-M., Gianfrani, L., Casa, G., Castrillo, A., Lepère, M., Delière, Q., Dhyne, M. and Fissiaux, L.: *Ab initio* calculations of the spectral shapes of CO₂ isolated lines including non-Voigt effects and comparisons with experiments, *Phys. Rev. A*, 87, 013403, 2013.
- Hase, F., Wallace, L., Mcleod, S. D., Harrison, J. J. and Bernath, P. F.: The ACE-FTS atlas of the infrared solar spectrum, *J. Quant. Spectrosc. Radiat. Transfer*, 111, 521–528, 2010.
- Hase, F., Demoulin, P., Sauval, A., Toon, G., Bernath, P., Goldman, A., Hannigan, J. and Rinsland, C.: An empirical line-by-line model for the infrared solar transmittance spectrum from 700 to 5000 cm⁻¹, *J. Quant. Spectrosc. Radiat. Transfer*, 102, 450–463, 2006.
- Hase, F., Blumenstock, T. and Paton-Walsh, C.: Analysis of the Instrumental Line Shape of High-Resolution Fourier Transform IR Spectrometers with Gas Cell Measurements and New Retrieval Software, *Appl. Opt.*, 38, 3417–3422, 1999.
- Jacob, D. J.: Introduction to Atmospheric Chemistry, Princeton University Press, Princeton, NJ,

ISBN 0-691-00185-5, 1999.

Jenouvrier, A., Daumont, L., Régalia-Jarlot, L., Tyuterev, V. G., Carleer, M., Vandaele, A. C., Mikhailenko, S. and Fally, S.: Fourier transform measurements of water vapor line parameters in the 4200–6600 cm⁻¹ region, *J. Quant. Spectrosc. Radiat. Transfer*, 105, 326–355, 2007.

Kirschke, Stefanie, Philippe Bousquet, Philippe Ciais, Marielle Saunois, Josep G. Canadell, Edward J. Dlugokencky, Peter Bergamaschi, Daniel Bergmann, Donald R. Blake, Lori Bruhwiler, Philip Cameron-Smith, Simona Castaldi, Frédéric Chevallier, Liang Feng, Annemarie Fraser, Martin Heimann, Elke L. Hodson, Sander Houweling, Béatrice Josse, Paul J. Fraser, Paul B. Krummel, Jean-François Lamarque, Ray L. Langenfelds, Corinne Le Quéré, Vaishali Naik, Simon O'doherty, Paul I. Palmer, Isabelle Pison, David Plummer, Benjamin Poulter, Ronald G. Prinn, Matt Rigby, Bruno Ringeval, Monia Santini, Martina Schmidt, Drew T. Shindell, Isobel J. Simpson, Renato Spahni, L. Paul Steele, Sarah A. Strode, Kengo Sudo, Sophie Szopa, Guido R. Van Der Werf, Apostolos Voulgarakis, Michiel Van Weele, Ray F. Weiss, Jason E. Williams, and Guang Zeng.: Three decades of global methane sources and sinks, *Nature Geoscience*, 16, 2013.

Kort, E. A., P. K. Patra, K. Ishijima, B. C. Daube, R. Jiménez, J. Elkins, D. Hurst, F. L. Moore, C. Sweeney, and S. C. Wofsy: Tropospheric distribution and variability of N₂O: Evidence for strong tropical emissions, *Geophys. Res. Lett.*, 38, L15806, doi:10.1029/2011GL047612, 2011.

Krol, M., Houweling, S., Bregman, B., Broek, M. V. D., Segers, A., Velthoven, P. V., Peters, W., Dentener, F. and Bergamaschi, P.: The two-way nested global chemistry-transport zoom model TM5: algorithm and applications, *Atmospheric Chemistry and Physics Discussions Atmos. Chem. Phys. Discuss.*, 5, 3975–4018, 2005.

Kalnay, K., Kanamitsu, M., Kistler, R., Collins, W., Deaven, D., Candin, L., Iredell, M., Saha, S., White, G., Woollen, J., Zhu, Y., Leetmaa, A., Reynolds, R., Chelliah, M., Ebisuzaki, W., Higgins, W., Janowiak, J., Mo, K. C., Ropelewski, C., Wang, J., Jenne, R., and Joseph, D.: The NCEP/NCAR 40-year reanalysis project, *B. Am. Meteorol. Soc.*, 77, 437–470, 1996.

Kennaugh, R., Ruth, S. and Gray, L. J.: Modeling quasi-biennial variability in the semiannual double peak, *J. Geophys. Res.*, 102(D13), 16169–16187, 1997.

Keeling, C. D.: The concentration and isotopic abundances of carbon dioxide in rural and marine air, *Geochimica et Cosmochimica Acta*, 24, 277–298, 1961.

Keeling, C. D.: The concentration and isotopic abundances of atmospheric carbon dioxide in rural areas, *Geochimica et Cosmochimica Acta*, 13, 322–334, 1958.

Keeling, C. D., Mook, W. G. and Tans, P. P.: Recent trends in the ¹³C/¹²C ratio of atmospheric carbon dioxide, *Nature*, 277, 121–123, 1979.

Keeling, C. D., Carter, A. F. and Mook, W. G.: Seasonal, latitudinal, and secular variations in the abundance and isotopic ratios of atmospheric CO₂: 2. Results from oceanographic cruises in the tropical Pacific Ocean, *J. Geophys. Res.*, 89, 4615–4615, 1984.

Kelley, C. T.: Iterative Methods for Optimization, Society for Industrial and Applied Mathematics, 1999.

Lamouroux, J., Tran, H., Laraia, A., Gamache, R., Rothman, L., Gordon, I. and Hartmann, J.-M.: Updated database plus software for line-mixing in CO₂ infrared spectra and their test using laboratory spectra in the 1.5–2.3 μm region, *J. Quant. Spectrosc. Radiat. Transfer*, 111, 2321–2331, 2010.

Mitchell, J. F. B.: The "Greenhouse" Effect And Climate Change, *Reviews of Geophysics*, 27, 115–139, 1989.

Melton, J. R., R. Wania, E. L. Hodson, B. Poulter, B. Ringeval, R. Spahni, T. Bohn, C. A. Avis, D. J. Beerling, G. Chen, A. V. Eliseev, S. N. Denisov, P. O. Hopcroft, D. P. Lettenmaier, W. J. Riley, J. S. Singarayer, Z. M. Subin, H. Tian, S. Zürcher, V. Brovkin, P. M. Van Bodegom, T. Kleinen, Z. C. Yu, and J. O. Kaplan.: Present state of global wetland extent and wetland methane modelling: conclusions from a model inter-comparison project (WETCHIMP), *Biogeosciences*, 753-788, 2013.

Michelson, H. A., Manney, G. L., Gunson, M. R., Rinsland, C. P., and Zander, R.: Correlations of stratospheric abundances of CH₄ and N₂O derived from ATMOS measurements, *Geophys. Res. Letts.*, 25, 2777-2780, 1998.

Messerschmidt, J.; Macatangay, R.; Notholt, J.; Petri, C.; Warneke, T. and Weinzierl, C.: Side by side measurements of CO₂ by ground-based Fourier transform spectrometry (FTS), *Tellus*, 62B, 749-758, 2010.

Messerschmidt, J., Chen, H., Deutscher, N. M., Gerbig, C., Grupe, P., Katrynski, K., Koch, F.-T., Lavric, J. V., Notholt, J., Rödenbeck, C., Ruhe, W., Warneke, T., and Weinzierl, C.: Automated ground-based remote sensing measurements of greenhouse gases at the Bialystok site in comparison with collocated in situ measurements and model data, *Atmos. Chem. Phys.*, 12, 6741-6755, doi:10.5194/acp-12-6741-2012, 2012.

Meirink, J. F., Bergamaschi, P., and Krol, M. C.: Four-dimensional variational data assimilation for inverse modelling of atmospheric methane emissions: method and comparison with synthesis inversion, *Atmos. Chem. Phys.*, 8, 6341-6353, doi:10.5194/acp-8-6341-2008, 2008.

Mook, W. G., Koopmans, M., Carter, A. F. and Keeling, C. D.: Seasonal, latitudinal, and secular variations in the abundance and isotopic ratios of atmospheric carbon dioxide: 1. Results from land stations, *J. Geophys. Res. Journal of Geophysical Research*, 88, 10915–10915, 1983.

Miloshevich, L. M., Vömel, H., Whiteman, D. N. and Leblanc, T.: Accuracy assessment and correction of Vaisala RS92 radiosonde water vapor measurements, *J. Geophys. Res.*, 114, D11305, 2009.

Miller, C. E., Brown, L. R., Toth, R. A., Benner, D. C. and Devi, V. M.: Spectroscopic challenges for high accuracy retrievals of atmospheric CO₂ and the Orbiting Carbon Observatory (OCO) experiment, *Comptes Rendus Physique*, 6, 876–887, 2005.

- Miller, C. E. and Brown, L. R.: Near infrared spectroscopy of carbon dioxide II. $^{16}\text{O}^{13}\text{C}^{16}\text{O}$ and $^{16}\text{O}^{13}\text{C}^{18}\text{O}$ line positions, *Journal of Molecular Spectroscopy*, 228, 329–354, 2004.
- Naik, V., A. Voulgarakis, A. M. Fiore, L. W. Horowitz, J.-F. Lamarque, M. Lin, M. J. Prather, P. J. Young, D. Bergmann, P. J. Cameron-Smith, I. Cionni, W. J. Collins, S. B. Dalsøren, R. Doherty, V. Eyring, G. Faluvegi, G. A. Folberth, B. Josse, Y. H. Lee, I. A. Mackenzie, T. Nagashima, T. P. C. Van Noije, D. A. Plummer, M. Righi, S. T. Rumbold, R. Skeie, D. T. Shindell, D. S. Stevenson, S. Strode, K. Sudo, S. Szopa, and G. Zeng.: Preindustrial to present-day changes in tropospheric hydroxyl radical and methane lifetime from the Atmospheric Chemistry and Climate Model Intercomparison Project (ACCMIP), *Atmos. Chem. Phys.*, 13, 5277–5298, 2013.
- Nakamura, N.: Two-Dimensional Mixing, Edge Formation, and Permeability Diagnosed in an Area Coordinate, *J. Atmos. Sci. Journal of the Atmospheric Sciences*, 53(11), 1524–1537, 1996.
- Nakamura, N. and Ma, J.: Modified Lagrangian-mean diagnostics of the stratospheric polar vortices: 2. Nitrous oxide and seasonal barrier migration in the cryogenic limb array etalon spectrometer and SKYHI general circulation model, *Journal of Geophysical Research: Atmospheres J. Geophys. Res.*, 102(D22), 25721–25735, 1997.
- Ostler, A., Sussmann, R., Patra, P. K., Houweling, S., De Bruine, M., Stiller, G. P., Hänel, F. J., Plieninger, J., Bousquet, P., Yin, Y., Saunois, M., Walker, K. A., Deutscher, N. M., Griffith, D. W. T., Blumenstock, T., Hase, F., Warneke, T., Wang, Z., Kivi, R., and Robinson, J.: Model – TCCON comparisons of column-averaged methane with a focus on the stratosphere, *Atmos. Meas. Tech. Discuss.*, doi:10.5194/amt-2016-90, in review, 2016.
- Patra, P. K., Houweling, S., Krol, M., Bousquet, P., Belikov, D., Bergmann, D., Bian, H., Cameron-Smith, P., Chipperfield, M. P., Corbin, K., Fortems-Cheiney, A., Fraser, A., Gloor, E., Hess, P., Ito, A., Kawa, S. R., Law, R. M., Loh, Z., Maksyutov, S., Meng, L., Palmer, P. I., Prinn, R. G., Rigby, M., Saito, R., and Wilson, C.: TransCom model simulations of CH_4 and related species: linking transport, surface flux and chemical loss with CH_4 variability in the troposphere and lower stratosphere, *Atmos. Chem. Phys.*, 11, 12813–12837, doi:10.5194/acp-11-12813-2011, 2011.
- Pison, I., Ringeval, B., Bousquet, P., Prigent, C., and Papa, F.: Stable atmospheric methane in the 2000s: key-role of emissions from natural wetlands, *Atmos. Chem. Phys.*, 13, 11609–11623, doi:10.5194/acp-13-11609-2013, 2013.
- Plumb, R. A., and Ko, M. K. W.: Interrelationships Between Mixing Ratios of Long Lived Stratospheric Constituents, *J. Geophys. Res-Atmos.*, 97, 10145–10156, 1992.
- Palm, M., Melsheimer, C., Noël, S., Heise, S., Notholt, J., Burrows, J., and Schrems, O.: Integrated water vapor above Ny Ålesund, Spitsbergen: a multi-sensor intercomparison, *Atmos. Chem. Phys.*, 10, 1215–1226, doi:10.5194/acp-10-1215-2010, 2010.
- Parker, R., Boesch, H., Cogan, A., Fraser, A., Feng, L., Palmer, P. I., Messerschmidt, J., Deutscher, N., Griffith, D. W. T., Notholt, J., Wennberg, P. O. and Wunch, D.: Methane observations from the

Greenhouse Gases Observing SATellite: Comparison to ground-based TCCON data and model calculations, *Geophys. Res. Lett.*, 38, L15807, 2011.

Predoi-Cross, A., Unni, A., Liu, W., Schofield, I., Holladay, C., Mckellar, A. and Hurtmans, D.: Line profile study of transitions in the $30012 \leftarrow 00001$ and $30013 \leftarrow 00001$ bands of carbon dioxide perturbed by air, *Journal of Molecular Spectroscopy*, 246, 121, 2007.

Rhee, T. S., Kettle, A. J. and Andreae, M. O.: Methane and nitrous oxide emissions from the ocean: A reassessment using basin-wide observations in the Atlantic, *J. Geophys. Res.*, 114, D12304, 2009.

Rodgers, C. D.: Inverse Methods for Atmospheric Sounding: Theory and Practice, vol. 2 of Series on Atmospheric, Oceanic and Planetary Physics, edited by: Taylor, F. W., World Scientific, 2000.

Rothman, L. S.: The evolution and impact of the HITRAN molecular spectroscopic database, *J. Quant. Spectrosc. Radiat. Transfer*, 111, 1565–1567, 2010.

Rigby, M., Prinn, R. G., Fraser, P. J., Simmonds, P. G., Langenfelds, R. L., Huang, J., Cunnold, D. M., Steele, L. P., Krummel, P. B., Weiss, R. F., O'Doherty, S., Salameh, P. K., Wang, H. J., Harth, C. M., Muehle, J., and Porter, L. W.: Renewed growth of atmospheric methane, *Geophys. Res. Lett.*, 35, L22805, doi:10.1029/2008GL036037, 2008.

Rödenbeck, C., Estimating CO₂ sources and sinks from atmospheric mixing ratio measurements using a global inversion of atmospheric transport, Technical Report 6, Max Planck Institute for Biogeochemistry, Jena, Germany, 2005.

Rojas, M. and Norton, W.: Amplification of the 2-day wave from mutual interaction of global Rossby-gravity and local modes in the summer mesosphere, *J. Geophys. Res.*, 112(D12), 2007.

Randel, W. J., Wu, F., Russell, J. M., Roche, A. and Waters, J. W.: Seasonal Cycles and QBO Variations in Stratospheric CH₄ and H₂O Observed in UARS HALOE Data, *J. Atmos. Sci.*, 55(2), 163–185, 1998.

Rothman, L.s., I.e. Gordon, A. Barbe, D.chris Benner, P.f. Bernath, M. Birk, V. Boudon, L.r. Brown, A. Campargue, J.-P. Champion, K. Chance, L.h. Coudert, V. Dana, V.m. Devi, S. Fally, J.-M. Flaud, R.r. Gamache, A. Goldman, D. Jacquemart, I. Kleiner, N. Lacome, W.j. Lafferty, J.-Y. Mandin, S.t. Massie, S.n. Mikhailyko, C.e. Miller, N. Moazzen-Ahmadi, O.v. Naumenko, A.v. Nikitin, J. Orphal, V.i. Perevalov, A. Perrin, A. Predoi-Cross, C.p. Rinsland, M. Rotger, M. Šimečková, M.a.h. Smith, K. Sung, S.a. Tashkun, J. Tennyson, R.a. Toth, A.c. Vandaele, and J. Vander Auwera.: The HITRAN 2008 molecular spectroscopic database, *J. Quant. Spectrosc. Radiat. Transfer*, 110, 533–572, 2009.

Rohart François, Mäder Heinrich and Nicolaisen, H.-W.: Speed dependence of rotational relaxation induced by foreign gas collisions: Studies on CH₃F by millimeter wave coherent transients, *J. Chem. Phys.*, 101, 6475, 1994.

Spahni, R., Wania, R., Neef, L., Weele, M. V., Pison, I., Bousquet, P., Frankenberg, C., Foster, P. N., Joos, F., Prentice, I. C. and Velthoven, P. V.: Constraining global methane emissions and uptake by

ecosystems, *Biogeosciences*, 8, 1643–1665, 2011.

Sepúlveda, E., Schneider, M., Hase, F., García, O. E., Gomez-Pelaez, A., Dohe, S., Blumenstock, T., and Guerra, J. C.: Long-term validation of tropospheric column-averaged CH₄ mole fractions obtained by mid-infrared ground-based FTIR spectrometry, *Atmos. Meas. Tech.*, 5, 1425-1441, doi:10.5194/amt-5-1425-2012, 2012.

Sugimoto, A., Inoue, T., Kirtibutr, N. and Abe, T.: Methane oxidation by termite mounds estimated by the carbon isotopic composition of methane, *Global Biogeochemical Cycles*, 12, 595–605, 1998.

Sepúlveda, E., Schneider, M., Hase, F., Barthlott, S., Dubravica, D., García, O. E., Gomez-Pelaez, A., González, Y., Guerra, J. C., Gisi, M., Kohlhepp, R., Dohe, S., Blumenstock, T., Strong, K., Weaver, D., Palm, M., Sadeghi, A., Deutscher, N. M., Warneke, T., Notholt, J., Jones, N., Griffith, D. W. T., Smale, D., Brailsford, G. W., Robinson, J., Meinhardt, F., Steinbacher, M., Aalto, T., and Worthy, D.: Tropospheric CH₄ signals as observed by NDACC FTIR at globally distributed sites and comparison to GAW surface in situ measurements, *Atmos. Meas. Tech.*, 7, 2337-2360, doi:10.5194/amt-7-2337-2014, 2014.

Schmidt, M., Lopez, M., Yver Kwok, C., Messager, C., Ramonet, M., Wastine, B., Vuillemin, C., Truong, F., Gal, B., Parmentier, E., Cloué, O., and Ciais, P.: High-precision quasi-continuous atmospheric greenhouse gas measurements at Trainou tower (Orléans forest, France), *Atmos. Meas. Tech.*, 7, 2283-2296, doi:10.5194/amt-7-2283-2014, 2014.

Spivakovsky, C. M., Logan, J. A., Montzka, S. A., Balkanski, Y. J., Foreman-Fowler, M., Jones, D. B. A., Horowitz, L. W., Fusco, A. C., Brenninkmeijer, C. A. M., Prather, M. J., Wofsy, S. C., McElroy, M. B., Three-dimensional climatological distribution of tropospheric OH: update and evaluation, *J. Geophys. Res.*, 105, 8931–8980, 2000.

Sussmann, R. and Borsdorff, T.: Interference errors in infrared remote sounding of the atmosphere, *Atmos. Chem. Phys.*, 7, 13027–13073, 2007.

Schneider, M. and Hase, F.: Improving spectroscopic line parameters by means of atmospheric spectra: Theory and example for water vapor and solar absorption spectra, *J. Quant. Spectrosc. Radiat. Transfer*, 1825–1839, 2009.

Toon, G. C., Farmer, C. B., Schaper, P. W., Lowes, L. L., Norton, R. H., Schoeberl, M. R., Lait, L. R. and Newman, P. A.: Evidence for subsidence in the 1989 Arctic winter stratosphere from airborne infrared composition measurements, *J. Geophys. Res.*, 97, 7963–7963, 1992.

Trusilova, K., Rödenbeck, C., Gerbig, C., and Heimann, M.: Technical Note: A new coupled system for global-to-regional downscaling of CO₂ concentration estimation, *Atmos. Chem. Phys.*, 10, 3205-3213, doi:10.5194/acp-10-3205-2010, 2010.

Trepte, C. R. and Hitchman, M. H.: Tropical stratospheric circulation deduced from satellite aerosol data, *Nature*, 355(6361), 626–628, 1992.

Tran, H., Flaud, P.-M., Gabard, T., Hase, F., Clarmann, T. V., Camy-Peyret, C., Payan, S. and Hartmann, J.-M.: Model, software and database for line-mixing effects in the v3 and v4 bands of CH₄ and tests using laboratory and planetary measurements-I: N₂ (and air) broadenings and the earth atmosphere, *J. Quant. Spectrosc. Radiat. Transfer*, 101, 284–305, 2006.

Toth, R. A.: Measurements of positions, strengths and self-broadened widths of H₂O from 2900 to 8000 cm⁻¹: line strength analysis of the 2nd triad bands, *J. Quant. Spectrosc. Radiat. Transfer*, 94, 51–107, 2005.

Toth, R., Brown, L., Miller, C., Devi, V. M. and Benner, D.: Spectroscopic database of CO₂ line parameters: 4300–7000 cm⁻¹, *J. Quant. Spectrosc. Radiat. Transfer*, 109, 906–921, 2008a.

Toth, R., Miller, C., Brown, L., Devi, V. M. and Benner, D. C.: Line strengths of ¹⁶O¹³C¹⁶O, ¹⁶O¹³C¹⁸O, ¹⁶O¹³C¹⁷O and ¹⁸O¹³C¹⁸O between 2200 and 6800 cm⁻¹, *Journal of Molecular Spectroscopy*, 251, 64–89, 2008b.

Werf, G. R. V. D., Randerson, J. T., Giglio, L., Collatz, G. J., Mu, M., Kasibhatla, P. S., Morton, D. C., Defries, R. S., Jin, Y. and Leeuwen, T. T. V.: Global fire emissions and the contribution of deforestation, savanna, forest, agricultural, and peat fires (1997–2009), *Atmos. Chem. Phys.*, 10, 11707–11735, 2010.

Wunch, D., Toon, G. C., Blavier, J.-F. L., Washenfelder, R. A., Notholt, J., Connor, B. J., Griffith, D. W. T., Sherlock, V. and Wennberg, P. O.: The Total Carbon Column Observing Network, *Philosophical Transactions of the Royal Society A*, 2087–2112, 2011.

Warneke, T., Meirink, J. F., Bergamaschi, P., Groß, J.-U., Notholt, J., Toon, G.C., Velazco, V., Goede, A.P.H., and Schrems O.: Seasonal and latitudinal variation of atmospheric methane: A ground-based and ship-borne solar IR spectroscopic study, *Geophys. Res. Lett.*, 33, L14812, doi:10.1029/2006GL025874, 2006.

Washenfelder, R. A., Wennberg, P. O., and Toon, G. C.: Tropospheric methane retrieved from ground-based near-IR solar absorption spectra, *Geophys. Res. Lett.*, 30, L017969, doi:10.1029/2003GL017969, 2003.

Wunch, D., Toon, G. C., Wennberg, P. O., Wofsy, S. C., Stephens, B. B., Fischer, M. L., Uchino, O., Abshire, J. B., Bernath, P., Biraud, S. C., Blavier, J.-F. L., Boone, C., Bowman, K. P., Browell, E. V., Campos, T., Connor, B. J., Daube, B. C., Deutscher, N. M., Diao, M., Elkins, J. W., Gerbig, C., Gottlieb, E., Griffith, D. W. T., Hurst, D. F., Jiménez, R., Keppel-Aleks, G., Kort, E. A., Macatangay, R., Machida, T., Matsueda, H., Moore, F., Morino, I., Park, S., Robinson, J., Roehl, C. M., Sawa, Y., Sherlock, V., Sweeney, C., Tanaka, T., and Zondlo, M. A.: Calibration of the Total Carbon Column Observing Network using aircraft profile data, *Atmos. Meas. Tech.*, 3, 1351–1362, doi:10.5194/amt-3-1351-2010, 2010.

Wofsy, S. C., et al.: HIAPER Pole-to-Pole Observations (HIPPO): fine-grained, global-scale measurements of climatically important atmospheric gases and aerosols, *Proc. Roy. Soc. A*, 369,

2073-2086, doi: 10.1098/rsta.2010.0313, 2011.

Wilcox, L. J., Hoskins, B. J. and Shine, K. P.: A global blended tropopause based on ERA data. Part I: Climatology, Q.J.R. Meteorol. Soc., 138, 561–575, 2012.

Acknowledgments

I would like to thank Prof. Justus Notholt for providing me an opportunity of doing the PhD thesis in his group. During the research work I got many advices and encourages from him, and Thorsten Warneke, Nicholas Deutscher and Mathias Palm. They helped me go into the remote sensing field in a short time, pointed out directions worth pursuing and prepared me necessary knowledge and tools. Without these guides the thesis can not be finished. It is a pleasure time during the stay in Bremen because of both good work environment in the group and moderate weather conditions.

Also, I have to thank Stefan Kowaleski and Christof Petri for introducing me how to operate FTIR instrument. I still remember how difficult the FTIR looks to me when I touched it for the first time. I am grateful to Matthias Buschmann for introducing Python to me, which is a very important tool for all the data analysis in the thesis.

Because of my broken English it is difficult to commute with me, however all the members of the group always show great patience in listening to me. Especially during the first a few months they try best to integrate me into the group. I am grateful to their efforts for reducing my uncomfortable feeling because that is the first time when I was facing people with completely different customs and speaking different languages.

During my short stay in Frank Hase's group he provided Proffit to me and carefully explained how to use it. That is especially important in the work about retrieval of CO₂ isotopes.

In the master period Prof. Lei Zhang (Lanzhou University, China) introduced me into Atmospheric Physics and showed how to do research work there.

Finally, I want to thank my grandparents, parents and other members for tolerating my not visiting them in a so long time.

The CSC (China Scholarship Council) provide funds for cover my living expenses in Bremen during first four years.